4799FR

Debris Characterisation and Modelling (DeCaM) Software Improvements

Final Report

(Contract No. W7701-7-3386/001/XSK)

August 1999

Prepared by:

Fleet Technology Limited
311 Legget Drive
Kanata, Ontario
K2K 1Z8

Scientific Authority
Yves Baillargeon

For:

Department of National Defence
Defence Research Establishment Valcartier
2459 Pie-XI Blvd. North
Val-Bélair, QC
G3J 1X5

FTL Contact: A. Dinovitzer, P.Eng.
Tel: (613) 592-2830 ext 203
Fax: (613) 592-4950
E-mail: Adinovit@fleetech.com

FTL DOCUMENT QUALITY CONTROL DATA SHEET

Report: Debris Characterisation and Modelling (DeCaM) Software Improvements Final Report

Project No. 4799

Date: August 1999

Prepared by: A. Dinovitzer, Principal Engineer

Checked by: B. Xu, Project Engineer

Approved for Release by: I. Glen, President - Fleet Technology Limited

ACKNOWLEDGMENTS

This work was funded by the Department of National Defence (DND) through the Defence Research Establishment Valcartier (DREV). The authors wish to thank Mr. Michel Szymczak of the Defence Research Establishment Valcartier who acted as the Scientific Authority for the project. His comments and reviews of the development work and final product have been most useful and encouraging.

Project Team

The development of the theory and software included in the DeCaM Software are the result of the efforts of the following Fleet Technology Limited personnel:

Aaron Dinovitzer	Principal Investigator
Terry Brown	Programmer / Project Engineer
Bo Xu	Project Engineer
Mike Bennett	Project Engineer
Robert Walker	Project Engineer

Disclaimer

The contents of this report and the processes and data that are embedded in the program reflect the views of the above named contractors and do not necessarily reflect the official view or opinions of the Department of National Defence.

EXECUTIVE SUMMARY

The lethality of ammunition, and/or the effectiveness of armour can be assessed by the penetration (or perforation) performance of the ammunition, and by the nature of the "debris" that results on the "inside" of the armour following a threat/armour interaction. The "debris" comprises the residual projectile and armour fragments generated during the penetration event. These fragments are referred to as behind-armour debris or BA debris.

The effectiveness of the projectile or the armour may be assessed with knowledge of the characteristics (mass, velocity and trajectory) of this debris cloud. Experimental techniques have been developed to measure the BA debris using "witness packs" (thin plates in which the number and nature of the resulting holes can be measured) and flash radiography (time lapse debris fragment position images). These results may be used in larger vulnerability/lethality (V/L) models, in which the effect of a range of projectiles or other threats on the total system (e.g. land, air or sea vehicles) are used to assist in design, in terms of layout and protection.

The following report outlines the work carried out in a project aimed at improving and extending the Debris Characterisation and Modelling (DeCaM) software developed under a previous contract. The overall objective of this project was to improve and extend the characterisation and modelling capabilities of the DeCaM software. This overall objective can be divided into the following specific objectives:

a) Facilitate the application of the DeCaM software by incorporating projectile, witness pack, armour system and materials databases,

b) Incorporate the Multiple Plate Penetration Model (MPPM3) software in DeCaM to model the penetration and residual characteristics of projectiles,

c) Improve the witness pack BA debris characterisation process,

d) Improve the target penetration process simulation graphics to better present the results of the DeCaM characterisation and modelling processes, and

e) Review the potential for the inclusion of ballistic impact back splash and non-penetrating spall events.

This report presents the results of the work completed in this project in five broad sections:

- Literature and Analytical Technique Reviews- provides information concerning recent BA debris modelling work by others, backsplash, spall and the MPPM3 software. These reviews indicated that that backsplash was not a concern for conventional (velocity < 1500m/s) ammunition and that the existing spall modelling techniques required further development before they could be implemented in the DeCaM software.
- BA Debris Characterisation Improvements - includes descriptions of modifications to the witness pack hole matching process and the development and implementation of witness pack plate penetration threshold curves. The threshold curves provide a link between a fragment's size, its depth of penetration within a witness pack and its velocity prior to entering the witness pack.

- BA Debris Modelling Improvements - describes the efforts focussed on improving the target fragmentation model which predicts the number of fragments produced in a ballistic penetration event.
- DeCaM Software Improvements - presents improvements to the graphical display of DeCaM simulated ballistic penetration events and the development and population of DeCaM software related databases.
- Concluding Remarks and Recommendations.- outlines the status of the DeCaM software and discusses the way ahead.

While this report provides some background information on the modified or improved portions of the DeCaM software, it does not repeat all of the information given in the project report delivered to DREV describing the initial development of the DeCaM software.

ABSTRACT

While both the potential lethality and the random nature of behind armour-debris have been recognised, practical means of their quantitative prediction have not been developed. In an effort to bridge this gap DREV initiated a project to develop a basis for vulnerability and lethality modelling which resulted in the development of the Debris Characterisation and Modelling (DeCaM) software. The following report outlines the work completed to improve and extend the behind-armour (BA) debris characterisation and modelling capabilities of DeCaM. This report does not try to repeat all of the theory developed for the DeCaM software but focuses on the studies completed in this development effort and the modifications which were implemented to produce DeCaM 2.0. A detailed description of the software and its operation is presented in the DeCaM on-line help system.

This report presented the literature and analytical technique reviews completed in support of this development work, details of the BA debris characterisation and modelling improvements, descriptions of the DeCaM software improvements and concludes with some future development recommendations for the way ahead.

The literature review, in addition to providing background information for the implemented modifications, indicated that backsplash was not a concern for conventional (velocity < 1500m/s) ammunition and that the existing spall modelling techniques required further development before they could be implemented in the DeCaM software. The characterisation development work resulted in the implementation of witness pack penetration threshold curves and indicated the need for additional work on the penetration hole growth algorithms. While the DeCaM 2.0 target fragmentation model, used to predict the number of fragments developed in a ballistic penetration event, compares well with experimental data, is recommended that the predictive capabilities of the modelling process be improved though the extension of energy and momentum conservation concepts. In general, the presentation and ballistic penetration simulation animation graphics enhancement implemented in DeCaM 2.0 significantly improve the usability and value of the software.

The general conclusion developed in this project is that while the DeCaM software is a good BA debris characterisation and modelling tool, it can be improved and extended to increase its value in vulnerability and lethality evaluation.

Table of Contents

Page

ACKNOWLEDGMENTS II

EXECUTIVE SUMMARY III

ABSTRACT V

1.0 INTRODUCTION 1
- 1.1 Background 1
- 1.2 Project Objective 1
- 1.3 Project and Report Scope 2

2.0 REVIEWS 3
- 2.1 Reviews - Introduction 3
- 2.2 Target Frontal Splash 3
  - 2.2.1 Initial Damage States of Hypervelocity Impact for Tungsten Projectile on Aluminum Targets 3
  - 2.2.2 An Aluminum Splash Generated by Impact of a Detonation Wave 4
  - 2.2.3 A Phenomenological Investigation of the Impact of Compact Projectiles against Plates at Speeds up to 3 km/s 5
  - 2.2.4 An Engineering Model to Predict Perforation Damage to Plates Impacted by High Velocity Debris Clouds 8
  - 2.2.5 The Mechanics of Penetration of Projectiles into Targets 8
  - 2.2.6 Conclusions For Frontal Splash Review 9
- 2.3 Target Spallation Behaviour 9
  - 2.3.1 Ductile Material Models 10
    - 2.3.1.1 Ductile Hole Growth under Uniaxial Stress Conditions 10
    - 2.3.1.2 The Growth of Microvoids Under the Action of HydroStatic Stress 11
    - 2.3.1.3 Numerical Modelling of Ductile Spall Fracture 12
    - 2.3.1.4 A Void Growth Relation for Ductile Porous Materials under Intense Dynamic Loading 12
    - 2.3.1.5 A Void Growth-Based Failure Model Based on A Pressure-Dependent Yield Criterion 13
  - 2.3.2 Brittle and Brittle-Ductile Material Models 14
    - 2.3.2.1 Evolution of Microcracks in Brittle Solids under Intense Dynamic Loading 14
    - 2.3.2.2 A Simple Non-Local Spallation Failure Model 14
    - 2.3.2.3 Crack Straining-Based Spall Model 15
    - 2.3.2.4 Energy-Based Spall Theory 15
    - 2.3.2.5 Computational Models for Ductile and Brittle Fracture 16
  - 2.3.3 Spall Fracture Models Summary and Comparison 17
  - 2.3.4 Concluding Remarks 22
- 2.4 Characterisation of Impact and Penetration 22
  - 2.4.1 Experimental and Numerical Simulation of High Velocity Impact on Steel Targets 22
  - 2.4.2 An Analytical Model of Hole Size in Finite Plates for Both Normal and Oblique Hypervelocity Impact for all Target Thicknesses up to the Ballistic Limit 23
  - 2.4.3 Dimensionally Scaled Penetration Experiments to Extract Projectile Sizes from Space Exposed Surfaces 24
  - 2.4.4 Characteristics of Debris Clouds Produced by Hypervelocity Impact of Aluminum Spheres with Thin Aluminum Plates 25
  - 2.4.5 Experiments on the Hypervelocity Penetration of Thin Aluminum Sheets 26

2.4.6 An Engineering Model to Predict Perforation Damage to Plates Impacted by High Velocity Debris Clouds 26
2.4.7 Ballistic Perforation Dynamics 32
2.4.8 Response of Simulated Propellant and Explosives to Projectile Impact – III Experimental and Numerical Results of Warhead Penetration and Fragmentation ... 35
2.4.9 The Influence of Plate Hardness on the Ballistic Penetration of Thick Steel Plates 38
2.4.10 Numerical and Experimental Studies of High-Velocity Impact Fragmentation 43
2.5 Multiple Plate Penetration Model 3 – MPPM3 46
2.5.1 MPPM3 Review-Introduction 46
2.5.2 Capabilities, Limitations and Definitions 46
2.5.2 1 Projectile Material and Geometry 46
2.5.2.2 Target Configuration 47
2.5.2.3 Ballistic Penetration Model 49
2.5.3 MPPM3 Modelling Data and Parameters 50
2.5.3.1 MPPM3 User Defined Data 50
2 5.3.2 MPPM3 Embedded Parameters 53
2.5.3.3 MPPM3 Input File Formats 56
2.5.4 MPPM3 Output 57
2.5.5 Software Description - Structure and Operation 58
2.5 5.1 MPPM3 I/O Module 58
2 5.5.2 MPPM3 Computational Engine Architecture 59
2.5.5.3 MPPM3 Computational Engine Pseudo Code Description 59

3.0 CHARACTERISATION PROCESS 66
3.1 Characterisation Process Introduction 66
3.1.1 Characterisation Process Overview 66
3.1.2 Scope of Characterisation Process Improvement 66
3.2 Hole Matching Process 67
3.2.1 Hole Matching Process Introduction 67
3.2.1 Hole Matching Process Improvements 69
3.3 WP Penetration Threshold Curves 70
3.3.1 WP Penetration Threshold Curve Introduction 70
3.3.2 Threshold Curve Experimental Data 70
3.3.3 Penetration Velocity Threshold Curve Regression 71
Mass [g]73
3.3.4 Witness Pack Penetration Velocity Threshold Curves 74
3.4 Characterisation and Comparison of WP BA Debris Data 76
3.4.1 Characterisation and Comparison of WP BA Debris Data Introduction 76
3.4.2 BA Debris Witness Pack Experimental Data 76
3.4.3 Comparison of Characterisation Results 77
3.4.3.1 Comparison of DeCaM Characterisation Results 77
3.4 3.2 Comparison of Estimated and Observed Velocities 80
3.4.3.3 Comparison of Estimated and Observed Masses 82
3.5 Characterisation Process Status 83

4.0 MODELLING PROCESS 84
4.1 Modelling Process Introduction 84
4.1.1 Modelling Process Overview 84
4.1.2 Scope of Modelling Process Improvements 85
4.2 Target Penetration Model Improvements 85

4.2.1 Target Penetration and Fragmentation Process Introduction.....85
4.2.2 Target Penetration Experimental Data.....85
4.2.3 Review of Target Penetration Holes.....86
4.2.3 Development of Target Penetration Cone Relations.....89
4.2.4 Estimation of Target Deformation Energy.....90
4.2.5 Fragmentation Model Target Penetration Improvements.....93
4.3 Fragmentation Model Calibration and Validation.....95
4.3.1 Fragmentation Model Calibration and Validation Introduction.....95
4.3.2 Fragmentation Model Uncertainty.....96
4.3.2 Calibration and Validation BA Debris Witness Pack Data.....97
4.3.2.1 Experimental Calibration Data.....97
4 3.2 2 Experimental Validation Data.....99
4.3.3 Fragmentation Model Calibration.....100
4.3.3.1 Results of DeCaM 2.0 Fragmentation Model Results.....100
4.3.4 Fragmentation Model Validation.....102
4.4 Modelling Process Status.....103

5.0 DECAM SOFTWARE.....104
5.1 DeCaM Software Introduction.....104
5.1.1 DeCaM 2.0 Software Overview.....104
5.1.1.1 Hardware and Software Requirements.....104
5.1.1.2 Software Installation.....104
5.1.1.3 Software Limitations.....105
5.1.2 Scope of DeCaM 2.0 Software Improvements.....105
5.2 Witness Pack, Projectile, Target and Material Databases.....105
5.3 Probabilistic Solution Automated Result Accuracy Feature.....110
5.4 Improve DeCaM Graphics and Animation.....112

6.0 CONCLUDING REMARKS AND RECOMMENDATIONS.....114
6.1 Concluding Remarks.....114
6.2 Recommendations.....114
6.2.1 Recommended Calibration and Revisions to the Current Model.....114
6.2.2 Potential Extensions of the DeCaM Process.....115
6.2.3 Possible Enhancements for the DeCaM Program.....116

7.0 REFERENCES.....117

APPENDICES.....120
Appendix A - Comparison of DeCaM Characterisation Results.....121
Appendix B - Sample *.RPT File Formats.....131

List of Figures

Page

Figure 2.1: Back Splash Momentum as a Function of Impact Speed (Mild Steel Sphere, Mild Steel Plate, $T/d = 1$)......6
Figure 2.2: Momentum as a Function of Impact Speed (Mild Steel Sphere, Steel Armour, $T/d=1$)6
Figure 2.3: Momentum as a Function of Impact Speed (Mild Steel Sphere, Mild Steel Plate, $T/d=1$)......7
Figure 2.4: Momentum as a Function of Impact Speed (Mild Steel Sphere, 4130 Steel Bar, $T/d=1$)......7
Figure 2.5: Sectioned View of the Impact Craters Formed on (a) Low Hardness and (b) High Hardness Plates......39
Figure 2.6: Velocity-Hardness Curve for Experimental Data......40
Figure 2.7: Projectile Geometry Definitions......47
Figure 2.8: Target Component Definition Parameters......48
Figure 2.9: Projectile / Target Encounter Parameters......49
Figure 2.10: MPPM3 Input File Format......56
Figure 2.11: Subroutine Calls in MPPM3......59

Figure 3.1: DeCaM BA Debris Characterisation Process......66
Figure 3.2: Grouping Witness Pack Holes on Successive Plates......67
Figure 3.3: Comparison of Leading and Trailing Hole Locations......68
Figure 3.4: M1 Witness Pack V_{50} Penetration Threshold Velocity Curves......75
Figure 3.5: V_{50} and V_{95} Penetration Velocity Threshold Estimation Inconsistencies......80
Figure 3.6: Residual Projectile Velocity Error Ranges......82

Figure 4.1: DeCaM BA Debris Modelling Process......84
Figure 4.2: Petalling and Plug Penetration......87
Figure 4.3: Penetrated Plate Geometric Measures......88
Figure 4.4: Target Penetration Cone Geometry to Impact Velocity Relations......89
Figure 4.4: Target Deformation Trends for Type A Petalling Penetration......91
Figure 4.5: Target Deformation Trends for Type B Petalling Penetration......91
Figure 4.6: Target Deformation Trends for Type C Plugging Penetration......92
Figure 4.7: Idealised Deformation Energy to Impact Velocity Relationship......92
Figure 4.8: Target Plug Fragmentation Zone......93
Figure 4.9: Fragmentation Model Calibration Results......102
Figure 4.10: Fragmentation Model Validation Results......103

Figure 5.1: DeCaM 2.0 Characterisation Data Entry Dialog Box......106
Figure 5.2: Projectile Data Entry Dialog Box......107
Figure 5.3: Projectile Database Dialog Box......107
Figure 5.4:Witness Pack Database Dialog Box......108
Figure 5.5: Target System Database......108
Figure 5.6: DeCaM Data Menu......109
Figure 5.7: Material Database Dialog Box......109
Figure 5.8: Material Database Add/Edit Dialogue box......109
Figure 5.6: Probabilistic Modelling Parameter Dialog Box......110

Figure 5.7: DeCaM 2.0 Characterisation and Modelling 3D BA-Debris Animation 112
Figure 5.8: BA-Debris Statistical Distribution Viewer..113

List of Tables

Page

Table 1.1: Project Statement of Work Summary 2

Table 2.1: Ductile Material Models 20
Table 2.2: Brittle and Ductile Material Models 21
Table 2.3: Material Parameters for Propergol used in Penetration Computations 37
Table 2.4: Steel Cover and Projectile Material Parameters in Penetration Computations 37
Table 2.5: Impact Parameters and Results Summary 43
Table 2.6: Projectile (C) Data Summary 51
Table 2.7: Encounter (E) Data Summary 51
Table 2.8: Target (P) Data Summary 52
Table 2.9: Parameters for S2M2 18 Plate Array 53
Table 2.10: Target Component Material Codes 54
Table 2.11: Metallic Target Material Property Definitions 54
Table 2.12: Non-Metallic Target Material Property Definitions 55
Table 2.13: Target Metallic Material Property Parameter Summary* 55
Table 2.14: Target Non-Metallic Material Property Parameter Summary* 55
Table 2.15: MPPM3 Standard Output Data Summary 57
Table 2.16: TPPM Output Data Summary 58

Table 3.1: FSP Geometric Parameters 70
Table 3.2: Witness Pack Configurations 70
Table 3.3: WP-Calibration Data 72
Table 3.4: Coefficients and Powers for WP Threshold Curve Formula 73
Table 3.5: Extrapolated V_{50} Witness Pack Threshold Data 73
Table 3.6: Extrapolated V_{90} Witness Pack Threshold Data 74
Table 3.7: Extrapolated V_{95} Witness Pack Threshold Data 74
Table 3.8: Typical Witness Pack Penetration Velocity Threshold Data File 75
Table 3.9: Data Used in DeCaM BA Debris Characterisation Process 76
Table 3.10: Experimental Data and Measurements Unique to Each Test 77
Table 3.11: Test 3536 Comparison 78
Table 3.12: Comparison of V_{50} and V_{95} Characterisation Results for Test 3527 79
Table 3.13: Comparison of Estimated and Observed Fragment Velocities 81
Table 3.14: Comparison of Estimated and Observed Residual Projectile Velocities [m/s] 81
Table 3.15: Comparison of Fragment Geometry 82
Table 3.16: Comparison of MPPM3 Residual Projectile Mass 83

Table 4.1: Target Penetration Experimental Data 86
Table 4.2: Penetration Zone Geometry 88
Table 4.3: Percentage of Plastic Energy to Impact Energy 90
Table 4.4: Calibration Data Used in DeCaM BA Debris Characterisation Process 97
Table 4.5: Experimental Calibration Data and Measurements Unique to Each Test 98
Table 4.6: Validation Data Used in DeCaM BA Debris Characterisation Process 99

Table 4.7: Experimental Validation Data and Measurements Unique to Each Test 99
Table 4.8: Fragmentation Model Calibration Results 101
Table 4.9: Fragmentation Model Validation Results 102

Table A.1: Test 3527 Comparison 121
Table A.2: Test 3528 Comparison 122
Table A.3: Test 3529 Comparison 123
Table A.4: Test 3530 Comparison 124
Table A.5: Test 3531 Comparison 125
Table A.6: Test 3532 Comparison 126
Table A.7: Test 3533 Comparison 127
Table A.8: Test 3534 Comparison 128
Table A.9: Test 3535 Comparison 129
Table A.10 Test 3536 Comparison 130

1.0 INTRODUCTION

1.1 Background

The lethality of ammunition, and/or the effectiveness of armour can be assessed by the penetration (or perforation) performance of the ammunition, and by the nature of the "debris" that results on the "inside" of the armour following a threat/armour interaction. The "debris" comprises the residue of the projectile that penetrates the armour, as well as the "spall" - destroyed particles from the armour. These are referred to as behind-armour debris or BA-debris.

The effectiveness of the projectile or the armour may be assessed with knowledge of the characteristics of this debris cloud. Experimental techniques have been developed to measure the debris using "witness packs" behind the armour - thin plates in which the number and nature of the resulting holes can be measured - and by flash radiography to visualise the debris cloud and obtain position and velocity data.

The results of behind-armour debris modelling efforts are used in larger vulnerability / lethality (V/L) models in which the effect on the total system (e.g. land, air or sea vehicles) of a range of projectiles or other threats are used to assist in the design in terms of layout and protection. Such V/L models require relatively accurate modelling not only of the probability and nature of penetration, but also the resulting debris, since the latter can cause significant damage to equipment, components and personnel.

A variety of projectile and penetration models exist which can reproduce or predict experimental results. These models have been used in conjunction with empirical, kinematic and mechanics based approaches to develop BA-debris damage potential predictive schemes. BA-debris modelling is a complex problem requiring a good understanding of the underlying physics and the statistical nature of the problem. Current simulation models rely heavily on experimental data and empirical relationships, and thus they can be limited to the modelling of specific threat / armour combinations.

In 1995 Fleet Technology Limited was contracted to develop a BA-debris characterisation and modelling system. The result of this project was DeCaM 1.1, a software capable of characterising and modelling the BA-debris generated in ballistic penetration events. The current project focuses on the improvement and extension of the preliminary DeCaM software.

1.2 Project Objective

The global objective of this project was to develop and improve theoretical and empirical algorithms in support of the behind-armour (BA) debris characterisation and modelling system, Debris Characterisation and Modelling (*DeCaM*) Software package. Existing algorithms need to be revised to increase the accuracy of the characterisation and modelling of BA-debris. The model will be used as a stand-alone tool to characterise and model BA-debris and also implemented into DREV's Survivability/Lethality Assessment and Modelling Software (SLAMS).

Additional features also need to be implemented to increase the applicability and ease of operation of *DeCaM*, as follows:

(a) *incorporate additional penetration* algorithms,
(b) develop databases for input parameters,
(c) review and add as appropriate the following functionality:
  i) spall for non-perforating impacts,
  ii) multi-layered targets.

1.3 Project and Report Scope

These software development or extension activities were chronologically organised into three phases and associated tasks as shown in Table 1.1. To ensure a cohesive presentation of the results of this project, the information in this report is organised differently than that shown in Table 1.1. The report is presented in six sections including:

1 - Introduction
2 - Reviews
3 - Characterisation Process
4 - Modelling Process
5 - DeCaM 2.0 Software
6 - Conclusions and Recommendations

The final column of Table 1.1 relates the project tasks to the section(s) in which they are reported.

Table 1.1: Project Statement of Work Summary

Phase I	Section
I.1 Review and incorporate MPPM algorithms into DeCaM	2.0
I.2 Witness pack, projectile & target databases	5.0
I.3 Review and improve the hole matching process	3.0
I.4 Include probabilistic solution automated result accuracy feature	5.0
I.5 Perform literature review on frontal splash	2.0
Phase II	
II.1 Develop and incorporate WP penetration threshold	3.0
II.2 Characterisation and Comparison of WP BA Debris Data	3.0 / 4.0
II.3 Improve target fragmentation model	4.0
II.4 Improve DeCaM 3D animation	5.0
Phase III	
III.1 Review spall (scabbing) for non-penetrating impacts	2.0
III.2 Improve on effects of obliquity	4.0
III.3 Include multi-layer targets	4.0 / 5.0

2.0 REVIEWS

2.1 Reviews - Introduction

Literature and resource reviews are a necessary and useful first step in any engineering development process. The following sections present the results of the literature and resource reviews complete as part of this project. The reviews reported herein focus on four subject areas including:

- Target Frontal Splash
- Target Spallation Behaviour
- Characterisation of Impact and Penetration
- Multiple Plate Penetration Model (MPPM3)

References for the documents and papers reviewed in this section are presented in Section 7.0.

2.2 Target Frontal Splash

In this section, a number of papers on the topic of frontal splash are reviewed with the objective of determining the need and potential for developing a frontal splash algorithm for the DeCaM software. Frontal splash involves the ejection of target material, from the impact side of the target, in the opposite direction to the projectile's trajectory. The reason for investigating this phenomenon is to improve the penetration energy balance formulation and describe the threat posed by the frontal splash in terms of the ejected material mass velocity and trajectory.

2.2.1 Initial Damage States of Hypervelocity Impact for Tungsten Projectile on Aluminum Targets

- Sih, 1990

During a high-speed impact, a solid will undergo several stages of extreme mechanical behaviour as it deforms. In the vicinity of the initial contact, the solid behaves very much like a fluid due to the very high elevation of local pressure. To examine such behaviour, a numerical model of a flat end tungsten projectile fired at a velocity of 9000 m/s at a 5083-aluminum target plate was developed. The projectile measured 50 mm long and 14 mm in diameter. The target was 20 mm thick and 120 mm wide. The deformation, damage and phase transitions were analysed for each time step. The model was discretised with the use of 12 node iso-parametric finite elements. With the onset of failure, the mesh was resized to include the influence of local fragmentation, mass redistribution and mass detachment. As the projectile impacted the target, dynamic displacements were computed for all points on the target surface. With the displacements known, the location of the iso-energy density plane was determined for each element. The iso-stress τ and iso-strain ε pairs were used to determined the iso-energy state.

At $t = 2$ ns after impact, the surface energy density, $(dW/dA)_0$, increased in magnitude faster than the volume energy density, dW/dV, since the energy from the projectile was necessarily transmitted across the surface. It took time for the energy to spread into the target, i.e., to increase the value of the volume energy density. The lowest temperature away from the corner was more than 460 °K above ambient. However, near the corner, the melting temperature of the 5083 aluminium had nearly been reached, i.e., 1200 °K. No phase transformation was predicted since the strain rate of energy dissipation was below the critical value.

At $t = 4$ ns, none of the element had reached failure by fracture or fragmentation. At the corner of the projectile, the temperature had reached the melting point and the strain rate of dissipation had exceeded the critical value indicating that solid had been transformed to a liquid. As a result, the energy dissipation levelled off immediately. The solid/liquid interface could result in slippage and needed to be accounted for and was modelled as a narrow region that behaved neither as a solid nor as a liquid; it had its own properties which were more sensitive to changes in the local strain rate.

At $t = 10$ ns, the liquid surface bulge was predicted as the projectile pressed into the target. More solid was transformed into liquid state. The material at the centre of plate directly underneath the projectile was still in the solid phase. The surface energy density in the liquid region was extremely high and splashed the liquid and ejected the debris at a velocity that was many times greater than the impact velocity (up to ten times the projectile velocity). The ejection speed of the liquid was calculated to be 74,085 m/s (8.2 times the initial projectile velocity). As a result of the splash, the local surface and volume energy densities lowered.

At $t = 15$ ns, fragmentation was predicted in a small region where the solid broke into little pieces. The transformation of solid to liquid continued to spread to the centre plane and deeper into the target. The pressure and temperature in the liquid region were so intense that the two small regions turned into gas. The projectile remained virtually undamaged and no appreciable distortion of the target had occurred. More of the liquid debris was ejected.

The projection of the damage pattern at $t = 280$ ns indicated that two large regions of vaporised liquid were formed. Failure of the projectile by fracture began to take place in addition to phase transformation. Ejection of debris continued. The predicted pattern of damage began to take shape in the form of a crater.

2.2.2 An Aluminum Splash Generated by Impact of a Detonation Wave

- Taylor and Venable, 1968

Taylor and Venable, to observe the formation and growth of the resulting splash, present an experimental study of the hypervelocity impact between an explosive charge and an aluminium plate. The explosive charge consisted of a column of high-density gas.

The explosive charge was a 10 cm cube of composition B-3 (60% RDX and 40% TNT by weight) at a density of 1.730 ± 0.002 g/cm^3 and a velocity of 7.96 mm/μsec. The target was a 25 mm thick piece of 1100-F aluminium.

Upon impact, both the target and projectile were considered as inviscid fluids. As the impact continued, a shock wave progressed in two directions – into the projectile and into the target. At the same time, a crater was formed whose lip moved upward and outward as a well-defined wave. Typically, the wave was of secondary importance, but Harlow, Wilkins and Giroux, and Wilkins demonstrated that if the initial shock wave was not attenuated too severely before reaching the far side of the target, its reflection as a rarefaction might well cause spalling even in liquids.

The characteristic features and motion of the out-going splash wave depended upon viscosity, the prevailing dynamic shear and tensile strengths, and to some degree, upon the surface tension of the target material. They also depended strongly upon any sensible interaction between the expanding projectile material and the surface of the target.

The experimental observations clearly showed:

1. The development of the wave emerging from the crater's edge;
2. The reflected shock wave moving back into the gaseous products of the explosive;
3. The shock wave transmitted into the target material;
4. The rarefaction wave arising from the reflection of this latter shock at the free surface edge of the target;
5. The spalling behaviour of the target;
6. The flow pattern of the expanding gases as they passed over the target surface;
7. The region in which some of these gases, pushed against the outgoing aluminium wave, continually modify its progress; and
8. The air shock generated by the lateral expansion of the detonation products.

Upon impact, the explosive-aluminium interface almost instantaneously began to move at 1.72 mm/μsec and a 365 kbar shock wave was initiated and propagated through the aluminium with an initial velocity of 7.60 mm/μsec.

2.2.3 A Phenomenological Investigation of the Impact of Compact Projectiles against Plates at Speeds up to 3 km/s

- Backman and Finnegan, 1984

The impact of compact spherical projectiles at speeds ranging from 0.5 to 3.0 km/s against plates was examined to identify and characterise the internal failure processes involved in perforation and fragmentation.

An impact in the velocity range above 1 km/s generates extremes of stress and strain that become most evident in the phenomena that occur on the entry side of the plate. The entry deformations resemble the splash of an object striking a liquid surface. Fragments formed early in the process have small sizes, make up a comparatively minor part of the total fragmented mass, and tend to have extremely high velocities.

Measurements of momentum, which serve to interpret the dynamics of impact, require the consideration of back splash. Figure 2.1 illustrates measurements of back splash momentum as a function of impact speed for a mild steel plate ($T/d = 1$). Figures 2.2, 2.3 and 2.4 illustrate momentum as a function of impact speed for a mild steel sphere impacting a steel armour plate ($T/d = 1$), impacting a mild steel plate ($T/d = 1$), and impacting a 4130 steel bar ($T/d = 1$), respectively. From these Figures, it becomes apparent that for the ordnance velocity ranges of interest back splash behaviour need not be considered as it represents only a minor fraction of the total impact momentum..

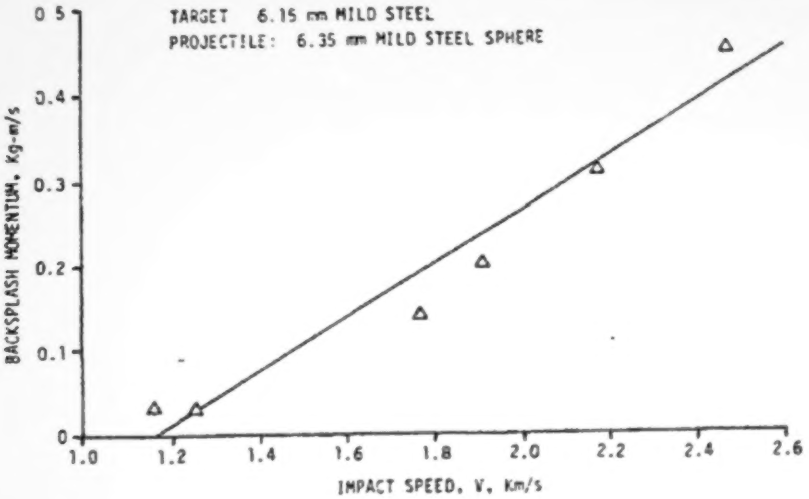

Figure 2.1: Back Splash Momentum as a Function of Impact Speed (Mild Steel Sphere, Mild Steel Plate, *T/d* = 1)

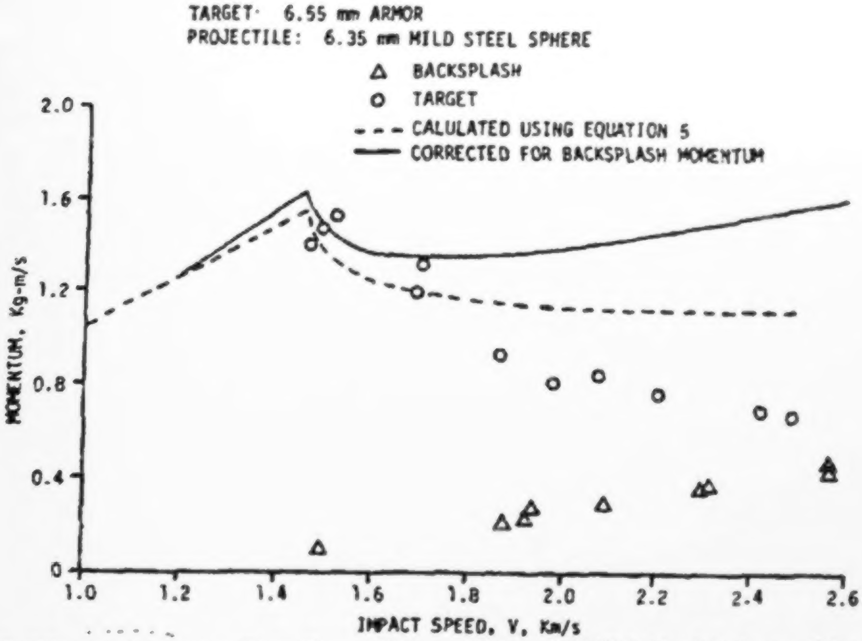

Figure 2.2: Momentum as a Function of Impact Speed (Mild Steel Sphere, Steel Armour, *T/d*=1)

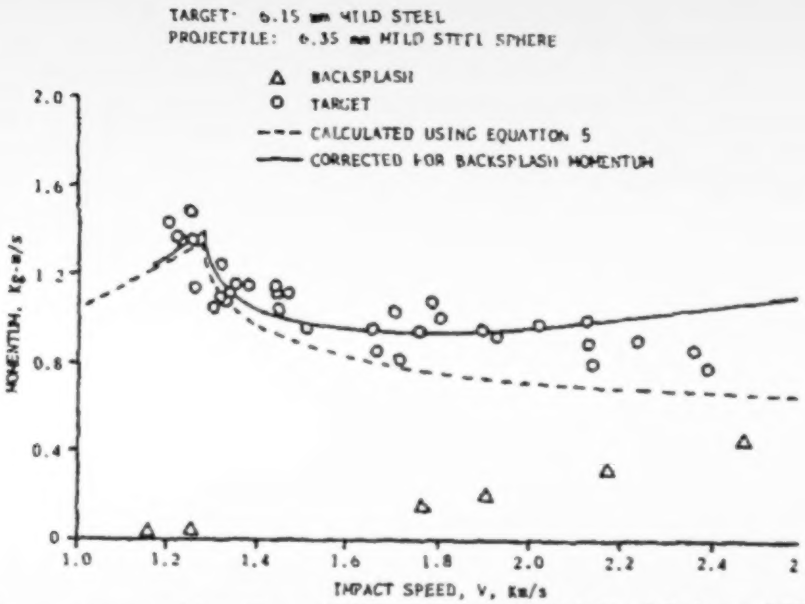

Figure 2.3: Momentum as a Function of Impact Speed (Mild Steel Sphere, Mild Steel Plate, *T/d*=1)

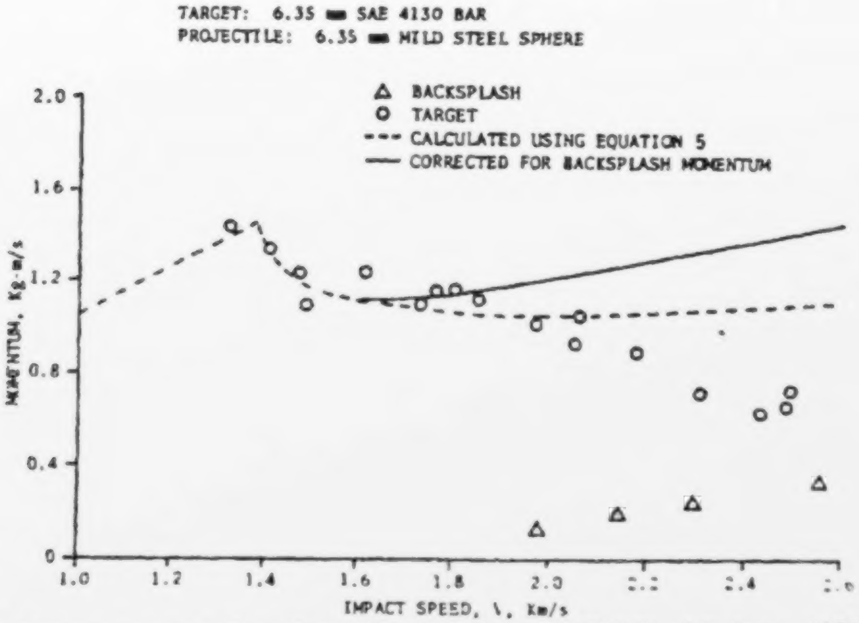

Figure 2.4: Momentum as a Function of Impact Speed (Mild Steel Sphere, 4130 Steel Bar, *T/d*=1)

Spall failure results from stress-wave interactions following reflections from free surfaces in which the reflection process changes compressive stresses to tensile stresses. The process depends on the net tensile stress wave having sufficient impulse to cause failure. In the materials and range of impact speeds of interest here, this form of fracture occurs infrequently and predominately in the less ductile materials and at the higher impact speeds.

2.2.4 An Engineering Model to Predict Perforation Damage to Plates Impacted by High Velocity Debris Clouds

- Yatteau and Dickinson, 1993

To determine the numbers and sizes of debris particles, the dispersion angles for the sphere and plate particles, and the shape of the debris clouds, experiments with multiple flash radiographs and debris particle collection in micro-crystalline wax were conducted. The wax collection technique netted 80-90% of the total possible weight. The missing mass was presumed to have been lost on the front side of the shatter plate.

2.2.5 The Mechanics of Penetration of Projectiles into Targets

- Backman and Goldsmith, 1978

Spalling is tensile material failure due to the reflection of the initial compressive transient from the distal side of the target and is a common place phenomena under explosive loading. Scabbing is similar in appearance but the fracture is produced by deformation and local inhomogeneities and/or anisotropies such as the rolling direction. High radial and circumferential tensile stresses produce petaling after passage of the initial wave occurring near the lip of the penetrator. This deformation is the result of bending moments created by the forward motion of the plate material being pushed ahead of the striker, and by inhomogeneities or planes of weakness of the target.

For thin plates, failure resulting from the tensile stress in the initial wave is calculated from the condition that the radial stress at the back surface is equal to the yield value in tension; thus,

$$v_{\Lambda} = \frac{2\sigma_{YT}\left[1+\left(\frac{h_o}{R_p}\right)^2\right](1-\nu)}{Z\left\{(1-\nu)+2\nu\left[1+\left(\frac{h_o}{R_p}\right)^2\right]^{0.5}\right\}}$$

In a similar manner spalling failure due to the reflected tensile wave corresponds to the limit velocity

$$v_{\Lambda} = \frac{\sigma_{YT}}{Z}\frac{1+\left(\frac{h_o}{R_p}\right)^2}{\left[1+\left(\frac{h_o}{R_p}\right)^2\right]^{0.5}}$$

The phenomena for thin targets, in particular the formation of a system of tiny particles on both sides of the target element, has been examined from the viewpoint of shock wave propagation. Two shock waves *S1* and *S2* propagate outward from the interface and rarefaction (tensile) waves generated at the edge of the striker cause rearward material ejection while travelling towards the centre. The pattern after reflection of *S2* as rarefaction *R3* from the distal side of the target causes the formation of a bubble of debris that grows due to the addition of material from the projectile and target. Fracture occurs when the net tensile stress exceeds a critical value, creating other waves in order to satisfy the boundary conditions of zero stress at any free surface.

2.2.6 Conclusions For Frontal Splash Review

In the papers and reference sources reviewed to develop an understanding of frontal splash, it is generally accepted that frontal splash is only a concern in high velocity impacts. Frontal splash seems to occur when impact velocities exceed a threshold velocity on the order of 1200 m/s. In addition, the momentum or significance of the resulting frontal splash increases with increasing projectile impact velocity. Since frontal splash appears to not be a concern in the range of impact conditions (velocity in particular) for which DeCaM was developed as a characterisation and modelling tool, it is recommended that the development of a frontal splash modelling tool not be pursued at this time. However, if the focus of development turns towards higher velocity (hyper-velocity) projectiles or weapon effects the significance of frontal splash might need to be considered.

2.3 Target Spallation Behaviour

The term "spall" refers to the internal material failure as result of cavitation due to dynamic stress waves. When a projectile strikes a target, transient stresses are generated and propagate through the target material away from the impact site. The compressive stress wave reflects from the backside or free-surface of the plate as a tensile wave. Whether or not spall occurs depends on the stress levels caused by the impact and the fracture toughness of the target. Should spalling occur, damage or injury to personnel and equipment may result due to target debris even though the target has not been perforated by the projectile.

There are two forms of spalling: ductile and brittle. Spallation in ductile materials is controlled by elasto-plastic deformation around existing and nucleated micro-voids which dynamically grow and coalesce to form the spall plane. Spallation in brittle materials is controlled by dynamic micro-crack growth with plastic deformation around the crack tip. These cracks eventually coalesce to form the spall plane.

Some of the models reviewed here were developed for ductile spalling, others for brittle spalling, and others are for either ductile or brittle spalling. Generally, the models were developed by interpreting experimental results and were tested and verified against experimental results.

Spallation fracture analysis started with an explanation of scabbing (or spalling) by reference to stress waves in bars, then electronic measuring devices were used to study such waves. In the early 1950's, the detailed studies on spall fractures were carried out by crystallographic examination of the spall damage. In the 1960's Broberg introduced the concept of the development of micro-fractures to explain the spallation failure mechanism. He postulated that when the tensile stress reaches some critical value micro-fractures start to grow, the number of which depends on the stress level and that scabbing is produced when the micro-fractures join together to form the spall plane. These ideas provided a good basis for the work carried out in the following year.

Refined microscopic theories were put forward to explain the phenomenon and incorporated into hydrocodes in order to predict spallation. In keeping with Broberg, it is accepted that spallation in ductile materials is dominated by localised elasto-plastic deformation around existing and nucleated micro-voids which dynamically grow and coalesce to form the spall plane. Spallation in brittle materials is controlled by dynamic micro-crack propagation with plastic deformation confined to the small region around the crack tips. The cracks eventually coalesce to form the spall plane.

The technology of micro-structure examinations has been greatly developed to study the details of the damage process associated with spallation. Various statistical laws for the nucleation and growth of micro-damage were proposed. For example, Seaman et al. 1976 put forward their nucleation and growth (NAG) model after a series of experiments involving detailed microscopic examinations. Since then, the fundamental mechanisms of spall nucleation and growth concerned about the mean micro-void or crack size were developed. These include visco-plastic constitutive modelling of high strain-rate deformation and material damage. To avoid the difficulties caused by the data requirements of the micro-void or micro-crack models and the effects of element size on numerical results, macroscopic description based spallation process and energy-based spall models have been developed and presented.

A review of available literature identified ten spall fracture formation models. Mainly concentrated on the models after the NAG model. The sections following provide a brief theoretical review of the spall fracture models which were identified in the literature review. Each section provides an outline of the features of a model type and identifies the sources in which the development was described.

2.3.1 Ductile Material Models

2.3.1.1 Ductile Hole Growth under Uniaxial Stress Conditions

- Johnson, J. N. 1981

One of the basic spallation fracture models is the nucleation and growth (NAG) model of spall fracture. The NAG model has the property of having sufficient generality to include the statistical distribution of one or more target material variables such as porosity, void density, but requires numerous phenomenological constants that are difficult to obtain.

In his work, Johnson developed a microscopic model of ductile hole growth which relates the material porosity (an internal state variable) to its initial value, and the time history of the tensile pressure (or mean stress). He also developed a single scalar parameter model representing the rate-dependent plastic flow properties of the solid material surrounding the voids. The model is expressed mathematically in a scalar form, involving only the mean stress, that can be used in a general multidimensional situation.

The model developed by Johnson originated from the model of Carroll and Holt (1972). In their model, the void collapse in porous ductile materials lends itself directly to a theory of void growth under tensile loading conditions. It differs from Johnson's model, in that the pressure is negative. Additional rate-dependent plastic flow terms and internal gas pressure were also present in the original development.

One of the major differences in the Johnson model compared with other microscopic descriptions of ductile hole growth, is the fact that the mean tensile stress around a single pore is applied at a finite radius. The model leads directly to a threshold mean stress as a function of the distension. The description thus tends to bridge the gap between the low-damage and complete separation regimes of spall fracture.

Johnson's model only deals with the uniaxial-strain conditions associated with spallation and produces a predominantly isotropic stress state with a smaller deviatoric effect added on.

2.3.1.2 The Growth of Microvoids Under the Action of HydroStatic Stress.

- Cortes, R., et. al. 1992.

Experimental evidence suggests that there exists a threshold tensile stress at which spall initiation takes place and this theory may be applied to any "ductile" material.

Cortes et al. analysed in detail the plastic void growth process which takes place under extremely high rates of loading. Their basic assumptions for the analysis were taken from the previous model for perfectly plastic porous materials presented by Carroll and Holt (1972) and later extended by Johnson (1981). The voids were assumed to be spherical and to grow plastically under the action of an externally applied macroscopic hydrostatic stress. Since the inclusion of triaxiality in the void expansion model would complicate the problem and it is understood that under extremely high loading rates the hydrostatic stress is the leading stress component in the spall fracture process, the model assumes a uniaxial-strain condition. A general relationship is derived between external hydrostatic stress and material porosity, starting with the simple assumptions of Carroll and Holt's. The influence of material viscosity, strain hardening and thermal softening effects on the dynamic void growth equation are ascertained.

The researchers found that material viscosity, especially in the high strain-rate range, has a great influence on the dynamic tensile strength of aluminium. Strain hardening also has an important influence though less marked than material viscosity. In particular, for aluminium the effect can be disregarded in practice. For greater amounts of work hardening, such as that exhibited by copper, the degree of influence in the dynamic tensile strength is greater. The thermal softening by itself has a negligible effect on tensile strength under high loading rates, for both copper and aluminium, due to excessively localised heat generation near the surface of the voids.

2.3.1.3 Numerical Modelling of Ductile Spall Fracture

- Cortes, R. and Elices, M. 1991 & 1995.

The spall fracture is associated with the complicated concurrence of nucleation, growth and coalescence of micro-defects, which can depend on both the pre-existing and the evolving microstructure.

Cortes investigated the influence that a combined state of hydrostatic and deviatoric stresses may have in the spall strength of ductile materials for the case of void growth controlled fracture. He analysed in detail the plastic void growth process which takes place under extremely high rates of loading and modified a procedure previously used by Gurson (1977) to derive the macroscopic yield locus of porous materials, in order to embody the inertial effect.

Starting with Gurson's formulation, expressions for macroscopic stresses are derived as a function of the macroscopic volume stress, the volumetric macroscopic deformation rate and the macroscopic deviatoric strain rate tensor in a system of principal axes of strain. To include the inertia terms, Gurson's formulation was modified with the inclusion of the associated energy dissipation. A more general expression considering the influence of a linear viscosity term was developed.

In the second paper, the formulation by Gurson for perfectly plastic materials was expanded to include a non-linear viscous term.

It has been discovered that, when the volumetric expansion rate is more important than the deviatoric strain rate then, for void growth controlled dynamic fracture, the spall strength may be affected by the deviatoric field and, under certain circumstances, may cause a considerable decrease in the strength of the material. On the contrary, when the deviatoric strain rate is very high, stresses required to overcome the inertia effects associated with the deviatoric stain rate field may become very large, in such a way that plastic void growth may be very difficult. Under such conditions it is expected that a different mechanism, such as void nucleation should be the controlling factor in dynamic fracture.

The model with a non-linear viscous term was applied to spall experiments in aluminium. The damage mechanism leading to fracture of the tested specimens was the nucleation and growth of micro-voids. It was shown that inclusion of a non-linear viscous term is essential to obtain good agreement between analysis and experiment.

2.3.1.4 A Void Growth Relation for Ductile Porous Materials under Intense Dynamic Loading

- Zheng, J. and Wang, Z.-P. 1995 & 1997

Dynamic ductile fracture with different loading conditions, such as high speed impact, explosive loading, dynamic tension of smooth or notched bar specimens, is a consequence of the nucleation, growth and coalescence of voids in a triaxial stress field. Dynamic ductile damage modelling is much more difficult than modelling ductile damage under static loading conditions. The inertial effects, rate-dependence and thermal influence from rapid plastic deformation need to be considered under intense dynamic loading.

Zheng and Wang developed a void growth relation model by means of the energy principles, in which the inertial effects, rate-dependence and the contribution of the void surface energy were considered. The inertial effects in an intense dynamic loading scenario are a major concern yet they are commonly neglected due to the complexity they introduce to damage modelling formulations. This damage accumulation model explicitly considers material viscosity describing the rate sensitivity of the target materials to differentiate dynamic and quasi-static ductile damage accumulation. This modelling approach also considers the net effects of the applied external stress, the change in void surface energy, work hardening rate and the target material's yield strength.

They started with the assumptions adopted from Johnson's model and applied them to the surface energy equilibrium equation with the matrix material being assumed to be linear work-hardening and viscoplastic. The threshold stress expressions for dynamic growth of voids in general dynamic loading conditions were obtained. If the contributions of the change of the void surface energy and material work-hardening, as well as the action of the external deviatoric stress are neglected, the result is the same as Carroll and Holt's.

In the second paper, the influence of inertial, rate-sensitive as well as thermal effects on the void growth at high strain rate in a thermal-visco-plastic solid were investigated by means of a theoretical model. The authors compared the numerical results of Johnson's model and theirs, and suggested that the thermal effect generated by high speed deformation greatly influence, the void growth, which must be considered in the high strain rate case.

The conclusions from both papers are that the thermal effect and the inertial effect greatly influence the behaviour of the void growth at high strain rate. The work showed that the inertial effect is no longer significant for a strain rate less than $10^3 s^{-1}$, where the visco-plastic effect becomes dominant. The higher the loading rates, the greater are the inertial effects.

2.3.1.5 A Void Growth-Based Failure Model Based on A Pressure-Dependent Yield Criterion

- Rajendran. A. M., Dietenberger, M. A., and Grove, D. J. 1989.

Rajendran et al. present a void nucleation and growth-based constitutive and failure model to describe spallation-type failure processes in ductile materials under dynamic loading conditions. The model is three-dimensional and based on micro-mechanical parameters. Strain rate dependency on the strength (flow stress) and the pressure effect on the plastic flow were also included in the model formulation.

The model includes four phases: (1) behaviour of the initially intact material; (2) description of the damaged material; (3) nucleation behaviour; and (4) coalescence of the damage leading to material failure.

The matrix material was modelled with the state variable based visco-plastic constitutive equation of the Bodner-Partom model (Bodner, Partom 1975). The Bodner-Partom model parameters were determined from the split Hopkinson bar stress-strain data at three different strain rates and the steady-state value of the Hugoniot elastic limit from the plate impact experiments.

The authors evaluated the effects of various model parameters on the numerically simulated failure process.

2.3.2 Brittle and Brittle-Ductile Material Models

2.3.2.1 Evolution of Microcracks in Brittle Solids under Intense Dynamic Loading

- Wang, Z. P. and Lam, K. Y. 1995.

Seaman et al. (1985), on the basis of experimental observations and measurements, presented a continuum model for dynamic tensile micro-fracture and fragmentation using a statistical approach.

Wang et al. established a simple dynamic brittle fracture model using the principle of energy balance in which a few parameters were required. The influence of inertial effects and elastic energy on micro-crack growth was taken into account in the kinetic equation for the micro-crack.

Starting with the assumption also adopted by Perzyna (1986), applying the energy principle that the work done by an externally applied tensile stress equals the increments of the system energies, the expression for the critical condition for micro-crack growth under high-rate tensile loading was derived.

The conclusion is that the rate dependence of micro-crack growth and the rate-dependence of the threshold tensile stress for micro-crack growth under high-rate loading are two major features that are distinct from that of quasi-static loading. There is a critical stress condition for the dynamic growth of a micro-crack and this threshold stress for micro-crack growth is strain rate dependent only when the average strain rate is greater than 10^5 s^{-1}.

2.3.2.2 A Simple Non-Local Spallation Failure Model

- Al-Hassani,S., Chen,D., Sarum,M. 1997

The authors consider that, in application, a full knowledge of material microstructure during spalling is not necessary. There is evidence that, in certain cases, spall properties are not very sensitive to micro-structural details of the material.

A new, simple, non-local failure model was presented in their work. The model was applicable to both ductile and brittle materials and was based on a macroscopic view of the spallation process while conforming with the microscopic nature of the physics of the phenomenon. The model was incorporated into one and two dimensional hydrocodes and applied to the problem of planar plate impact test.

The methodology for the theoretical model can be summarised as follows:

1) The gross damage is defined with the assumption that the solid constituent is incompressible when the tensile pressure reaches a critical value.
2) The gross damage is evaluated using the conservation equations and constitutive equations for the finite difference cells. Additional damage evolution laws and strength functions are therefore considered unnecessary on the assumption of incompressibility.
3) The use of gross quantities to characterise the average continuum behaviour of the material during damage evolution makes the results of numerical simulation less susceptible to the influence of mesh size as compared to micro-mechanical models.

The model only requires two parameters: the critical tensile pressure and the critical gross porosity. A reasonable estimate of the two parameters can be obtained as the exact determination of the two parameters depends on the comparison between numerical simulation and experimental record of the planer spall test. The approach avoids the complexities of soft recovery and elaborate specimen examination.

2.3.2.3 Crack Straining-Based Spall Model

- D. Chen,S., A-Hassani,M. Sarumi, X. Jin 1996

In view of the fact that mean void growth-based ductile spall models are successful, the authors have explored the possibility of presenting an equivalent mean crack growth-based failure model for brittle spall. They indicated that it remains to be demonstrated how an appropriate mean crack size was chosen to identify the brittle spall strength as the threshold pressure for crack growth and they found that there seems to be no basis for a mean crack growth-based spall model which avoids nucleation considerations.

The authors present a crack straining-based spall model which assumes that the inelastic volumetric strain caused by the relaxed tensile pressure at a critical fragment volume is the main factor governing the solidity evolution during the process of coalescence and fragmentation. This allows for the modelling of brittle spall to be compatible with that of ductile spall.

The crack straining-based spall model was developed by:

1) expressing the solidity evolution in terms of inelastic volumetric strain rate;
2) determining the inelastic volumetric strain rate according to the crack opening strain and the crack shear strain;
3) considering a crack straining-based spall model avoiding nucleation and growth considerations; and
4) evaluating the relaxation of tensile stress ignoring the inelastic volumetric strain of the matrix material.

By using the crack strain-based spall model, the modelling of brittle spall is made compatible with equivalent ductile spall modelling. The comparisons between the experimental and calculated velocity history of the free surface of the target in the planar impact of flat plates are very good.

The spall model requires only two parameters: a spall strength and the critical solidity.

2.3.2.4 Energy-Based Spall Theory

- Buchar, J. and Krejci, J. 1994 & 1997

The evaluation of spall in a body subjected to dynamic loading involves co-operative nucleation, growth and coalescence processes that depend on both the pre-existing and the evolving microstructure of the spalling body. One of the approaches to the spall description that exists is the energy-based spall theory.

The authors present further experimental verification of the energy-based spall theory (Grady 1988). The theory uses a balance of the driving energy in the stress wave loading and some continuum measure of fracture dissipation such as fracture toughness, surface tension, etc., to describe spall fracture. Experimental results from nine different steel microstructures indicated that there was a dependence of the spall strength on the strain rate and that this dependence exhibited features that would suggest a transition in the spall fracture mode from brittle to ductile.

The experimental results indicate that the logarithm of the spall strength increases linearly with the logarithm of the strain rate up to some critical value, $\dot{\varepsilon}_c$, and then remains constant.

The data on the dynamic (spall) strength for more than 30 steels were testified with the energy-based theory and some modifications to the theory were suggested.

2.3.2.5 Computational Models for Ductile and Brittle Fracture

- Seaman,L., Curran,D.R., Shockey,D.A. 1976.

The well known nucleation and growth (NAG) model was first presented by these authors establishing the basis of the micro-void spall fracture model.

Curran and co-workers made detailed microscopic observations before and after shock-wave loading (both ductile and brittle solids) as a basis for nucleation and growth (NAG) models of spall fracture. The models describe the processes of nucleation of cracks or voids, the growth of these cracks or voids, and the effect of the growing damage on the stress-strain relations. The damage in the models is related only to the stress and stress duration and is therefore independent of the type of loading.

In the model, the fracture phenomena to be treated computationally are first introduced through experimental examples. The results of the calculations include number and sizes of cracks, voids, or fragments as a function of position in the ductile or brittle material.

From reviewing typical experimental fracture cases, the authors concluded that:

1) A range of damage is possible; there is no instantaneous jump from undamaged to fully separated.
2) Damage grows as a function of time and the applied stress.
3) As the damage occurs, the stiffness of the material decreases; therefore, the wave propagation characteristics change.
4) Even incipient damage levels are important.

The models incorporate the following phenomena:

1) Nucleation of cracks or voids as a function of stress level and stress duration.
2) Growth of cracks or voids as a function of stress.
3) A range of void or crack sizes at all stages of fracture.
4) Coalescence of crack to form fragments.
5) A range of fragment sizes.
6) A smooth transition from no damage through fracture to full separation.

The damage is described by statistical distribution of cracks or voids, not by individual cracks or voids. After nucleation, the voids or cracks grow at a rate dependent on the stress (or stress intensity, K_I) level, duration of loading, and the size of the void or crack. When the number and size of cracks meet a coalescence criterion in the brittle model, the cracks begin to join and form isolated fragments. For ductile fracture, the voids continue to increase in size until the void fraction exceeds a critical value and separation occurs.

Ductile Fracture

The experimentally observed ductile fractures in aluminium, copper, armco iron and novaculite revealed that fracture occurred through the nucleation and growth of nearly spherical voids. The observed voids were measured and counted and assembled into number versus radius distributions.

When the ductile material is undergoing fracture, the computational fracture of ductile material contains three parts: 1) nucleation, 2) growth, and 3) pressure-volume and stress-volume relations.

Brittle Fracture

When the brittle material is undergoing fracture, the computational fracture of brittle material contains three parts as well: 1) crack opening, 2) crack nucleation, and 3) crack growth.

The NAG model was constructed from detailed observations of the dynamic fracture processes in a wide range of materials. The observations show the nucleation and growth of voids or cracks. Although the stress-strain relations for material undergoing fracture and the treatment of coalescence and fragmentation are very approximate in the models, they are still shown to adequately represent the dynamic fracture processes over a wide range of material types, stress levels, and load duration.

2.3.3 Spall Fracture Models Summary and Comparison

In the previous sections ten spall fracture schemes were identified and described and in this section their unique qualities are outlined. The spallation fracture model summary table which follows is used to compare the models which were previously described. The table is divided into six columns presenting the following information:

- Model: Provides the number corresponding to the order in which the models were presented in the previous sections. The listing below relates each model number to the section in which it was presented.

Model	Section	Model	Section
1	2.3.1.1	6	2.3.2.1
2	2.3.1.2	7	2.3.2.2
3	2.3.1.3	8	2.3.2.3
4	2.3.1.4	9	2.3.2.4
5	2.3.1.5	10	2.3.2.5

- Model Type: Characterises each model according to its basis of development, describes the general circumstances where the models were established and loading conditions.
- Basis: Describes the theoretical basis of the model (e.g. fracture mechanics, energy balance or force equilibrium) and indicates preceding models.

- Data Type: This column describes the data and used by the model in the description of the spallation fracture.
- Calibration Source: Identifies the materials and testing approach used in the development of the model.
- Application Specifics: Provides a summary of the features of each model (i.e. the nature of the assumed material behaviour).

Table 2.1: Ductile Material Models

No.	Model Type	Basis	Data Type	Calibration Source	Application Specifics
1)	-analytic model -microscopic damage -ductile void growth	-Carroll and Holt's model	-void growth relation -no inertial/thermal effect -uniaxial stress	-plate-impact experiment (PMMA plate)	-porous perfectly plastic materials -numerical results: stress, particle-velocity, void-growth history
2)	-analytical model -microscopic damage -hydrostatic stress and high loading rate	-Carroll and Holt's model -Johnson's model.	-void growth relation -material viscosity, strain hardening and thermal softening effects -triaxial stress	-numerical analysis -plate-impact test (copper and aluminium)	-plastic material with viscosity -strain hardening influence -Result: dynamic void growth process equation
3)	-analytical model -macroscopic constitutive equation -hydrostatic and deviatoric stresses	-Gurson's model -Carroll and Holts' model	-void growth relation -with inertial effect -linear or non-linear material viscosity -triaxial conditions	-numerical analysis -plate-impact tests (aluminium)	-plastic material grow dilative and distortedly -linear or non-linear viscosity effects
4)	-theoretical model -microscopic damage -high dynamic loading	-Johnson's model. -Energy principles.	-void growth relation -with inertial effect -linear material viscosity -applied external deviatoric stress -triaxial conditions.	-numerical analysis -plate-impact tests (aluminium alloy and mild steel)	-ductile porous material -inertial effects, -material viscosity effect -contribution of void surface energy
5)	-theoretical dynamic failure model -microscopic damage	-Bodner-Partom (BP model). - Pressure-dependent yield criterion	-yield function -three void nucleation parameters and three void growth parameters	-numerical analysis -plate-impact tests (OFHC copper)	-strain rate dependent failure model -one-, two- three-dimensional model -improved yield function

Table 2.2: Brittle and Ductile Material Models

No	Model Type	Basis	Data Type	Calibration Source	Application Specifics
6)	-analytic model -micro-crack damage -dynamic loading	-energy balance principle -Perzyna assumption	-micro-crack growth relation -inertial effect -elastic energy effect	-numerical analysis (steel-like material)	-brittle cracked materials -threshold stress dependent strain rate when strain rate is great than 10^5 s^{-1} -kinetic equation of micro-crack
7)	-New analytic model -non-local damage	-non-local view of spallation process -energy conservation	-gross damage equation -critical tensile pressure, critical gross porosity	-plate impact tests (uranium, copper, armco iron) -numerical analysis	-for practical engineering material -one-,two-, three-dimensional hydrocode -only two parameters required
8)	-analytic model -microscopic damage	-Curran and Seaman's model -Addessio and Johnson's model	-conservative relation -relaxed tensile pressure at a critical fragment volume	-plate impact tests (armco iron, uranium, copper) -numerical analysis	-brittle spall compatible with ductile spall -strain hardening effect
9)	-analytic model -microstructure damage -dynamic load	-energy conservation -Cherepanov's concepts	-spall strength relation -strain rate effect	-plate-impact tests (more than 30 steels)	-strain rate effect on spall strength -improved energy-based spall theory
10)	-analytic models -microscopic damage	-comparison of experimental and theoretical results	-void growth relations	- plate impact tests (aluminium, copper, armco iron, novaculite)	-dynamic fracture of ductile and brittle material -one-, two-dimensional geometry

2.3.4 Concluding Remarks

A literature review of existing target spall models was performed and ten distinct modelling efforts were identified. The models were summarised individually and tables comparing the characteristics of each model were assembled. The objective of the review was to identify modelling techniques which could easily be implemented in the DeCaM software to describe target spall produced by non-penetrating ballistic impact events. The results of the review may be summarised as follows:

- Most of the spall models are based on an assumed material ductility. Brittle materials produce spall based on a fracture process while ductile material spall develops based on a void nucleation and growth process. In either case, information concerning the initial void or discontinuity distribution is generally required.
- The reviewed models were predominantly developed for use as failure criteria or material behaviour limits in hydrocodes.
- The models focus on micro-mechanical behaviour and thus do not provide information on the distribution and dissipation of the applied pressure wave and thus an assumption as to the stiffness of the target support and the pressure wave distribution would be necessary.
- In general, the model development efforts have been developed based on the observed behaviour of materials other than conventional armour steel.

It is suggested that the most promising models for further development within DeCaM include:

- Buchar, J. and Krejci, J., "Energy-Based Spall Theory" (Section 2.3.2.4), and
- Seaman,L., Curran,D. R., Shockey,D.A., "Computational Models for Ductile and Brittle Fracture" (Section 2.3.2.5).

However, the development and implementation of a simplified formulation for the prediction of spallation would be a significant effort, which cannot be supported under the current contract.

2.4 Characterisation of Impact and Penetration

2.4.1 Experimental and Numerical Simulation of High Velocity Impact on Steel Targets

- Hohler *et al.*, 1993

This paper discusses the geometry of behind armour debris clouds generated by penetration events with impact velocities from 2 to 3 km/s. The study includes both normal and flat on impacts of cylindrical steel fragments ($L = 20.7$ mm and $D = 20$ mm). Thick shielded targets with thickness to projectile diameter ratios (t/D) of 1 and 1.5 were considered.

The crater geometry was roughly hemispherical and the crater lips were broken out. This indicated a relatively brittle behaviour. Some projectile material remained in the crater ground area, the amount of which decreased with velocity.

At the beginning of the debris cloud formation, it exhibited a flat shape that was determined by the origin of the cloud material from all over the impact region. During the expansion of the cloud, it became roughly spherical. The fragmentation increased with velocity and was smaller with increasing target thickness. There was strong spallation damage at the target rear side that confirmed the brittle behaviour. The spallation ring limited the boundary line of the cloud near the target rear side. This ring was ejected.

The damage to the witness plate consisted of an inner area of high debris concentration with diameter d_{min} and an outer area of low concentration with diameter d_{max}. The inner area was impacted by the main part of the debris cloud whereas the particles in the outer area were partly coming from the rear of the cloud. The geometry of the cloud is characterised by the ratio of the debris cloud's distance from the plate (x) to its maximum lateral diameter (b). A plot of x/b as a function of x demonstrates that x/b increases with x close to the target. The ratio of x/b has a value of unity at about $x = 4D$ and converges to a value of 1.1 to 1.2 further from the target. This was a result of the fragments not being ejected from a central point in the target. The origin of the fragments was spread over the total damage area in the target and caused a dependence of x/b on x near the target rear side. At larger distances, this dependence disappeared and x/b became constant, which meant in this case, a roughly spherical expansion of the cloud. x/b was nearly independent of the residual velocity of the cloud front. Only a small decrease of x/b with impact velocity was observed. This indicates that the debris cloud lateral expansion velocity is not strongly related to impact velocity.

2.4.2 An Analytical Model of Hole Size in Finite Plates for Both Normal and Oblique Hypervelocity Impact for all Target Thicknesses up to the Ballistic Limit

- Baker and Persechino, 1993

This paper presents an empirical model for the hole size produced by normal and oblique hypervelocity impact into finite plates based on the experimental investigation of aluminium spheres impacting aluminium plates. The model illustrates that the target thickness that divides the thin target regime from the thick target regime is a function of velocity.

For small values of t/d (thin plates), the hole size increases with increasing target thickness. For large values of t/d (thick plates), the hole size decreases with increasing target thickness. The transition region between thin and thick targets has never been clearly defined quantitatively.

For very thin targets, i.e., $t/d \leq 0.035$, the hole size is independent of velocity. While the model developed in this study may not be directly applicable, the trends developed here may be illustrative.

2.4.3 Dimensionally Scaled Penetration Experiments to Extract Projectile Sizes from Space Exposed Surfaces

- Hörz *et al.*, 1993

This paper experimentally examines the relationship between the diameter of the penetration hole, D_h, the foil thickness, T, and the projectile size, D_p, while maintaining a constant impact velocity. The impact experiments were conducted with soda-lime glass projectiles (50, 150, 1000 and 3175 μm in diameter, D_p) and aluminium (1100 series) and Teflon (FEP) targets with thicknesses ranging from $D_p/T << 0.1$ (infinite halfspace) to $D_p/T > 100$ (thin films).

The craters and penetration holes found in the "thick" $D_p/T < 1$ aluminium targets typically had diameters several times the size of the projectile diameter. The thinner the aluminium targets became, the small the hole diameter became until sufficiently thin foils ($D_p/T > 50$) allowed D_h to approach D_p. For $D_p/T < 1$, the diameters of the craters and penetrations remain essentially constant if measure at the initial aluminium target surface. The diameter of the penetration hole underwent a dramatic change from sizes smaller than D_p, at or close to the ballistic limit ($D_p/T = 0.3$), to dimensions measured in multiple projectile diameters at $D_p/T > 0.35$. The depth of the crater also increased when incipient spallation occurred and there were systematic changes in the slope(s) of the crater walls until $D_p/T > 0.5$ was reached. It takes $D_p/T > 1$ to generate penetration holes that are smaller in diameter than the standard crater, regardless of where the actual hole diameter is measured (at the target surface or at the narrowest points). This decrease in D_h was systematically related to T until a threshold foil thickness was reached where $D_h = D_p$.

The morphology and dimensions of the crater lips develop in a fashion that is systematically related to the aluminium target thickness as well. The lip diameter decreases with decreasing foil thickness. The average extent of the entire lip decreases as T decreases, as does the height of the lip above the original target surface.

The Teflon target responded to shock stresses largely by brittle failure yielding crater and penetration-hole morphologies that differed dramatically from those of the aluminium target. The Teflon underwent significant spallation on both the front and rear surfaces. The crater was difficult to define due to highly irregular failure of the Teflon. The walls and bottoms of the crater are formed by highly irregular protrusions that are associated with a substantial set of radial cracks that approach a crater radius in length. The penetration holes are systematically related to D_p/T, no matter what target material, and that they form a morphologic continuum over a wide range of D_p/T, including a smooth transition from cratering to penetrations in massive targets.

The average frontal spall zone remained relatively constant at all $D_p/T < 0.75$ and resembled a standard crater. For penetrations at $D_p/T = 0.15 - 0.5$, there was a slight increase in Ds, whereas a substantial decrease in Ds occurred at $D_p/T > 0.75$ which was simultaneously accompanied by a rapid decrease of the relative spall width (D_s/D_h). Rear surface spallation processes were already occurring in the Teflon targets at $D_p/T = 0.15$ and were substantial at $D_p/T > 0.2$. At $D_p/T = 0.2 - 0.5$, the rear-surface spallation was more pronounced than that of the front side. The rear-surface spallation at $D_p/T > 0.5 - 0.7$ was so prominent that it controlled the physical size of the penetration hole and produced a distinct maximum for D_h at $D_p/T > 0.6 - 0.7$.

2.4.4 Characteristics of Debris Clouds Produced by Hypervelocity Impact of Aluminum Spheres with Thin Aluminum Plates

- Piekutowski, 1993

This paper examines the effects of variations in bumper-plate thickness, sphere diameter and impact velocity on the shape and velocity of the debris cloud produced with the impact of aluminium spheres with thin aluminium plates. The evaluation was limited to:

1) *t/D* ranging from 0.026 to 0.424 for impact velocities of 6.7 km/s and
2) *t/D* ratio of 0.049 for impact velocities of 3.77 km/s to 7.23 km/s.

Various thicknesses of 1100-O, 2024-T3, and 6061-T6 aluminium plates, ranging from 0.25 mm to 4 mm were used as bumpers. 2017-T4 aluminium spheres of 9.53 mm, 6.35 mm and 12.7 mm diameter were used as projectiles.

The debris cloud consisted of an ejecta veil, an external bubble of debris, and a significant internal structure composed of three distinct elements – front, centre and rear elements. The ejecta veil was ejected from the impact or front side of the bumper and consisted almost entirely of bumper fragments. The expanding bubble formed on the rear side of the bumper and consisted of bumper debris. A structure (bumper plug) composed of projectile debris was located inside and at the front of the external bubble of bumper debris.

For a 6.7 km/s impact, the front element consisted of finely divided molten droplets of bumper and projectile. The disk-like centre element was composed of numerous splintery projectile fragments and a single large chunky projectile fragment located at the centre of the disk and on the debris cloud centre-line. The rear element was a hemispherical shell of fragments spalled from the rear surface of the sphere. The central fragment represented the most severe threat to rear wall integrity (Piekutowski, 1992a).

As *t/D* was increased form the minimum value, significant expansion of the internal structure of the debris cloud was noted. The following changes in internal-structure morphology also occurred as *t/D* was increased: (1) diameter of disk-like centre element increased, began to "bend over" at *t/D* of 0.084 and formed a flat-bottom bowl at $t/D = 0.163$; (2) radial expansion of the hemispherical shell of spall fragments at the rear of the internal structure increased; and (3) the size of the fragments in the centre and rear elements decreased. The front element of the cloud did not vary significantly in size, shape or radiographic density until $t/D > 0.102$. At $t/D =$ 0.163 and 0.234, this element was a spherical sector and did not exist when the ratio *t/D* was 0.424.

The effects of impact velocity with constant *t/D* were examined next. At 3.77 km/s, a spalled region developed inside the projectile, forming a shell that was loosely attached to the rear of the sphere. A slight flattening of the front of the sphere was also noted. As impact velocity increased, fragmentation of the projectile and an increase in the axial and diametral expansion of the internal structure was noted.

Growth of the internal structure of a debris cloud was sensitive to both *t/D* and impact velocity, and increased as both parameters increased. Development and growth of the front element was most sensitive to impact velocity.

The normalised axial debris cloud velocities along the cloud centreline decreased as *t/D* increased. An increase in the axial dispersion was also observed. The velocity at the centre of mass of the debris cloud decreased as *t/D* increased. The normalised axial and diametral velocities at the outer tips of the central fragment showed a decrease in the axial velocity and an increase in the diametral velocity as *t/D* increased. As the impact velocity increased, little change was in the axial velocity; however, there was a moderate increase in the diametral velocity of these points.

Growth of the debris cloud internal structure occurred as *t/D* and impact velocity increased.

2.4.5 Experiments on the Hypervelocity Penetration of Thin Aluminum Sheets

- Reschauer and Igenbergs, 1993

This paper examines the hypervelocity penetration of thin aluminium sheets (8 to 125 μm thick) impacted by glass spheres with diameters of 20 to 60 μm at 10 to 15 km/s velocities.

The experimental results illustrated typical features of a hypervelocity impact. A steep, overturned lip rimmed both the front and rear side of the hole. Sometimes the rear side showed two or more rows of lips inside the outer steep lip and had a rough and crumbly looking surface between the lips. This feature is caused by spallation. The targets penetrated were neither semi-infinite nor thin compared to the diameter of the projectile and therefore, the transition from the crater to the hole generation process was visible if the impacts were close to the ballistic limit. The further beyond the ballistic limit an impact occurred, the more cylindrical the penetration hole was and the smaller the crater lips were, compared to the hole size.

The impact velocity influenced the shape of the penetration hole if the projectile diameter and target thickness were of the same order of magnitude. The faster the impact occurred, the more conical the penetration holes were. This may correspond to an increasing ratio of front-to-rear-side ejecta mass.

Spallation occurred within a small range rather than at a certain impact velocity. The spallation generated by the shock wave occurred closer to the rear target surface with an increasing shock wave amplitude. The projectile penetrated deeper into the target until the rear target surface was disrupted and more material was ejected to the front side of the target.

2.4.6 An Engineering Model to Predict Perforation Damage to Plates Impacted by High Velocity Debris Clouds

- Yatteau and Dickinson, 1993

This paper describes experiments and the development of a model to predict damage to metallic plates impacted by high velocity, multi-particle debris clouds. The experiments involved single 6.9 g hardened steel spheres fired at a mild steel shatter plate at speeds near 1.5 and 2.0 km/s to generate the debris cloud. Impact velocity was controlled and the witness plate was placed at increasing distances, *S*, behind the shatter plate to observe the effects of debris particle dispersion on plate damage and focuses on the variations, with plate sizing, in the diameter, D_h, of the central region removed from the witness plate. The central hole model compares the post impact kinetic energy distribution to the free impact residual kinetic energy in an equivalent plate impacted by an $L/D = 1$ steel cylinder, at the ballistic limit velocity.

The witness plate damage due to the debris cloud from a high velocity impact is a circular or elliptical pattern of individual craters and/or holes with an areal density that decreases with increasing radius from the centre of the pattern. Hypervelocity impact debris clouds can also cause material to be spalled from the rear surface of the plate.

Additional experiments with multiple flash radiographs and debris particle collection in micro-crystalline wax were conducted to determine the numbers and sizes of debris particles, the dispersion angles for the sphere and plate particles, and the shape of the debris cloud. The wax collection technique netted 80-90% recovery of the total possible weight (sphere + weight of plate material removed).

The central hole models were developed for inclusion in the FATEPEN program developed by the Naval Surface Warfare Centre, Dahlgren Laboratory. FATEPEN was originally developed for application to high velocity (up to 5 km/s) fragment penetration of thin aluminium plates by compact steel fragments (Yatteau, 1982). However, several experiments and analytical efforts extended the range to impact speeds below the fracture threshold, to additional fragment and target materials, and to a variety of fragment shapes (Yatteau *et al.*, 1991a, b). The original version of FATEPEN calculated the size of the central hole based on the accumulated area removal by individual perforating debris particles while the current version uses a central hole model based on impulsive loading and response of the plate.

The debris cloud was described by examining the debris particle numbers and sizes, the velocity distribution, and the debris particle trajectory distribution. For the debris particle numbers and sizes, it was necessary to select a subset of particle sizes from the debris cloud. Three penetrator particle sizes were used along with a single average size for the target particles. The size of the primary, or largest, fragment particle, M_{f1}, and the total number of secondary particles were determined by empirical functions of the encounter conditions at the shatter plate. The representative numbers and sizes of larger and smaller secondary fragment particles, N_{f2}, M_{f2}, N_{f3} and M_{f3}, respectively, were then computed from the total number of particles using experimentally determined size distribution functions for steel cubes. The larger particles represented the mean size and total mass of all particles above the mean particle size of the entire population, and the smaller particles represented the mean size and total mass of all particles below the population mean. The number, N_t, and average size, M_t, of the target particles were determined from the total mass of plate material driven out the rear of the plate and an empirically determined function of the encounter conditions for the number of plate particles.

The debris particle velocity distribution was based on observations of debris cloud radiographs for steel fragments impacting steel plates at speeds up to 3000 m/s. The debris particles were presumed to reside on the surface of an expanding, hollow, ellipsoid of revolution with a major-to-minor axis ratio of 1.5 (Rolens *et al.*, 1976). The distribution of particle velocities were closely approximated by the following function:

$$V_x(\varphi) = V_1 \cos(q\varphi)$$

where $V_x(\varphi)$ is the component of the particle velocity parallel to the shotline, φ is the trajectory inclination angle relative to the shotline, V_1 is the debris cloud leading edge velocity and q is a constant depending on the shape of the ellipsoid. A value of $q = 1.92$ is used for the 1.5 ratio ellipsoid for trajectory inclination angles up to 25°.

The number of debris particle trajectory intersections on planes normal to the debris cloud axis within a radius *r* of the debris cloud axis increased nearly linearly with increasing *r* out to the edge of the pattern (Recht *et al.*, 1969), that is:

$$N(r) = \left(\frac{r}{r_m}\right) N_m$$

where *N(r)* is the number of particle trajectories impacting a plate normal to the debris cloud axis within a radius *r* about the centre of the impact pattern, r_m is the maximum pattern radius, and N_m is the total number of debris particles striking the plate. The number of debris particles, *dN*, intercepted by ring elements of width *dr* about the centre of the pattern is a constant given by:

$$dN = \left(\frac{N_m}{r_m}\right) dr$$

The plate damage models included an area removal model and an impulsive loading and response model.

The area removal model assumes that if the sums of the areas of the holes produced in a ring increment about the centre of the pattern exceeds the area of the ring, then that ring is deemed to be removed. The hole pattern diameters for two sets of particles, D_{mf} and D_{mt}, were determined by the dispersion angles and the plate spacing. The sizes of individual holes were predicted as a function of debris particle density, size, and impact velocity and plate material and thickness. Hole size was predicted to increase above the diameter of the fragment with increasing impact speed and with increasing plate thickness. Each of the ring increments contained the same number of impacts. It was shown that for ring elements impacted by all three secondary particle sizes, the central hole diameter based on area removal was:

$$D_h = 0.5\left[\frac{\left(N_{f2}D_{tf2}{}^2 + N_{f3}D_{tf3}{}^2\right)}{D_{mf}} + \frac{N_t D_{tt}{}^2}{D_{mt}}\right]$$

where D_{tf2}, D_{tf3} and D_{tt} are the individual particle hole sizes calculated using the average impact velocity for the perforating particles of each kind. The area removal model does not take into account material removal between holes and is therefore conservative with respect to fragment lethality and generally underpredicts the diameter of the central hole.

The impulsive loading and response model was an attempt to improve upon the impulse-punch model developed by Recht (Rolens *et al.*, 1976). The Recht model examined the velocity and areal density of particles impacting the plate within some radial ring increment located a distance *r* from the centre of the pattern. An equivalent cylinder of radius *r* was defined as having the same areal density as the particles impacting the ring increment in question. If the velocity of the debris particles at *r* exceeded the ballistic limit velocity for the equivalent cylinder and plate in question, then that ring increment was deemed to be removed form the plate. The model was applied to the current test conditions and found to greatly over-predict the capacity for the debris particles to enlarge the central hole.

The new model retained the Recht concept of using available ballistic limit velocity data to supply the required failure criterion for an impulsively loaded plate. The new model focused on the post-impact kinetic energy imparted to the remaining plate material by both perforating and non-perforating debris particles and compared it with the post-impact kinetic energy of the penetrator and plate plug for the equivalent cylinder impact at the ballistic limit velocity. In this way, only the impulse actually delivered to the plate by perforating particles was accounted for. The equivalent cylinder impact definition in the new model involved only steel cylinders with a slenderness ratio, $L/D = 1$.

The model was based on the idealisation that the impacting debris particles load the plate impulsively, that is, perforating and non-perforating particles instantaneously impart a velocity distribution in the plate across the impact pattern before significant plate deformation occurs. If the initial radial velocity gradient normal to the plate near the centre of the plate was too large to be accommodated by shear strain behind the radially propagating plastic shear wave, a shear failure would occur early, and the material at the centre of the impact pattern would be punched from the plate. If the initial post-impact velocity gradient was not too large, the plate would initially deform in shear, but failure could still occur later under combined shear, membrane, and bending stresses. No attempt was made to analytically model these plate responses and failure mechanisms. Instead, a comparison of the post-impact kinetic energy distribution in the perforated and cratered plate impacted by the debris cloud was made to the post-impact kinetic energy for equivalent plate impacted by a steel cylinder.

In FATEPEN, the comparison between the actual and equivalent impact was accomplished incrementally by examining the impact and response of differential ring elements of increasing radius. The plate for the equivalent cylinder impact was defined as having the areal density of the current ring element less any material removed by the perforating particles. The free impact residual kinetic energy for the equivalent plate impacted by the steel cylinder at the appropriate ballistic limit velocity then determined maximum kinetic energy that could be converted to plastic work without failure. The calculations were as follows:

The radius, area and initial mass of the current ring element of width dr were:

$$r = r + dr$$

$$dA = \pi[r^2 - (r - dr)^2]$$

$$dM_t = \rho_t \, dA \, T$$

where ρ_t is the density of the plate material and T is the plate thickness.

The trajectory inclination angle and particle impact velocity for the current rings were:

$$\varphi = \frac{1}{\tan\left[\left(\frac{r - D_s}{2}\right) \Big/ S\right]}$$

$$V_{oi} = V_1 \cos(q\varphi)$$

where D_s is the fragment hole diameter in the shatter plate and S is the spacing between this plate and the shatter plate.

The number of the *i*th type particles ($i = f_1, f_2$ or t) impacting the current ring element was:

$$dN_i = \left(\frac{N_i}{r_m}\right) dr$$

An individual particle slug mass was:

$$M_{pi} = \frac{\pi D_i^2 \rho_i T}{4}$$

The impulse delivered by all of the *i*th particles to the ring was:

$$dI_i = \left[M_{oi} V_{oi} - \left(M_{Ri} + M_{pi}\right) V_{Ri}\right] dN_i$$

where V_{Ri} is the residual velocity of residual particle and plate plug combined mass centre.

The mass deposited in the ring element by all the *i*th particles and the total mass removed by the perforating *i*th particles was:

$$dMD_i = (M_{oi} - M_{Ri})\, dN_i$$

$$dML_i = M_{pi}\, dN_i$$

The residual mass of plate material within the current radius *r* was:

$$dM_{tR} = dMR_t + dM_t - \sum_i dML_i$$

where dMR_t is the plate mass of any interior ring elements not yet removed (calculated below). If dM_{tR} was less than zero, the ring was deemed removed by overlapping perforations as in the area removal model.

The total residual mass of plate material and penetrator material in the current ring was:

$$dM_{tR} = dMR_t + dM_t - \sum_i \left(dMD_i - dML_i\right)$$

where *dMR* is the retained total residual mass not yet removed at lesser radii.

The total impulse delivered to the current and any retained interior rings from all particles was:

$$dI = dIR + \sum_i dI_i$$

where *dIR* is the impulse delivered to retained interior rings.

The average residual velocity of the perforated plate and deposited debris particle mass remaining within *r* was:

$$VR = \frac{dI}{dM_R}$$

The post-impact kinetic energy in the plate impacted by the uniform debris cloud was to be compared with the equivalent cylinder impact was:

$$KE_R = \frac{\left(0.5\, dMR\, V_R^{\,2}\right) r^2}{A_r}$$

where A_r is the total area of the remaining ring elements within the r:

$$A_r = AR_n + dA$$

where AR_n is the retained area of unremoved ring elements at lesser radii.

Only the remaining plate material underwent plastic work during the plate response. The uniform plate thickness that represented the same energy absorbing capacity per unit area as the perforated ring element was:

$$T_e = \frac{dM_{tR}}{A_r\, \rho_t}$$

A rigid steel cylinder that impacted the equivalent plate at the ballistic limit velocity first exchanged momentum with the plate plug in the path of the cylinder. The initial momentum exchange was assumed to occur as a free impact without influence of the surrounding plate material. The free impact decelerated the cylinder and accelerated the plate plug to an initial post-impact velocity of:

$$V_{Rcl} = \frac{M_{cl}\, V_{50}}{M_{cl} + M_{tl}}$$

where M_{cl} and M_{tl} is the mass of the rigid steel cylinder and plate plug, respectively.

The mass of the steel cylinder with $L/D = 1$ was:

$$M_{cl} = 2\pi r^3 \rho_{st}$$

The plate plug mass was:

$$M_{tl} = \pi r^2 \rho_t T_e$$

The free impact residual kinetic energy for the equivalent impact was:

$$KE_{Rcl} = \frac{M_{cl}\, V_{50}^{\,2}}{2\left(1 + \dfrac{M_{tcl}}{M_{cl}}\right)}$$

The criterion for removal of the current ring element by the debris cloud was:

$KE_R > KE_{Rcl}$ and

$dMR_t = dM_R = dIR = AR_r = 0$

Otherwise, the ring element was retained and

$dMR_t = dM_{tR}$

$dMR = dM_R$

$dIR = dI$

$AR_r = A_r$

The ballistic limit expression for very efficient plugging type perforations by non-deforming steel cylinders (Ipson and Recht, 1977) provided good agreement between model predictions and the experimental test results. The ballistic limit velocity expression was:

$$V_{50} = V_{50\tau} = C\tau \frac{\left(T/D\right)^{0.75}}{\left(L/D\right)^{0.5}}$$

For an $L/D = 1$ cylinder, the equation reduced to:

$$V_{50} = V_{50\tau l} = C\tau\left(\frac{T_e}{2r}\right)^{0.75}$$

Values of C_τ for steel plates and aluminium plates were given by (Ipson and Recht, 1977):

$$C_\tau = -0.0062(BHN_t)^2 + 3.28(BHN_t) + 184 \text{ (m/s)}$$

$$C_\tau = -0.00166(BHN_t)^2 + 0.75(BHN_t) + 300 \text{ (m/s)}$$

where BHN_t is the Brinell hardness of the plate material. The values used for the model and test data for the mild steel and the 2024 aluminium plates were $BHN_t = 185$ and $BHN_t = 120$, respectively.

The impulse-response model provided improved predictions over the simple area removal model for all cases. The new model applied particularly well to thinner plates but under predicted the central hole diameters in the thicker plates at larger plate spacings.

2.4.7 Ballistic Perforation Dynamics

- Recht and Ipson, 1963

This paper developed analytical equations to define the ballistic perforation dynamics of blunt and sharp-nosed fragments impacting plates normally and obliquely.

When a cylinder perforates a relatively thin plate ($T/L < 0.5$ and $T/d < 0.5$) normally, a plate plug of diameter, D, equivalent to that of the expanded portion of the projectile, will be ejected. As the fragment perforates the plate, two major processes reduce the velocity of the fragment:

- Acceleration of the plate-plug mass is accomplished at the expense of the fragment's momentum and
- Shearing resistance at the edge of the plate-plug acts to decelerate the fragment-plug combination.

An analytical model concerning the blunt-fragment perforation process at nominal ballistic velocities was developed. Idealising the inelastic impact between the projectile and the plate-plug as that of two free cylinders, i.e., the plug is completely free from the plate. As the impact is inelastic, the final velocity of both cylinders must be equivalent. Due to the conservation of momentum, the free impact final velocity, V_f, is:

$$V_f = \frac{M_p}{M_p + M_{sn}} V$$

where M_p and M_{sn} are the fragment and free plug masses, respectively, and V is the initial fragment velocity.

The energy lost to deformation and heat during this free impact is the difference between the initial and final kinetic energy, or

$$E_{fn} = 0.5\left(\frac{M_{sn}}{M_p + M_{sn}}\right)M_p V^2$$

Additional kinetic energy will be lost during the perforation of the plate due to the presence of the peripheral shear zone at the plug boundary. This additional loss is represented by W_n. The energy balance is then given by:

$$0.5 M_p V^2 = E_{fn} + W_n + 0.5 M_p V_r^2 + 0.5 M_{sn} V_r^2$$

where V_r is the residual velocity of the projectile and plate-plug.

At the minimum perforation velocity, V_{xn} (ballistic limit velocity), the residual velocity, V_r, is zero. Substitution of E_{fn} at $V = V_{xn}$, and $V_r = 0$ into the above energy balance yields the work required to overcome the resistance due to the presence of the shear zone:

$$W_{sn} = 0.5\left(\frac{M_p}{M_p + M_{sn}}\right)M_p V_{xn}^2$$

If the previous equations are substituted for W_n and E_{fn} in the energy balance equation, the residual velocity is then:

$$V_r = \frac{M_p}{M_p + M_{sn}}\sqrt{V^2 - V_{xn}^2}$$

For very high initial velocities, the impulse transferred to the plate external to the plate plug will be very small compared to the total momentum. The residual velocity expression breaks down as the ratio of *V/C* becomes large (where C is the speed of sound in the material). This break down is associated with projectile deformation, as impact pressures become very high, i.e., about 4,000,000 psi at 4000 fps.

Rewriting the previous equation in terms of geometrical dimensions yields:

$$V_r = \frac{1}{1 + \Omega\left(\frac{D}{d}\right)^2 \frac{T}{L}}\sqrt{V^2 - V_{xn}^2}$$

where Ω is the ratio of plate to projectile material density, *D/d* is the ratio of plug diameter to projectile diameter, and *T/L* is the ratio of plate thickness to the projectile length. In the usual case, the effect of *D/d* is quite small and since *D* is not usually known, a value of unity can be used for this ratio.

An expression has been developed for the minimum perforation velocity at normal impact obliquity and is given by:

$$V_{xn} = \frac{4\Omega T^2 \psi \eta}{Ld}\left[1 + \sqrt{\left(\frac{L+\Omega T}{\Omega T}\left(1 + \frac{d}{4\rho_s T \eta \psi^2}\right)\right)}\right]$$

where $\psi \quad = \dfrac{\rho_P C_P + \rho_s C_s}{\rho_P C_P \rho_s C_s}$

ρ_p, ρ_s = projectile and plate material densities

C_p, C_s = longitudinal acoustic-wave velocities in projectile and plate

η = function related to dynamic shear strength of plate material, assumed to be constant and has dimensions of stress

If the fragment strikes the plate obliquely (at an angle of obliquity θ) and the total angular change in direction of the fragment as it passes through the plate β, then the post-perforation obliquity is $\theta - \beta$. The entire component of the initial total momentum M_pV, which is perpendicular to the emergent path, will be transferred to the plate and only the momentum in the direction defined by β will be involved in the perforation. When $V = V_x$ (the minimum impact velocity for plate perforation), the fragment will change its direction by a characteristic angle β_x. As V increases, β decreases; thus, only at $V = V_x$ does the change in direction equal β_x. The minimum perforation velocity is the component of V_{xn} in the direction defined by β and is therefore $V_x\cos\beta$. By replacing V with $V\cos\beta$, V_{xn} with $V_x\cos\beta$, and M_{sn} with $M_{sn}/\cos\theta$, the equation for oblique perforation is:

$$V_r = \frac{\cos\beta\,\sqrt{V^2 - V_x^2}}{1 + \dfrac{M_s}{M_p}} = \frac{\cos\beta}{1 + \Omega\left(\dfrac{D}{d}\right)^2 \dfrac{T}{L\cos\theta}}\sqrt{V^2 - V_x^2}$$

The expression for the prediction of β is given by:

$$\sin\beta\cos\beta = \frac{\sin\beta_x \cos\beta_x}{\dfrac{V^2}{V_x^2} + \dfrac{V}{V_x}\sqrt{\dfrac{V^2}{V_x^2} - 1}}$$

V_x and β_x must be determined experimentally.

For thick plates perforated normally ($\theta = 0^\circ$) by a steel cylinder, a more general form of equation (41) is required. If, for normal perforation by cylinders, then

$$\frac{M_{sn}}{M_p} = \Omega\left(\frac{\mathrm{D}}{\mathrm{d}}\right)^2\left(\frac{T}{L}\right)$$

and equation (42) can be written as

$$V_r = \sqrt{\frac{V^2 - V_{xn}^2}{\left[1 + \dfrac{M_{snr}}{M_p}\right]\left[1 + \Omega\left(\dfrac{D}{d}\right)^2 \dfrac{T}{L}\right]}}$$

where M_{snr} is the ejected plug mass.

Thick aluminium plates (*T/L* = 1.45) were used to verify the equation above experimentally at normal obliquity and the results demonstrated that this equation represented the experimental data rather well.

For plates perforated by penetrating projectiles, the projectile does not undergo the severe impact with the mass of the plate that represents the important portion of the first perforation step for the blunt fragment. It does not produce a shear plug. Instead, the projectile perforates a relatively thin plate by displacing and compressing material laterally. The energy balance is:

$$0.5M_pV^2 = 0.5M_pV_r^2 + W$$

where W is the work done during the perforation.

The post-perforation velocity of penetrating projectiles at any impact obliquity is:

$$V_r = \sqrt{V^2 - V_{\tau}^2}$$

The analytical equations developed herein serve to predict the residual velocity and angular change in direction of blunt fragments that perforate plates and consider obliquity, thickness and projectile dimensions up to a high velocity impact of 4000 fps.

2.4.8 Response of Simulated Propellant and Explosives to Projectile Impact – III Experimental and Numerical Results of Warhead Penetration and Fragmentation

- Yuan and Goldsmith, 1992

This paper presents experimental and numerical results of micro fracture and fragmentation of propellant and explosive simulant (Propergol) samples resulting from projectile impact. A micro fracture and fragmentation oriented code had been developed upon modification and combination of a fragmentation subroutine BFRACT and a two-dimensional finite difference program AUTODYN. The experimentally determined responses of a layered target and a model warhead to high velocity impact by armour-piercing projectiles are also presented. Simulation results of combined fragmentation/penetration processes were compared with experimental measurements.

The experiments were performed on model warheads consisting of a steel cylinder filled with simulated explosive and two steel covers. All steel components were 20 mm thick and had a hardness of Rc40 - 44. The 45 g armour-piercing projectiles had a hard steel core wrapped by a copper jacket (core mass was 25.3 g). The length and maximum diameter of the bullet core were 47 and 10.8 mm, respectively. Seven shots were fired at the model warheads with initial velocities of 851, 892 and 924 m/s. The replicated explosive consisted of a 90 mm thick disk with a diameter of 125 mm constrained laterally by a steel cylinder to which the end plates were screwed at the top and bottom.

Numerical simulations of the penetration of the model warhead by armour-piercing projectiles were performed using an explicit finite element program, DYNA2D.

A fine mesh was used in the central region since penetration occurs along the axis of symmetry, thereby making this region the point of interest. A total of 786 elements were used to model the problem. Only the hard steel core of the projectile was modelled since the copper jacket is torn away at impact. The axi-symmetric arrangement of the grid was subjected to radial and axial zero velocity boundary conditions at the external circumference of the steel covers, a radial zero velocity at the external circumference, and a stonewall-type of boundary along the axis of symmetry to prevent the material from moving across any plane perpendicular to the end plate that contains the axis.

An elastic-plastic-hydrodynamic material model was used to represent the constitutive behaviour of the simulated explosive. The yield strength is expressed as a function of the effective plastic strain by:

$$\sigma_y = \sigma_0 + E_h \bar{\varepsilon}^p + \left(a_1 + a_2^p\right)\mathrm{Max}(0, P)$$

where P is the hydrostatic pressure, E_h is the plastic hardening modulus defined in terms of Young's modulus E and tangent modulus E_t as follows:

$$E_h = \frac{E_t E}{E - E_t}$$

Terms σ_o, a_1 and a_2 are constants; Max(0,P) is the largest-value function that takes the algebraically greatest value among 0 and P. The effective plastic strain is given by:

$$\bar{\varepsilon}^p = \int_0^t \sqrt{\frac{2}{3} D_{ij}^p D_{ij}^p}\, \mathrm{d}t$$

where t is time and D_{ij}^p is the plastic component of the rate of deformation tensor.

The hydrostatic pressure is given by:

$$P = c_0 + c_1\mu + c_2\mu^2 + c_3\mu^3 + (c_4 + c_5\mu + c_6\mu^2)\tilde{E}$$

Quantities $c_0 - c_6$ are constants; $\tilde{E}$ is the internal energy; $\mu = \rho/\rho_0 - 1 = \eta - 1$ is the compressibility, and ρ/ρ_0 is the ratio of current density to initial density.

A temperature-dependent elastic-plastic-hydrodynamic material model and a Gruneisen equation of state have been used to describe the constitutive relation for the steel covers at high strain rates. The strength model, proposed by Steinberg *et al.* (1980), defines the dependence of the shear modulus and the yield strength on pressure, temperature and effective plastic strain in the form

$$G = G_0\left[1 + \left(\frac{G'_p}{G_0}\right)\left(\frac{P}{\eta^{1/3}}\right) + \left(\frac{G'_T}{G_0}\right)(T - 300)\right]$$

$$\sigma_y = \sigma'_0\left[1 + \left(\frac{\sigma'_p}{\sigma_0}\right)\left(\frac{P}{\eta^{1/3}}\right) + \left(\frac{G'_T}{G_0}\right)(T - 300)\right]$$

subject to the limitation that

$$\sigma_0' = \sigma_0 \left[1 + \beta \left(\varepsilon_0 + \bar{\varepsilon}^p \right) \right]^n \leq \sigma_{max}$$

The terms G_0 and σ_0 are the initial shear modulus and initial yield strength of the steel, respectively; G'_p and σ'_p are the derivatives of G and σ with respect to pressure P; and G'_T is the derivative with respect to temperature, T. Quantities G'_T, G'_p and σ'_p are considered to be constants for given materials subjected to high strain rates; β and n are work-hardening parameters; η is the compression parameter. Finally, ε_0 and $\bar{\varepsilon}^p$ are the initial plastic strain and effective plastic strain, respectively.

The Grunëisen equation of state, which was determined form a cubic relation between shock velocity U_s and particle velocity U_p defines the pressure for compressed materials as:

$$P = \frac{\rho_0 c^2 \mu \left[1 - (1 - 0.5\gamma_0) - 0.5a\mu^2 \right]}{\left[1 - (s_1 - 1)\mu - s_2 \frac{\mu^2}{\mu + 1} - s_3 \frac{\mu^3}{(\mu + 1)^2} \right]^2} + (\gamma_0 + a\mu)\bar{E}$$

where c is the intercept and s_1, s_2 and s_3 are the coefficients of the slope of the $U_s - U_p$ curve, γ_0 is the Grunëisen parameter; and a is the first-order volume correction to γ_0.

An elastic-plastic model was used for the projectile core. Penetration with an initial velocity of 890 m/s was numerically studied for the above material models. The values for the material model constants are listed in Tables 2.3 and 2.4.

Table 2.3: Material Parameters for Propergol used in Penetration Computations

Parameter	Value	Parameter	Value
Density, ρ (g/cm^3)	1.82	c_1	5.666
Yield Strength, σ_0 (MPa)	50	c_2	39.13
Shear Modulus, G (GPa)	0.487	c_3	187.7
Young's Modulus, E (GPa)	1.419	c_0, c_4, c_5, c_6	0
Tangent Modulus, E_t (GPa)	0.20		

Table 2.4: Steel Cover and Projectile Material Parameters in Penetration Computations

Parameter	Value	Parameter	Value
Density (g/cm^3)	7.85	G'_p/G_0, σ'_p/G_0 (x 1000 GPa)$^{-1}$	26
Shear Modulus, G (GPa)	77	G_t/G_0, kK^{-1}	0.45
Poisson's Ratio, v	0.3	Volume Correction Factor, a	1.72
Young's Modulus, E (GPa)	2.09	Melting Temperature, T_{m0} (K)	2380
Projectile Yield Strength, Y_0 (GPa)	2.5	Grunëisen Parameter, γ_0	1.93
Cover Yield Strength, σ_{max} (GPa)	1.5	Work-Hardening Parameter, β	43
Initial Cover Yield Strength, σ_0 (GPa)	0.34	Work-Hardening Parameter, β'	1.0
Initial Plastic Strain, ε_0	0	Work-Hardening Parameter, n	0.35

2.4.9 The Influence of Plate Hardness on the Ballistic Penetration of Thick Steel Plates

- Dikshit *et al.*, 1995

Most literature in the area of ballistic penetration of metallic plates at ordnance velocities has been for thin plates ($T/D < 1$). The effect of plate hardness on ballistic performance of steels is also limited and even these pertain to thin plates. The influence of plate thickness (20, 40 and 80 mm) on ballistic performance with a large calibre projectile (20 mm diameter) was investigated by Dikshit and Sundararajan, 1992. It was observed that the penetration under plane strain and plane stress conditions had entirely different characteristics. The transition from plane strain to plane stress condition occurs when the plastic zone ahead of the penetrating projectile just impinges on the backface of the plate. Therefore, all of the penetration of thin plates ($T/D \ll 1$) occurs under plane stress conditions, while for thick plates ($T/D \gg 1$) it is all under plane strain.

The objective of the study was to characterise the penetration of steel plates of varying hardness in the range of HV295 – HV520 and of thickness 20 and 80 mm by ogive-shaped 20-mm-diameter projectiles over the velocity range 300 - 800 m/s at normal impact angles. The experimental results include the variation of penetration depth, crater volume, lip height, bulge height and diameter, plugged length and diameter and specific energy absorption capacity with impact velocity for tests on each plate of a given hardness and thickness.

The target plate material consisted of rolled homogeneous armour (RHA) steel plating that measured approximately 450 x 450 mm. The steel plates, of low alloy steel composition, were used in the as-received (AR) as well as in the quenched and tempered (QT) conditions. The 20 and 80 mm plates had hardnesses of HV300, 350, 440 and 520 and HV295, 440 and 520, respectively. Some plates of HV470 were also tested to examine the impact crater formed. Tensile coupons were taken from the plates of different hardness levels and demonstrated that the 0.2% offset yield strength (σ_{ys}) and the ultimate tensile strength (σ_{UTS}) increases and the uniform strain (ε_u) and the fracture strain (ε_f) decreases, respectively with increasing hardness.

The projectile was a steel cylinder with an ogive nose, of diameter 20 mm and a mass of 110 g. The hardness was approximately HV600.

The target plates were clamped firmly to the target holder at a distance of approximately 30 m from the gun. Six to eight shots were impacted on each plate. The impact velocity was varied by varying the charge mass of the propellant. The centre-to-centre distance between two impact craters was at least four times the diameter of the projectile, while the distance from the impact centre to the edge of the plate was at least twice the projectile diameter.

After the ballistic tests, each impact crater was examined in great detail. The depth of penetration (X_p), entry hole diameter (D_e), the crater volume (U), the lip height (H), the bulge height (H_b), the bulge diameter (D_b), and plug diameter (D_p) were all measured on the impact crater. After making the measurements, selected impact craters were sectioned along their diameter then ground and polished with emery paper up to 600 grit. Both microhardness (200 g load, Vickers indenter) and macrohardness (30 kg load, Vickers indenter) measurements were made on the sectioned surface. A series of hardness measurements at regular intervals were performed on the sectioned surface along the lines Y_1, Y_2, Y_3 and X_1 as shown in Figure 2.5. With the above measurements, the hardness-distance profiles were determined.

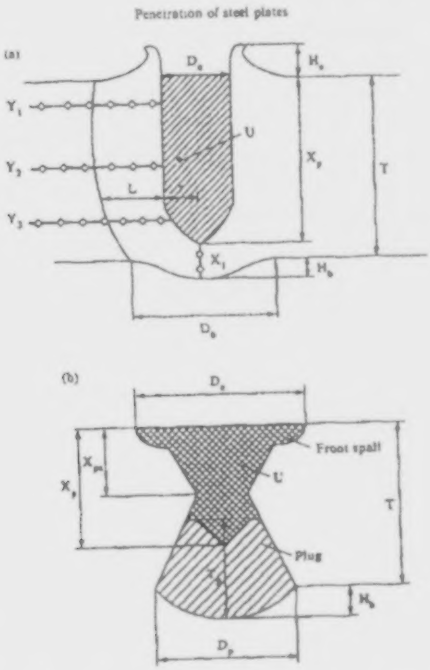

Figure 2.5: Sectioned View of the Impact Craters Formed on (a) Low Hardness and (b) High Hardness Plates

The impacted steel plates of 20 mm thickness and hardness HV300, 350, 440 and 520 were examined for assessing the nature and mode of plate material deformation. The HV300 plate experienced substantial lip formation all around the periphery of the impact crater on the energy side, while the HV400 and 520 plates did not have any lip. On the exit side, the HV300 had the formation of a bulge and subsequent perforation by star crack formation, while the HV440 and 520 plates experienced complete perforation by plugging.

The impact crater sections for the HV520 plate at impact velocities of 394 and 434 m/s demonstrated dramatically different appearances, despite only a 40 m/s difference. At $V = 394$ m/s, the crater had a smooth appearance and backside bulging with adiabatic shear bands (ASB) forming around the crater. At $V = 434$ m/s, the backside had completely bulged because of through thickness crack propagation along the ASBs.

The impact crater sections for the HV470 and HV440 plates at impact velocities of 502 m/s and 537 m/s, respectively, both demonstrated that both the craters were characterised by circumferential spall on the entry side and by extensive cracking (along ASBs) on the exit side.

The impact crater sections for the HV390 and HV350 plates at impact velocities of 580 m/s both had extensive bulging in the backside of the plates. The HV350 plate had lips along the periphery of the entry side hole and the HV390 had its lips removed by spalling.

From the above observations, an approximate minimum velocity required for plugging failure as a function of plate hardness can be determined. Figure 2.6 illustrates the velocity-hardness experimental data points. The velocity-hardness combinations, which resulted in plugging, are indicated as filled circles. The boundary line between plugging and non-plugging is indicated in the Figure as curve AB. From the Figure, the minimum velocity for plugging increases with decreasing hardness of the plate.

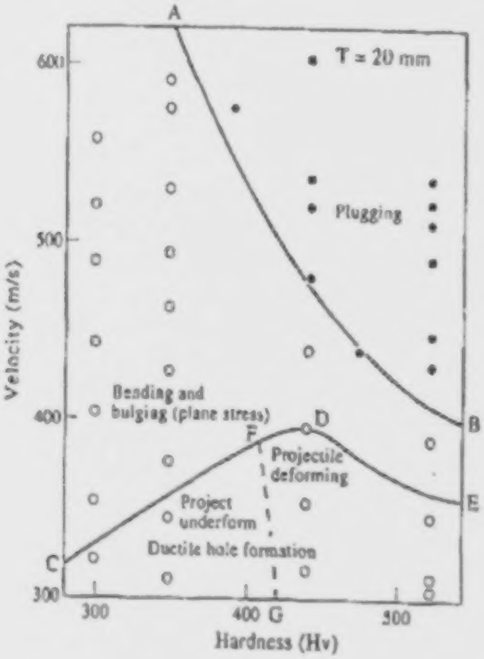

Figure 2.6: Velocity-Hardness Curve for Experimental Data

Plugging occurs by the initiation and propagation of an ASB into the target material ahead of the crater bottom followed by crack propagation along the just-formed ASB. This was verified by a detailed examination of the HV520 crater formed at an impact of 394 m/s.

The depth of penetration (X_p) increases with increasing impact velocity at all hardness levels. For a given impact velocity lower than about 500 m/s, the depth of X_p decreases with increasing hardness up to HV440. The volume of the craters (U) also decreases with increasing hardness up to HV440. The effect of increasing the impact velocity is to increase U irrespective of the hardness of the steel plate.

The bulge formed on the backside of the plate as a result of the plastic zone ahead of the penetrating projectile impinging on the rear face of the plate occurred at velocities as low as 350 m/s. The HV300 and 350 plates experienced extensive bulging and a maximum bulge height (H_b) of 10 mm before perforation occurred through the formation of star cracks. The H_b of the HV440 and 520 were lower than the HV300 and 350 plates. The bulge diameter (D_b) increases with increasing impact velocities and does not show any substantial effect due to the plate hardness.

Using the hardness profiles from the sectioned surfaces, it was observed that the normalised hardness value increased with decreasing distance from the crater wall at both the impact velocities of 377 and 468 m/s for HV300. For the HV440 and 520 plates, the normalised hardness values increased with decreasing distance from the crater wall only up to a distance of about 2 mm before which the normalised hardness decreased substantially as the crater wall was approached. The hardness attains the base value at a distance of about 6.0 – 6.5 mm, 10 mm and 6 mm for the HV350, 440 and 520, respectively. HV300 steel has the ability to work harden to a significant degree and therefore, the steep hardness gradient was actually the reflection of a strong plastic strain gradient within the plastic zone. The heat generated in the target steel plate during plastic flow around the penetrating projectile and the resulting temperature rise can reduce the hardness of the plate if the temperature exceeds the tempering temperature of the plate. Therefore, for the HV440 and 520 steels, the increase in hardness due to work hardening is more than off-set by the temperature-induced softening at distances very close to the crater wall, resulting in the observed soft zone.

The cumulative specific energy (E_{sc}) absorbed by the plate during penetration is

$$E_{sc} = \frac{mv^2}{2U}$$

where U is the volume of the crater formed in the target plate when it is impacted by a projectile of mass m at a velocity V. The equation above is only applicable at velocities below the ballistic limit since it assumes zero residual velocity and E_{sc} represents the average resistance offered by the plate to penetration. The value of U can be obtained either experimentally (U_{exp}) or by calculation (U_{cal}), where U_{exp} is determined by filling the crater up to the original plate level with plasticine of known density and U_{cal} is determined from the depth of penetration (X_p) and the known variation in the projectile volume as a function of distance along its cylindrical axis from its nose tip. In the determination of U_{cal}, it is assumed that the projectile does not suffer any deformation, whereas, for the determination of U_{exp}, it includes the volume created by the projectile plus the extra volume created by font end spalling, by the rigid movement of the plug ahead of the projectile and by the ASB-induced micro-fracture along crater walls. In either case, the E_{sc} values remain fairly independent of velocity. However, at higher velocities, both E_{sc} values start decreasing with increasing velocity. As such, E_{sc} (the resistance to penetration) is not a constant all through the penetration process.

A plot of E_{sc} versus hardness clearly illustrates a maximum at intermediate hardness values at all impact velocities. Therefore, the energy required for perforation is lower for very high hardness plates as compared to the plates with intermediate hardness. It was also noted that in the cases of HV300 and 350 plates, that $E_{sc,exp} \cong E_{sc,cal}$ at all impact velocities up to 500 m/s. This indicates that neither projectile deformation nor plate spalling/plugging occurred. However, for HV440 and 520 plates $E_{sc,cal} > E_{sc,exp}$ and the further diverge with increasing hardness.

Similarly, the 80 mm thick steel plates of hardness HV295, 440 and 520 were examined for assessing the mode of deformation of the plate material. None of the plates were penetrated and, as such, only the entry side of the plates were examined. The impact crater section of the HV440 and 520 at $V = 789$ m/s and 763 m/s, respectively illustrated that the depth of penetration (X_p) was only about ¼ the thickness of the plate for HV440 and even less for the HV520 plate. Therefore, it can be assumed that the 80 mm plate is semi-infinite as far as the penetration process is concerned. Substantial projectile deformation and flattening occurred during the penetration.

The experimentally measured depth of penetration (X_p) and crater volume (U) demonstrated that X_p increases monotonically with velocity (V) for the HV295 plate, saturates towards a constant value at higher velocities for the HV440 plate, and increases marginally with increasing V at low velocities but then decreases with V at higher velocities. The value of U increases with increasing V in the HV295 and 440 plates while remaining constant at higher velocities for the HV520 plate. At a given V, both X_p and U decrease with increasing plate hardness.

The experimental hardness-distance profiles taken from around the impact craters from the HV295, 440 and 520 at velocities of 715 m/s, 789 m/s and 762 m/s, respectively illustrated that as the crater wall is approached, the normalised hardness value initially increases from its base value of 1.0. However, for the HV440 and 520 plates, very close to the crater wall, the normalised hardness value decreases as the crater wall is approached, leading to a peak value of the normalised hardness at some intermediate distance from the crater wall. The HV295 plate had the hardness value continuously increase as the crater wall was approached.

The cumulative specific energy (E_{sc}) absorbed by the plate increased with increasing impact velocity. $E_{sc,cal}$ increases with increasing hardness of the plate (at a given impact velocity) and $E_{sc,exp}$ is the lowest for the HV440 and not the HV295 steel.

The experimental penetration behaviour of the low-hardness plates (20 mm HV300 and HV350 and 80 mm HV295) demonstrated negligible projectile deformation and neither plugging nor front end spalling during penetration. As such, a model, which assumes the projectile to be rigid and non-deforming while it penetrates the steel, should be applicable. In contrast, a similar model will not be applicable for the high-hardness plates (HV440 and HV520) since the projectile did and will undergo deformation. Also, high-hardness plates are prone to the formation of ASBs which allow for the propagation of cracks along these bands resulting in plugging of the plate material ahead of the projectile, spalling of the plate material around the crater periphery on the entry side and micro-spalling along the crater bottom and side walls. As mentioned, the proposed model does not take into account ABS-induced plugging and spalling.

In the case of the 20 mm plate of hardness HV440 and HV520, the ratio of $E_{sc,cal}/E_{sc,exp}$ initially increases with velocity (region I), reaches a maximum and then decreases to a minimum (region II) and finally increases with increasing velocity again (region III). Region I demonstrates ductile hole formation under constrained, plane strain deformation. Once the plastic zone in the plate material ahead of the projectile impinges on the backface of the plate, the bulging process involving deformation under unconstrained, plane stress conditions is initiated for region II. After a certain amount of bulging has occurred, ASB-induced shear plugging initiates leading to the rigid movement of the plate plug ahead of and along with the projectile for region III.

In the 80 mm plate, even at the highest velocity, the depth of penetration in both HV440 and HV520 plates is such that the plastic zone is well defined, i.e., region I.

The effect of plate hardness depends very much on the stress state accompanying the penetration. Under plane strain conditions, the harder the material, the greater is the resistance to deformation. Under plane stress conditions, the effect of hardness is dramatically different. At higher hardnesses, ASB-induced shear plugging limits the penetration resistance while at very low hardnesses, the energy dissipated in the plastic zone is very low leading to low resistance again. As a result, the maximum resistance to penetration occurs at an intermediate hardness.

2.4.10 Numerical and Experimental Studies of High-Velocity Impact Fragmentation

- Kipp et al., 1993

The paper reports on the development of numerical and experimental techniques for characterising the debris spray produced in penetration events. The objective of the study was to investigate the dynamic fragmentation characteristics of high-strength steel spheres with a diameter of 6.35 mm when fired at a velocity of 3 to 5 km/s at polymethyl-methacrylate (PMMA) plates with thicknesses of 0.6 to 11 mm and density of 186 kg/m^3. The steel spheres had a mass of 1.027 ± 0.001 grams with a Rockwell-C hardness of 60 to 67. The density, yield strength, fracture toughness, Young's modulus and Poisson's ratio were 7837 kg/m^3, 2.03 GPa, 30 to 40 MPa $m^{1/2}$, 200 GPa and 0.29, respectively. The PMMA plates were used since the x-ray beam can readily discriminate between projectile and target fragments. A 6061-T6 aluminium target plate 152.4 mm on a side and either 6.35 mm or 12.7 mm in thickness was placed approximately 400 mm behind the PMMA target plate to be used as a witness plate. A total of 24 experiments were performed. The numerical tool chosen for development of fragmentation prediction capability is the three-dimensional Eulerian waver propagation code, CTH (McGlaun *et al.* 1990).

Table 2.5 gives the impact parameters and summary of results for the 24 experiments where *h* is the PMMA plate thickness, V_i is the impact velocity, ΔV is the difference between the incident sphere velocity and the debris cloud velocity, and V_e is the radial expansion velocity of the debris cloud periphery.

The images taken during the experiments qualitatively illustrate the nature of the fragmentation process. The steel fragments remain well grouped and continue to move along the original trajectory at with slightly slower velocities due to the impulse delivered by the plate. Axial dispersion of the debris is quite limited, with fairly well defined, nearly planar boundaries forming. Radial dispersion is significant, but still the fragments are contained by rather well defined limits.

Table 2.5: Impact Parameters and Results Summary

Test #	h (mm)	V_i (m/s)	ΔV (m/s)	V_e (m/s)	Test #	h (mm)	V_i (m/s)	ΔV (m/s)	V_e (m/s)
1	3.28	4460	a	a	13	5.37	4430	460	290
2	3.28	4460	a	a	14	5.36	4060	330	183
3	1.74	4450	b	200	15	5.38	3310	240	50
4	1.74	4700	150	147	16	5.37	4080	330	164
5	3.38	4570	270	271	17	3.25	4520	195	223
6	3.28	3460	200	52	18	4.71	4430	345	219
7	3.44	4160	250	171	19	5.39	4610	410	660[d]
8	1.49	3950	130	105	20	4.75	4040	295	158
9	1.51	3460	170	44	21	4.78	3750	270	82
10	0.63	3410	50	0	22	0.99	4700	85	72
11	0.64	3920	60	0	23	11.23	4060	785[c]	580[d]
12	0.69	4470	90	0	24	9.47	4030	680[c]	540[d]

[a] Oblique angle radiograph – parameters not defined

[b] Not determined

[c] Velocity of debris cloud front

[d] Diffused

The impulse imparted to the steel sphere by the PMMA plate partitions the initial kinetic energy of the steel sphere into kinetic energies of axial translation and radial expansion of the steel fragments, kinetic energy of the PMMA debris, and energy expended in the various dissipative processes active during the impact process. Several distinct regions of behaviour were noted to occur within the parameter range of the study. First, impulses for which there was no radial expansion of the steel spheres were observed in three experiments performed on target plates approximately 0.6 mm in thickness. The steel spheres remained intact at impact velocities of 3400 and 3900 m/s. A small fragment was spalled off the rear surface of the sphere at a velocity of 4500 m/s. Plots of impact velocity versus target thickness, the product of which provides an approximate measure of impulse, were used to identify three regions of behaviour in the fragmentation process: Region I – no fragmentation; Region II – cluster fragmentation: and Region III – diffuse fragmentation. The expansion velocity versus impact velocity indicated that at similar impact velocities, the expansion velocity increases with plate thickness but becomes less sensitive at increased plate thickness and that there is a critical impact velocity below which fragmentation and subsequent expansion do not occur. This velocity limit is outside of the range of the data for the 0.6 mm plate and is probably around 4000 m/s for a 1.0 mm plate. For thicker plates (1.6 mm and above) this critical velocity (about 3000 m/s) becomes independent of plate thickness.

The wave code that was used for the calculations was the Eulerian finite-difference shock wave propagation code CTH. Files containing strain rate and temperature at the time of fracture are saved periodically during the simulation and are examined to determine the extent of the fractured regions as time progressed. When the fracture process is complete, the data are post-processed to determine fragment size distribution. Dynamic fragmentation theories predict an average local fragment size at a given strain rate and temperature and the number of fragments with this average size is determined by the local mass of the material that fractures.

The average fragment diameter S was determined for the three fragmentation regions and are:

(1) solid spall dominated by fracture toughness, for which

$$S = \left(\frac{\sqrt{24}Kc}{\rho c \dot{\varepsilon}} \right)^{2/3}$$

(2) solid spall dominated by flow stress, for which

$$S = \left(\frac{1.2Y}{\rho \dot{\varepsilon}^2} \right)^{1/2}$$

and (3) liquid spall above the melt temperature, for which

$$S = \left(\frac{48\gamma}{\rho \dot{\varepsilon}^2} \right)^{1/3}$$

where ρ is the density, $\dot{\varepsilon}$ is the strain rate, c is the speed of sound, and γ is the constant value of the surface tension. The temperature and strain-rate dependent yield strength, Y, is given by

$$Y = Y_0\left(1-\frac{T}{T_m}\right)^n\left(\frac{\dot{\varepsilon}}{\dot{\varepsilon}_0}\right)^m$$

and the temperature dependent fracture toughness, K_c, is given by

$$Kc = Kc_0\left(1-\frac{T}{T_m}\right)^{n'}$$

where Y_0 is the reference yield strength, K_{c0} is the reference fracture toughness, T is the temperature, T_m is he melt temperature, $\dot{\varepsilon}_0$ is a reference value of the strain rate (one per second), and n, m and n' are constants. In the solid region, the transition from fracture toughness to flow stress dominated spall occurs at a strain rate given by

$$\dot{\varepsilon}_t = \sqrt{\frac{0.003\rho c^4 Y^3}{K_c^4}}$$

The impact simulations represented the steel and PMMA materials as low temperature Mie-Grunëisen solids, in which the Hugoniot was described with a linear shock velocity – particle velocity relationship. Using the case of Test 5 as an example, in which the steel sphere impacts a 3.38 mm PMMA plate at a velocity of 4570 m/s, the computed sequence of penetration that occurs is a as follows. As the sphere progresses through the plate, it begins to deform with the leading surface undergoing significant flattening. The impact pressure is about 30 GPa, well above the 2 GPa yield strength of the steel. Just after 1 μs, a void is beginning to be inserted into the sphere as spall fracture commences and the PMMA material in front of the sphere has been accelerated to a higher velocity than the exit velocity of the sphere. The fracture is completed between 1.5 and 2 μs. The tensile stress is observed to reach a limit of about 4 GPa, then unload as void is added to the local cells to relieve the state of tension. As the shock pulse transits the axis of the sphere, the amplitude decays from an initial peak of about 30 GPa to less than 10 GPa. This creates a large decrease in particle velocity at the leading edge of the sphere than at the trailing edge, so that the trailing material in the sphere has a relative velocity towards the leading edge of the sphere. This accounts for the fact that the parts stay clustered in a thin disk. With the completion of the impulse delivery at about 2 us, the formation of the fragments has also ended and the debris is basically in free flight.

To examine trends of the behaviour resulting from target plate thickness, eight impact calculations were made with a fixed velocity of 4500 m/s with plate thicknesses ranging from 0.76 mm to 6.35 mm to be compared against experimental data for the loss in axial momentum and the expansion velocity of the debris cloud.

The loss in axial momentum versus thickness was plotted and the numerical data compared well with the experimental data. The expansion velocity of the outer debris edge was also plotted versus thickness and the numerical values generally fell within the range of experimental data.

2.5 Multiple Plate Penetration Model 3 – MPPM3

2.5.1 MPPM3 Review-Introduction

MPPM3 is the third version of the Multiple Plate Penetration Model software, MPPM. The software / model predicts variations in projectile velocity, mass, orientation and direction for spin-stabilised projectiles penetrating spaced target elements.

The program was prepared by Jerome D. Yatteau and Richard H. Zernow (1990) at Applied Research Associates Inc. for the Naval Surface Warfare Centre.

The objective of this review is to develop an understanding of the MPPM3 software to allow its inclusion in the DeCaM software as a ballistic penetration prediction module. This report has been prepared to describe the MPPM3 software in terms of its structure, capabilities and limitations. The report also outlines both the user supplied and resident material property data used by the MPPM3 penetration model.

The sections which follow describe the findings of this review in terms of the:

- Capabilities, Limitations and Definitions (Section 2.5.2),
- MPPM3 Modelling Data and Parameters (Section 2.5.3),
- MPPM3 Output (Section 2.5.4), and
- Software Description - Structure and Operation (Section 2.5.5).

2.5.2 Capabilities, Limitations and Definitions

The MPPM3 software / model was assembled based on a variety of research efforts to model ballistic penetration events. The model was developed to provide residual penetrator characteristics during and after penetration for spin-stabilised projectiles. The software and model operate based on a variety of semi-empirical impact momentum conservation formulations, developed using imperial units of measurement. The model includes facilities to:

- predict whether target penetration occurs or not,
- calculate residual penetrator velocity, mass, orientation and direction during and after the penetration of spaced element target systems, and
- predict the erosion, deformation or break-up of projectiles during the penetration event and provide velocity, mass, and trajectory data for the resulting fragments.

The MPPM3 software system does not contain any numerical data entry limitations. Error trapping is confined to user responses to software data entry prompts, data file names and checking alphabetic codes for model parameters such as target components and materials. The software does contain a "help" menu to aid the user in selecting appropriate codes for model parameters such as target components and materials.

2.5.2.1 Projectile Material and Geometry

The authors of the software indicate that the MPPM3 model is capable of handling a variety of projectile materials including depleted uranium, tungsten alloys, steel and other ductile metals. It should be noted that the projectile penetration, erosion and break-up calculations differentiate between projectile materials based on their geometry, specific weight, Brinell hardness and ultimate strength.

Projectile geometries accommodated by the software include any combination of cylindrical base section and a truncated cone nose section, as shown in Figure 2.7. The MPPM3 software can accommodate extreme projectile geometries including: flat-ended cylinders and projectiles with pointed conical noses. It should be noted again that MPPM3 is only applicable to spin-stabilised projectiles and fin-stabilised projectiles are not explicitly dealt with.

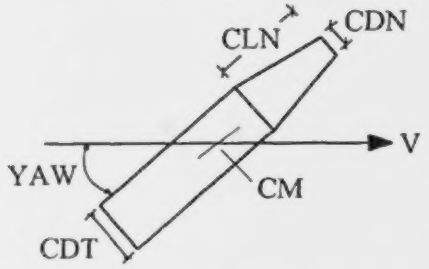

Figure 2.7: Projectile Geometry Definitions

The user may input shape factors to account for the influence of nose shape on the effective mass of target material accelerated by the projectile. The two shape factors CSF and PIF are projectile nose shape factors applied to the plate plug mass in residual velocity and residual mass calculations, respectively. It is indicated that unless experimental penetration data is available to tune the model the given default values (see Section 2.5.3) should be used. Although it has not been confirmed, it is suspected that the following equations may be used to estimate the projectile shape factors used in the software:

$$CSF = \frac{M_{cyl}}{M_p} \qquad \text{and} \qquad PIF = \frac{M_{cyl\ cone} - M_{p\ cone}}{M_{cyl}\ \text{cone}}$$

where:

M_p	Projectile mass
$M_{p\ cone}$	Mass of conical frustum portion of projectile
M_{cyl}	Mass of smallest cylinder enclosing projectile
$M_{cyl\ cone}$	Mass of smallest cylinder enclosing conical frustum potion of projectile

Shape factors for the software default projectile, a 20mm PHALANX MARK 68, are given in Section 2.5.3.0.

2.5.2.2 Target Configuration

Target systems in the MPPM3 software are defined in terms of target system components and their materials. The four target component types available in the MPPM3 software include:

- plate components (P1),
- single plate representations of volumetric components (V1),
- fluid or non-coherent material filled volumetric components (V2), and
- 18 plate volumetric component representation of avionics "black boxes" (V3 and V4).

The difference between volumetric components V3 and V4 involves the definition of average plate density ratio. All 18 of the plates within volumetric component V3 have the same average volumetric plate density, whereas, those in volumetric component V4 are randomly assigned a plate density between 80 and 140% of the average plate density value. The random plate density value is used to reflect the typical variation in component density along various shot lines. It is not stated in the user manual, but it is likely that the random numbers are uniformly distributed, since they are generated directly from the operating system random number generator based on a user supplied seed value.

The parameters used to describe the four target system component types are shown in Figure 2.8.

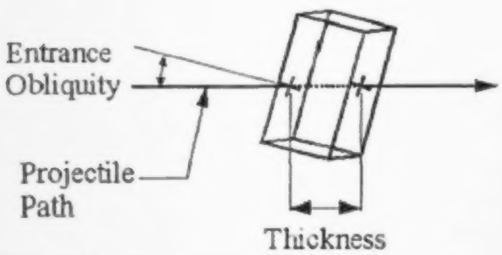

a) P1 - Plate Component Definition

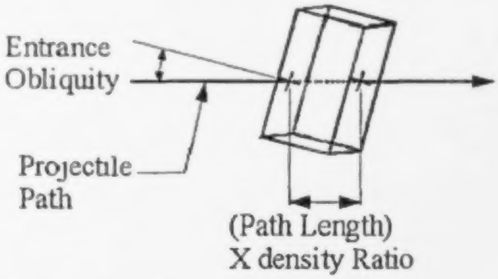

b) V1 - Plate Analogy for a Volumetric Component (Component path length is as defined for component V2)

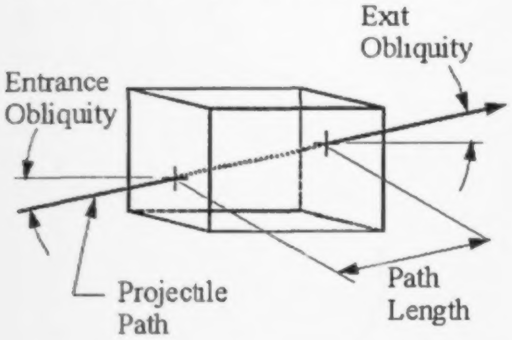

c) V2 - Fluid Filled Volumetric Component

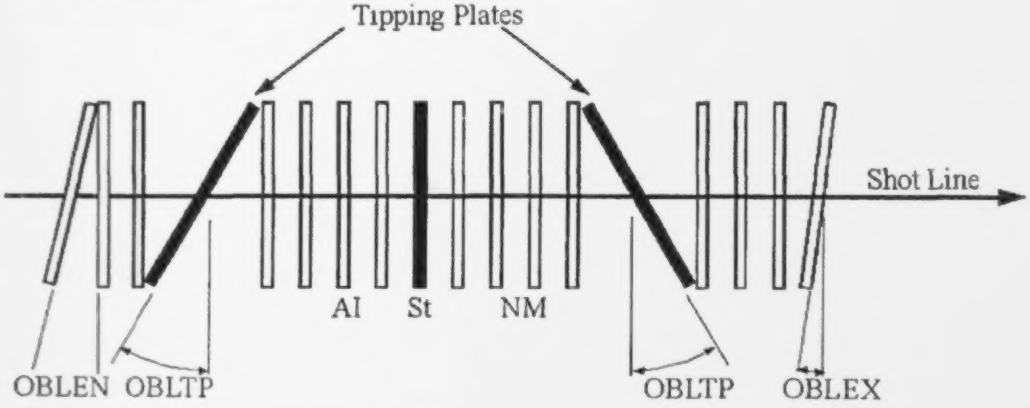

d) V3 and V4 Volumetric Component - 18 Plate Avionics Component Representation

Figure 2.8: Target Component Definition Parameters

The difference between target components V1 and V2, both of which may model a fluid or non-cohesive filled volume, is the means of calculating the penetrator residual velocity and erosion. Residual velocity for component V1 is based on a plate penetration model, whereas, the residual velocity for component V2 is calculated based on the projectile drag coefficient, fluid or material density and a standard exponential velocity decay function. It is also assumed that no projectile erosion occurs during the penetration of a target of component type V2.

The target components are made up of a variety of material types including: steel, aluminium, woven-roving laminated fibreglass panels (GRP and DORON), kevlar laminated fabric panels, laminated XP plastics, LEXAN, ceramic-faced composites and non-coherent materials (fluids). The mechanical properties of each material type are defined within the MPPM3 software, as discussed in Section 2.5.3.0.

The software includes a default target, an S2M2 plate array, comprised of 18 plates as described in Section 2.5.3.0.

2.5.2.3 Ballistic Penetration Model

The penetration events handled by the MPPM3 software are those that include spin-stabilised projectiles, target systems described by the four MPPM3 target components and the projectile/target encounter parameters described in Figure 2.9.

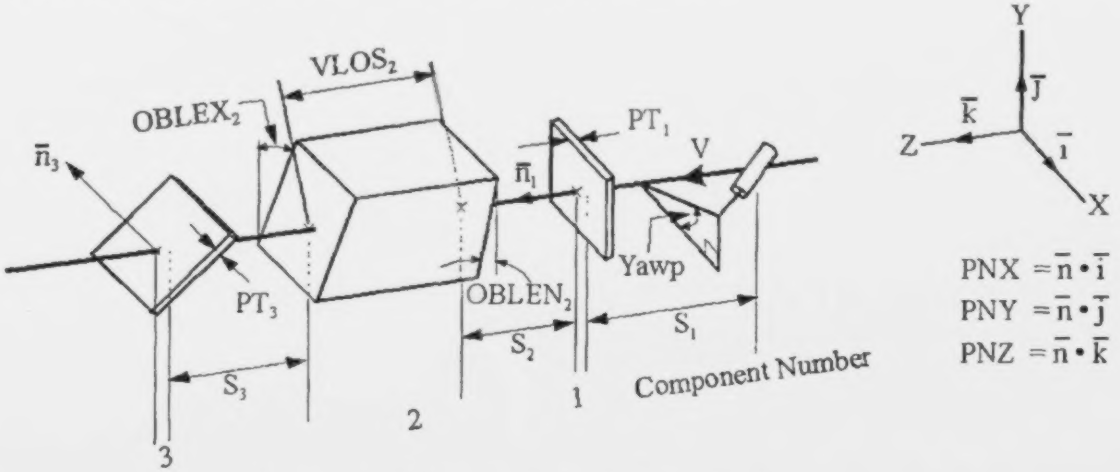

Figure 2.9: Projectile / Target Encounter Parameters

The MPPM3 software allows the user to either select the target penetration mode or allow the software to automatically determine the target penetration mode. The user may select from: 1) a thick plate model (TPPM), 2) a thin plate (plate plug) model (PLUG), or 3) use the default combined model that interpolates between the thick and thin plate model predictions depending on impact velocity and plate thickness.

When using either the thick plate or the combined model, the user has the option of having the calculation results displayed in dimensional (default) or non-dimensional formats. The non-dimensional data representation, in-general, non-dimensionalises linear measures based on the diameter of a circular area equal to the projectile's presented area, whereas, velocity based data is non-dimensionalised with the projectile impact velocity.

2.5.3 MPPM3 Modelling Data and Parameters

In this section the user supplied "data" and modelling "parameters" embedded in the MPPM3 software are described. Ideally, upper and lower limits on the values associated with both data and parameters would be defined. This is not the case in the MPPM3 software, therefore, based on a review of the published research efforts leading to the development of these models and some common sense, minimum and maximum values have been suggested for each data and parameter. In addition, the program variable and array name associated with each data value has been noted along with any default values to facilitate incorporation of this software into other programming efforts.

2.5.3.1 MPPM3 User Defined Data

The user supplied data is arranged into the three groups: 1) C - projectile data, 2) E - encounter data and 3) P - target system data. After the user supplies the C, E and P data values they are stored into the CIN(), EIN() and PIN() input data arrays, respectively. As calculations are completed these data values are transferred to the working variable names shown in Tables 2.6, 2.7and 2.8. Each of the user defined data description tables includes a default value and proposed limits (upper and lower bounds) on their numerical values. These values are proposed for use in data entry error trapping when MPPM3 is incorporated into the DeCaM software.

The projectile data describes the physical properties of the projectile of interest. The default values shown in Table 2.6 are based on a 20mm Phalanx projectile. The projectile data includes two shape factors, VR (CSF) and MR (PIF). The VR shape factor is used in the plate/plug mass residual velocity calculation, whereas, the MR ratio is used in the plate/plug mass residual mass calculation. It is suggested, in the MPPM3 documentation, that a value of 1.0 be assumed for the VR shape factor if it has not been experimentally defined. The documentation also suggests that a value of 0.5 or 1.0 be assumed for the MR shape factor for pointed and flat ended projectiles, respectively, if appropriate values have not been experimentally derived. Some additional information on the basis for establishing these shape factor values is given in Section 2.5.2.1.

The drag coefficient, in Table 2.6, is only required when the projectile penetrates a volumetric target component type V2 (see Section 2.5.2.2 for additional information). The drag coefficient is used to calculate the projectile velocity reduction in the fluid or non-coherent material contained in a V2 target component. It is noted that the projectile is assumed to move freely in air with no velocity reduction.

Table 2.6: Projectile (C) Data Summary

Data		Default Value	Variable Name	Array Name	Minimum Value	Maximum Value
Weight	[grains]	1 080.0	CM	CIN(1)	> 0.0	15 000.0
Base Diameter	[in]	0.47	CDT	CIN(2)	.2	1.5
Nose Length	[in]	0.577	CLN	CIN(3)	0.0	4.0
Nose Diameter	[in]	0.247	CDN	CIN(4)	0.0	1.5
Specific Weight	[lbs/in^3]	0.667	CRHO	CIN(5)	> 0.0	1.0
Brinell Hardness		285.0	CBHN	CIN(6)	10	1 000
Ultimate Strength	[psi]	133 500.0	CUS	CIN(7)	500	400 000
Shape Factor[1]	(VR)	1.2	CSF	CIN(8)	1.0	5.0
Shape Factor[1]	(MR)	0.4	PIF	CIN(9)	0.1	1.0
Drag Coefficient		1.0	CCD	CIN(10)	0.0	4.0

[1] Penetration (mass to volume) related shape factors

The encounter data listed in Table 2.7 describes the kinematics of the ballistic impact event. The initial projectile yaw (YAW) and yaw plane angle (YAWP) describe the orientation of the projectile with respect to the shot line, as shown in Figure 2.9. While the yaw angle describes the rotation of the projectile about its centroid, with respect to the shot line (z-axis), the yaw plane angle describes the rotational position of the projectile about the shot line (z-axis) with respect to the x-axis.

Table 2.7: Encounter (E) Data Summary

Data		Default Value	Variable Name	Array Name	Minimum Value	Maximum Value
Impact Velocity	[ft/sec]	6 000.0	V	EC(1)	> 0.0	10 000.0
Spin Rate	[rad/sec]	13 800.0	SPIN	EC(2)	5 000	25 000.0
Initial Yaw	[deg]	3.0	YAW	EC(3)	0.0	60.0
Yaw Plane Angle	[deg]	270.0	YAWP	EC(4)	0.0	180.0
First Impact Velocity	[ft/sec]	6 000.0	VSTART	--	> 0.0	10 000.0
Last Impact Velocity	[ft/sec]	6 000.0	VEND	--	> 0.0	10 000.0
Velocity Increment	[ft/sec]	1.0	VINC	--	> 0.0	10 000.0

The MPPM3 ballistic penetration software may be operated in batch mode which allows the penetration event to be modelled for a range of impact velocities ranging from an upper (VSTART) to a lower (VEND) bound impact velocity. The number of steps in the batch ballistic penetration modelling process is calculated based on the velocity increment value (VINC) provided by the user.

Table 2.8 outlines the data required to describe a target system. Since a target system or array may include more than one component, the NPLATE input data variable is used to identify the number of target system components which need to be described by the other data variables. Most of the target data is read from a file into a two dimensional array, PIN(I,#), whose indices refer to the target system component number and data item, respectively. Many of the target data variables are described in Figures 2.8 and 2.9.

Table 2.8: Target (P) Data Summary

Data	**Variable Name**	**Array Name**	**Minimum Value**	**Maximum Value**
Number of Target Components	NPLATE	--	1	20
Z-Axis Component Spacing [in]	S	PIN(I,1)	> 0.0	20.0
Component Type	PTYP	PIN(I,2)	--	--
Material Code	PMTL	PIN(I,3)	--	--
Brinell Hardness	PBHN	PIN(I,4)	10.0	1 000.0
Density Ratio	VRHOR	PIN(I,4)	0.1	1.0
X-Dir. Plate Normal Cosine	PNX	PIN(I,5)	0.0	0.5
Entrance Obliquity [deg]	OBLEN	PIN(I,5)	0.0	60.0
Y-Dir. Plate Normal Cosine	PNY	PIN(I,6)	0.0	0.5
Exit Obliquity[7] [deg]	OBLEX	PIN(I,6)	0.0	60.0
Z-Dir. Plate Normal Cosine[8]	PNZ	PIN(I,7)	0.0	0.5
Tipping Plate Obliquity [deg]	OBLTP	PIN(I,7)	0.0	60.0
Plate Normal Thickness [in]	PT	PIN(I,8)	> 0.0	2.0
Line-of-Sight Path Length [in]	VLOS	PIN(I,8)	> 0.0	60.0
Min Ricochet Obliquity[10] [deg]	RICOBL	--	0.0	90.0
Random No Generator Seed	RANDM	--	0.0	1 000.0
Penetration Model Print Flag	MTPPM	--	--	--

Several of the data values described in Table 2.8 share the same PIN(I,#) array location (e.g. PBHN and VRHOR). These data are mutually exclusive in that they are used to represent material properties for differing materials or they allow different systems of measurement to be used to describe their values. The following points describe the overlapping data variables:

- PIN(I,4) - Brinell hardness (PBHN) is collected for steel (ST) or aluminium (AL) plates, whereas, material density ratio (VRHOR) is used for volume mode components. For V1, V3 and V4 components, VRHOR is the ratio of the average component density to the density of the material corresponding to the input value of PMTL. For V2 components, VRHOR is the ratio of the density of non-coherent materials or fluids to the density of water (specific gravity).
- PIN(I,5) & PIN(I,6) - Entrance and exit obliquity (OBLEN/OBLEX) are entered in place of the *X*- and *Y*-direction plate normal cosines (PNX / PNY), as shown in Figures 2.8 and 2.9, for volumetric components. OBLEN determines the single plate obliquity for V1 components. OBLEN and OBLEX are used for obliquities of the first and last plates of V3 and V4 components. OBLEN and OBLEX are ignored for V2 components.
- PIN(I,7) - Tipping plate obliquity (OBLTP), see Figure 2.8, is entered in place of the *Z*-direction plate normal cosine (PNZ), as shown in Figure 2.9, for volumetric components V3 and V4.
- PIN(I,8) - The line-of-sight path length (VLOS), as shown in Figure 2.8, is entered for volumetric components, whereas the plate normal thickness (PT) is entered for plate components.

The last three target data variables, RICOBL, RAND and MTPPM, are not associated with a particular target system component and are thus not held in the data entry array PIN(I,#). RICOBL is the minimum impact obliquity at which the MPPM3 ricochet model is invoked if the impact velocity is less than the ballistic limit velocity for a particular plate. If a value greater than or equal to 90 degrees is entered for RICOBL, then the ricochet model will not be used. RAND is a seed for the random number generator used in V4 volumetric components to compute shot line areal densities (see Section 2.5.2.2 for more details on the differences between component types V3 and V4). The simulated results will always be the same for a given random number seed value. MTPPM is used in MPPM3 essentially as a flag to indicate whether the multiple thick plate penetration model (MTPPM) should printout results after each component or plate in the model is penetrated to develop a projectile velocity, position, etc.. time history. A value MTPPM = 0 will suppress printing, while a value of 1 will trigger the detailed printout.

The default data for the target system is S2M2 18 plate target array. The default data values for this target system are shown in Table 2.9 below.

Table 2.9: Parameters for S2M2 18 Plate Array

	S Element Spacing [in]	**PTYP** Element Type	**PMTL** Material Code	**PBHN** Brinell Hardness	**PNX** X-Dir Plate Normal Cosine	**PNY** Y-Dir Plate Normal Cosine	**PNZ** Z-Dir Plate Normal Cosine	**PT** Thickness [in]
1	0.00	P1	AL	120.0	0.00	-0.707	0.707	0.125
2	11.50	P1	AL	120.0	0.00	0.00	1.00	0.190
3	2.23	P1	AL	120.0	0.00	0.00	1.00	0.375
4	2.23	P1	AL	120.0	0.00	0.00	1.00	0.375
5	2.23	P1	AL	120.0	0.00	0.00	1.00	0.500
6	2.23	P1	AL	120.0	0.00	0.00	1.00	0.125
7	5.00	P1	AL	120.0	0.00	0.00	1.00	0.125
8	1.63	P1	AL	120.0	0.00	0.00	1.00	0.125
9	1.63	P1	AL	120.0	0.00	0.00	1.00	0.125
10	1.63	P1	AL	120.0	0.00	0.00	1.00	0.125
11	1.63	P1	AL	120.0	0.00	0.00	1.00	0.125
12	1.63	P1	AL	120.0	0.00	0.00	1.00	0.125
13	1.63	P1	ST	120.0	0.00	0.00	1.00	0.125
14	1.63	P1	ST	120.0	0.00	0.00	1.00	0.125
15	1.63	P1	ST	120.0	0.00	0.00	1.00	0.125
16	2.50	P1	AL	120.0	0.00	0.00	1.00	0.125
17	8.50	P1	AL	120.0	0.00	0.00	1.00	0.125
18	8.50	P1	AL	120.0	0.00	0.00	1.00	0.125

2.5.3.2 MPPM3 Embedded Parameters

Aside from the default target, encounter and projectile default data values, the MPPM3 software contains a library of target material properties. Table 2.10 lists the 15 materials included in the nominal material property database along with their material codes (PMTL).

Table 2.10: Target Component Material Codes

Material	Code
Aluminium	AL
Steel	ST
Titanium	TI
Copper	CU
Magnesium	MG
Lead	PB
GRP	GR
Doron	DO
Kevlar	KV

Material	Code
XP Plastic	XP
Lexan	LX
Ceramic (Al_2O_3) with woven-roving (GRP or Doron) backing	CW
Pyrex with woven-roving (GRP or Doron) backing	PW
Ceramic (Al_2O_3) with Kevlar backing	CK
Non-Coherent Material (fluid)	NM

The database of target materials contains both metallic and non-metallic materials whose behaviour to ballistic impact or mechanical properties are described by differing parameters. The parameters used to describe metallic and non-metallic plate materials are listed in Tables 2.11 and 2.12, respectively. Many of the listed metallic material properties have been related to the hardness of the material through some empirical equations. While the MPPM3 code is sufficiently clear to apply at this time it would be desirable to:

- determine the physical material properties which are represented by each parameter variable name used in the algorithms, and
- identify the range of validity of the empirical relationships which are used to evaluate parameters based on hardness.

Table 2.11: Metallic Target Material Property Definitions

Parameter	Variable Name	Relationships With Other Properties[1]
Unit Weight [lb/in^3]	PRHO	
Bulk Modulus [psi]	PBM	
Regressed from Exp.[2]	PBB	
C_τ[3] [ft/sec]	PCTAU	1) PCTAU = -0.0054•PBHN^2 + 2.46•PBHN + 984 2) PCTAU = -0.0203•PBHN^2 + 12.53•PBHN + 604
Regressed from Exp.[4]	PCS	3) PCS = -0.0896•PBHN^2 + 26.48•PBHN – 57.58 4) PCS = 0.00131•PBHN^2 + 3.02•PBHN + 2191
Regressed from Exp.[4]	PBS	5) PBS = 0.725 – 0.00035•PBHN
Regressed from Exp.[4] [ft/sec]	PCB1	6) PCB1 = 0.0164•PBHN^2 – 1.155•PBHN + 430 7) PCB1 = -0.0295•PBHN^2 + 17.25•PBHN + 2110
Regressed from Exp.[4] [ft/sec]	PCB2	8) PCB2 = -0.107•PBHN^2 + 9.767•PBHN + 4104 9) PCB2 = 2.258•PCB1
Regressed from Exp.[4]	PK	10) PK = -0.0146•PBHN^2 + 1.425•PBHN + 488

[1] Brinell Hardness (PBHN) is a user supplied data for steel and aluminium plates

[2] Likely an experimentally derived coefficient regressed to aid in the determination of normal incident limit velocities, therefore has no physical meaning.

[3] Correction factor to correct for steel and aluminium hardness in calculating V50.

[4] Likely an experimentally derived coefficient regressed to aid in the determination of limit velocities, residual and shatter velocities, therefore has no physical meaning.

Table 2.12: Non-Metallic Target Material Property Definitions

Parameter	Variable Name	Relationships With Other Properties
Regressed from Exp.[1]	PKS	
Regressed from Exp.[1]	PAS	
Regressed from Exp.[1]	PKB	
Regressed from Exp.[1]	PAB	
Average Density $[lb/ft^3]$	PRHOF	
Unit Weight $[lb/ft^3]$	PRHO	11) PRHO = PRHOF/1728

[1] Likely an experimentally derived coefficient regressed to aid in the determination of limit velocities, residual and shatter velocities, therefore has no physical meaning.

Based on the material property relationships presented in Tables 2.11 and 2.12, the default mechanical properties contained in MPPM3 for metallic and non-metallic materials are shown in Tables 2.13 and 2.14, respectively.

Table 2.13: Target Metallic Material Property Parameter Summary*

Material	PBHN	PRHO	PBM	PCTAU	PCS	PBS	PCB1	PCB2	PBB	PK
Aluminium	120	0.1	10.E6	1201 (eq-1)	1830 (eq-3)	0.61	528 (eq-6)	3735 (eq-8)	1.75	449 (eq-10)
Steel	150	0 283	23.E6	2027 (eq-2)	2673 (eq-4)	0.67 (eq-5)	4034 (eq-7)	9108 (eq-9)	0.61	0.0
Titanium	--	0.16	18.E6	1450	2660	0.75	1880	4700	1.0	350
Copper	--	0.32	19.E6	750	1424	0.65	913	1896	0.65	0.0
Magnesium	--	0.065	4.2E6	840	561	0.65	360	747	0.65	0.0
Lead	--	0.41	2 E6	100	2260	0.65	1450	3010	0.65	0.0

* Equations relate to material property parameter definitions (Table 2.11)

Table 2.14: Target Non-Metallic Material Property Parameter Summary*

Material	PKS	PAS	PKB	PAB	PRHOF	PRHO[1]
GRP	2725	0.72	1450	0.81	127	0.073
Doron	2725	0.72	1450	0.81	127	0.073
Kevlar	2410	0.38	1600	0.67	80	0.046
XP Plastic [2]	2410	0.38	1450	0.58	57	0.033
Lexan	2200	0.59	1600	0.67	80	0.046
Ceramic/Woven Backing	-1.0	-1.0	2100	1.0	181	0.105
Pyrex/Woven Backing	-1.0	-1.0	1950	1.0	138	0.080
Ceramic/Kevlar Backing	-1.0	-1.0	1700	1.0	156	0.090

[1] Based on equation presented in Table 2.12

[2] Unknown material type, possibly Experimental Plastic

2.5.3.3 MPPM3 Input File Formats

As will be discussed in Section 2.5.5, MPPM3 may be run in an interactive mode using the MPPM3 pre-processor prompts to collect the required input data (see Section 2.5.3.1) or the program may be run with user generated input files. The input file is a space delimited ASCII file of the form shown in Figure 2.10. The data input variable names are used in Figure 2.10 to illustrate the location of data within the input file. The variable names and ranges of acceptable value are described in Section 2.5.3.1. All of the input data values are real numbers with the exception of NPLATE and MTPPM which are integers.

```
Title Line
CIN(1)      CIN(2)      CIN(3)      CIN(4)
CIN(5)      CIN(6)      CIN(7)      CIN(8)      CIN(9)      CIN(10)
EC(1)       EC(2)       EC(3)       EC(4)
NPLATE      MTPPM       RICOBL      RANDM
PIN(I,1)
PIN(I,2)    PIN(I,3)    PIN(I,4)    PIN(I,5)    PIN(I,6)    PIN(I,7)    PIN(I,8)
PIN(I+1,1)
PIN(I+1,2)  PIN(I+1,3)  PIN(I+1,4)  PIN(I+1,5)  PIN(I+1,6)  PIN(I+1,7)  PIN(I+1,8)
     •
     •
     •
```

Figure 2.10: MPPM3 Input File Format

The input file illustrated in Figure 2.10 is set-up for a target system with two components. Additional components are added by replicating the last two lines of the input file format. To assemble a batch run input file the entire data structure is repeated. In other words a batch run with two simulation descriptions would include at least 14 lines of data (assuming single plate targets).

2.5.4 MPPM3 Output

The MPPM3 output is written to an ASCII data file whose name is supplied by the user and includes the extension ".out". All of the input data is included in the data file for reference prior to the penetration result data. All of the standard data printed to the output file are described in Table 2.15.

Table 2.15: MPPM3 Standard Output Data Summary

Parameter	Units	Definition
X, Y, Z - Impact Coordinates	[in]	For determination of impact yaw and presented area, impacts are presumed to occur when the projectile mass centre reaches the mid-point of plates and types V1 and V2. The projectile presented area at the mid-point of V2 components is used to compute the velocity decay over the entire length of the component (VLOS). Impacts for V3 and V4 components occur at the mid-point of the first plate in the component.
OBL - Impact Obliquity	[deg]	The effect of trajectory deviations from the z-axis on impact obliquity.
YAW	[deg]	Projectile yaw at the impact location.
LAMDA		Ratio of maximum impact bending stress to projectile material ultimate strength. The projectile is presumed to break when LAMDA exceeds a critical value (λ=1), and the residual mass and length are reduced by a factor of 2.
Mr	[grains]	Projectile residual weight behind the current target element.
BETA	[deg]	The angle between the pre-impact projectile trajectory and the post-impact trajectory. BETA is measured in the obliquity plane formed by the pre-impact velocity vector and the plate normal.
Vr	[ft/sec]	Projectile residual velocity behind the current target element.
V50	[ft/sec]	Ballistic limit velocity for current target element computer in RV.
VRV	[ft/sec]	Projectile residual velocity for thin plates computed in RV.
VTPPM	[ft/sec]	Projectile residual velocity for thick plates computed in TPPM.
Nose Diameter	[in]	Projectile nose diameter behind the current target element.
Projectile Length	[in]	Projectile length (total) behind the current target element.
Normalised Projectile Momentum Change		Change in projectile momentum through the target normalised by the pre-impact projectile momentum. A value of 1 indicates the projectile has been stopped by the target.

If the user opts to use the thick plate or combined penetration models (see Section 2.5.2.3) the MPPM3 software will prompt them to supply a TPPM output file name to which the extension ".prt" is appended. This additional output file provides a time history of the target system penetration process. The data included in this file is defined in Table 2.16.

Table 2.16: TPPM Output Data Summary

Parameter	Units	Definition
T	[μsec]	Time base for the penetration history description
P	[in]	Position of projectile leading edge referenced to position at time of impact
TP	[in]	Remaining thickness of target plate to be penetrated
GAM		Plate breakout parameter (e.g. GAM = 1 when breakout / penetration occurs)
L	[in]	Residual projectile length
V	[ft/sec]	Projectile residual velocity
U	[ft/sec]	Velocity of projectile / target interface
W	[ft/sec]	Target plug velocity

Since the source code is available, it would be possible to modify the output code to provide a customised output data file format.

2.5.5 Software Description - Structure and Operation

The following sections provide a technical description of the MPPM3 software and how it operates. The software code is written in standard Fortran 77 and compiled with Microsoft Fortran 5.0. It includes separate I/O and computational engine modules allowing for both interactive and batch run operation. While the computational engine containing the MPPM3 ballistic penetration model is of primary interest to this review, a brief description of the I/O module is provided in the next section followed by a more detailed description of the MPPM3 computational engine.

2.5.5.1 MPPM3 I/O Module

The MPPM3 software includes an interactive data entry and file handling pre-processor which operates in a text mode. This module of the MPPM3 software prepares input files for the main computational engine and including subroutines that can generate data files with the previously described default penetrator, encounter and target array data. The remaining subroutines within this first module of the MPPM3 software control the formatting within the program, that is, controlling on-screen cursor movements, text attributes, colours, and menu displays.

Menu options contained in the pre-processor module are used to prompt the user to direct the operation of the software. The main menu controls such options as: loading data from disk, saving data to disk, editing the current data, displaying the current data, running the penetration model, viewing the output results, and exiting the program. Once the user is satisfied with the penetrator, encounter and target array data, the MPPM3 subroutine is called. The subroutine calls or relationships between the various modules of the MPPM3 engine are described in the following section with both a description of the program architecture and a pseudo code description of the code.

2.5.5.2 MPPM3 Computational Engine Architecture

The architecture of the MPPM3 software is described in Figure 2.11 which illustrates the relationship between the MPPM3 modules. While the MPPM3 module relationship tree structure looks relatively busy it is made up of 13 basic modules including the MPPM3 mainline. Figure 2.11 illustrates the subroutine calls for the MPPM3 program.

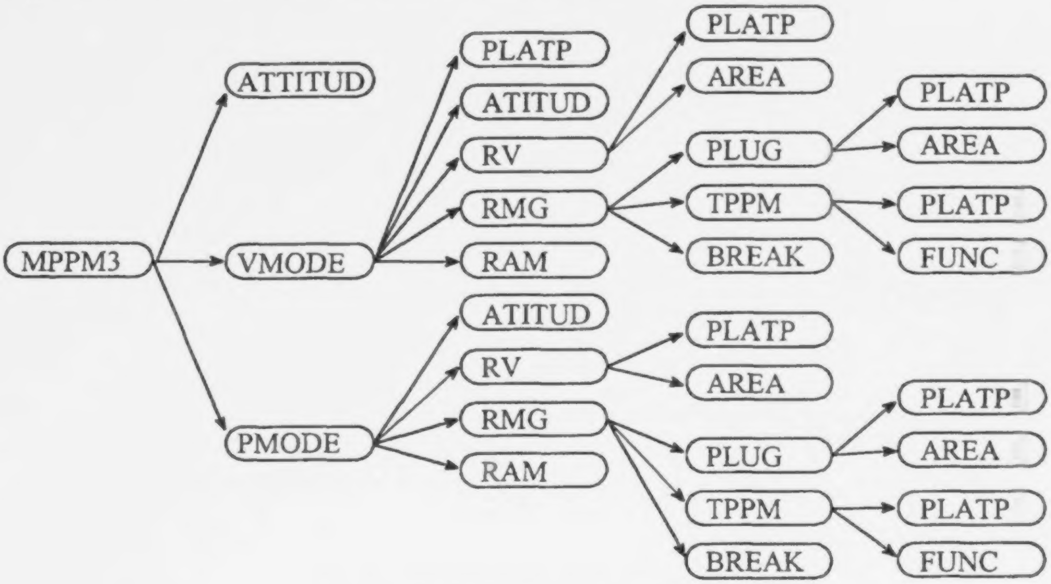

Figure 2.11: Subroutine Calls in MPPM3

2.5.5.3 MPPM3 Computational Engine Pseudo Code Description

2.5.5.3.1 SUBROUTINE MPPM3

Provides user interface, reads and prints input data, assigns initial values, assigns penetration results behind each plate to the output matrix.

```
1 – Set initial conditions.
2 – Initialise off-shot line displacement and velocity components. Initial impact presumed
    to occur on z-axis.
3 – Compute equivalent cylinder dimensions to preserve mass and axial moment of
    inertia.
4 – Initialise ceramic-hit flag and post-ceramic plate counter.
5 – Enter main do-loop to compute penetrator status after each impact. While I ≤
    IPLATE, do:
    1 – Fill output matrix with penetrator values in front of and behind the first plate
        and behind all remaining plates.
    2 - IF PTYPP = V3 or V4, then reset impact conditions to mid-point of first plate.
        ENDIF
    3 - Set previous target element type in order to print z-co-ordinate of first plate for
        V3 and V4 components.
    4 - Exit computational loop when CM or V is zero or exit conditions have been
        stored in out array.
        1 - IF $CM \leq 0$ or $V \leq 0$, then IPLATE = I.
        2 - IF I = IPLATE, then CONTINUE to 5 of main do-loop.
        3 - IF I = NPLATE + 1, then determine exit location and direction. CALL
            ATITUD
        4 - ENDIF
    5 - Select proper penetration methodology - Volume or Plate
        1 - IF PTYP = V, then CALL VMODE
        2 - ELSE, then CALL PMODE
        3 - ENDIF
    6 - Reset parameters for next impact. CONTINUE
6 – Print output results.
7 – Print out the normalised projectile momentum change.
```

2.5.5.3.2 SUBROUTINE ATITUD

Computes change in projectile attitude between plates.

```
1 – Compute azimuth and elevation of angular momentum vector and cone angle of
    penetrator.
2 – Compute current precession angle and new value for next impact.
3 – Compute direction cosines and yaw of penetrator at next impact.
4 – Compute direction cosines of transverse angular velocity at next impact.
```

2.5.5.3.3 SUBROUTINE VMODE

Supervises penetration calculations for volume mode components.

```
1 – IF PTYP = V1, then
    1 - Specify hardness of equivalent plate (needed only for steel and aluminium
        plates).
        1 - IF PMTL = AL, then PBHN = 120.0
        2 - IF PMTL = ST, then PBHN = 150.0
    2 – Assume equivalent plate obliquity defined by entrance obliquity. Assume y-z
        plane is obliquity plane.
    3 – Compute normal thickness of equivalent plate.
    4 – Determine impact co-ordinates, yaw, and obliquity at z-co-ordinate of
        component mid-point.
    5 - CALL ATITUD
    6 - CALL RV
    7 – Check for valid ceramic parameters.
    8 - CALL RMG
    9 – CALL RAM
2 – ELSEIF PTYP = V2, then
    1 - Determine impact co-ordinates, yaw, and obliquity at z-co-ordinate of
        component mid-point.
    2 - CALL ATITUD
    3 – Compute areal density of non-coherent materials ($lbs/ft^2$).
    4 - CALL RV
    5 – Check for valid ceramic parameters.
    6 – CALL RMG
    7 – CALL RAM
3 – ELSE – Default: (PTYP = 'V3' and 'V4') volume mode component represented by 15 aluminium plates and 3 steel plates separated by non-coherent material as determined for avionics components.
    1 – Get plate density. CALL PLATP
    2 – Compute areal density along path through component ($lbs/in^2$).
    3 – Compute total areal density of metallic plates in component plate array.
    4 – Compute normal thickness of aluminium and steel plates in representative plate array (inches).
    5 - Compute thickness of non-coherent material between metallic plates in representative plate array (inches).
    6 – Compute areal density of non-coherent material plates ($lbs/ft^2$)
    7 – Keep track of maximum lambda value while projectile passes through types 'V3' and 'V4' volume mode components.
    8 – Accumulate direction change as projectile passes through 'V3' and 'V4' components.
    9 – DO IPLT = 1 to 35 (loop through 35 plates of volume mode component)
        1 – IF CM or V = 0, then exit VMODE.
        2 - IF VZ $\leq 0$, then CONTINUE
            1 - Compute direction cosines for each plate component.
            2 – Set plate material type and normal thickness.
            3 – Determine impact co-ordinates, yaw, and obliquity at z-co-ordinate for this plate.
            4 - CALL ATITUD
            5 – Save impact conditions at first plate for output array.
            6 – CALL RV
            7 – CALL RMG
            8 – Hold maximum value for LAMB in LAMBMX.
            9 – CALL RAM
            10 – Reset parameters for next impact.
            11 – Accumulate direction change for printing when last component type is 'V3' or 'V4'.
4 – ENDIF
```

2.5.5.3.4 SUBROUTINE PMODE

Supervises penetration calculations for a plate element.

```
1 – Compute projectile co-ordinates, impact obliquity and projectile yaw at z-co-ordinate of plate centre.
2 – CALL ATITUD
3 – CALL RV
4 – Check for valid ceramic parameters.
5 – CALL RMG
6 – CALL RAM
```

2.5.5.3.5 SUBROUTINE RV

Computes projectile residual velocity for thin plates from the impact geometry and by calling PLATP to obtain the necessary ballistic limit constants.

```
1 – Compute effective value of projectile presented area.
2 – IF PMTL ≠ NM, then
    1 – CALL PLATP
    2 – Compute areal density ($lb/ft^2$) for flexible materials and ceramic materials.
    3 – Determine if nose shape is sharp or blunt. For blunt nose, the nose diameter
        (CDN) is equal to the base diameter (CDT). For sharp nose, the ratio of nose
        diameter to base diameter is less than or equal to 0.5 and the ratio of nose
        length to the difference between the base and nose diameters is greater than or
        equal to 1.0
        IF sharp, then set NSHP = 1,
        ELSEIF, set NSHP = 0.
    4 – Determine attack aspect (default ATK = 1).
        1 - IF NSHP = 0 or YAW ≥ 0.175, then ATK = 0
        2 - IF PMTL = ST and CBHN ≤ 560, then ATK = 0
    5 – Attack aspect for ceramics.
        1 - IF PMTL = CW and CBHN ≤ 560, then ATK = 0
        2 - IF PMTL = CK and CBHN ≤ 560, then ATK = 0
        3 - IF PMTL = PW and CBHN ≤ 560, then ATK = 0
    6 – Check invalid parameters for a sharp attack against ceramics.
    7 – Blunt attack check. IF ATK = 0 (blunt), then
        1 – Compute VX.
        2 – IF PMTL = GR, DO, KV, XP or LX (flexible materials), then compute
            V50 and VX.
            ENDIF
        3 - IF PMTL = CW, CK, or PW (ceramics), then compute V50 and VX.
            ENDIF
        4 – PMTL = ST or AL (by default), then
            1 – Compute plug-shear component ballistic limit velocity.
            2 – Compute V50 and VBLX for blunt attack.
            3 – Replace VXN by V50N when V < V50N or VXN > V50N.
        5 – Compute change in direction (in obliquity plane toward plate normal).
    8 – ELSEIF ATK ≠ 0 (sharp), then
        1 – Compute VBLX.
        2 - IF PMTL = GT, DO, KV, XP or LX (flexible materials), then compute
            V50 and VX.
        3 - IF PMTL = CW, CK, or PW (ceramics), then compute V50 and VX.
        4 – ELSEIF PMTL = ST or AL (by default), then compute V50 and
            VLBX.
    9 – Invoke simplified ricochet model.
    10 – Compute effective plate plug mass for residual velocity calculation. CALL
         AREA
```

3 – ELSEIF PMTL = NM, then compute velocity loss through non-coherent material. Note that areal density is used instead of thickness. Assume no direction change for these materials.
4 – Compute residual velocity components.

2.5.5.3.6 SUBROUTINE RMG

Computes projectile residual mass, velocity and geometry. An interpolation scheme is used for impacts at intermediate velocities against plates of intermediate thickness when the combined model is selected.

1 – For non-coherent material, projectile is assumed rigid.
  IF PMTL = NM, exit subroutine RMG
  ENDIF
2 – Neglect erosion/extrusion-shear mass loss when projectile ricochets.
3 – Use plate plug model if selected by user, or if the plate material is a ceramic.
  IF TMODEL = P or PMTL = CW or CK or PW, then ***CALL PLUG***
  ENDIF
4 – Use TPPM model if selected by user. Add ceramic material parameters to TPPM call statement.
  IF TMODEL = T, then ***CALL TPPM***
  ENDIF
5 – Select combined model (default).
6 – ***CALL PLUG*** to compute mass loss against thin plates at high impact velocities.
7 – Use TPPM to compute mass loss against thick plates of against thin plates near the ballistic limit velocity.
8 – Use TPPM for mass loss at or below the limit velocity or well above the hydrodynamic transition velocity.
    IF $V \leq V50$ or $V \geq 2.5VHD$, then ***CALL TPPM***
    ENDIF
9 – Use TPPM and interpolation equations for mass loss at intermediate velocities. Use plate plug velocity here.
10 – Modify transition formula to yield CMR = CMRT1 at V = 2.5*VHD
11 – Use PLUG and TPPM and interpolation formulas for mass loss against plates of intermediate thickness or against thin plates at intermediate velocities.
12 – Recalculate residual velocity for thick plates when impact velocity is greater than limit velocity.
13 – Determine if projectile broke. ***CALL BREAK***
14 – Calculate residual nose shape.
15 – Recalculate equivalent cylinder size when part of nose remains.

2.5.5.3.7 SUBROUTINE PLUG

Computes residual mass, length and diameter of the penetrator as functions of the plate and penetrator material properties, plate thickness and the pre-impact mass, length, diameter, velocity, yaw and obliquity of the penetrator.

1 – ***CALL PLATP*** to obtain plate properties.
2 – Use presented area of equivalent cylinder to determine length and diameter of equivalent unyawed cylinder.

3 – Compute thickness of equivalent normal plate.
4 – Use effective area and plate impact factor to determine effective rigid plug mass. ***CALL AREA***
5 – Compute remaining length, mass and velocity of equivalent cylinder after shock phase.
6 – Compute undeformed length of equivalent cylinder.
7 – After deformation phase – neglect deformation mass loss in thin aluminium plates.
8 – Compute estimate of CJ*TTAU and use Newton-Raphson method to determine TTAU.
9 – Compute mass, length and diameter of equivalent cylinder after deformation phase.
10 – Convert residual mass, length, and diameter to equivalent values for the yawed cylinder.

2.5.5.3.8 SUBROUTINE RAM

Computes projectile residual angular momentum after each impact.

1 – Compute components of velocity change.
2 – Set constant relating linear and angular momentum changes and compute components of change in angular momentum of residual penetrator.
3 – Compute pre-impact moments of inertia and pre-impact angular momentum components of residual penetrator.
4 – Compute moments of inertia and angular momentum components of residual penetrator.

2.5.5.3.9 SUBROUTINE PLATP

Contains plate parameters (see Section 2.5.1.4.7 for plate material properties)

1 – Determine plate material and compute or assign appropriate material properties.

2.5.5.3.10 SUBROUTINE BREAK

Determines projectile break-up.

1 – Break-up calculation for ricochet.

2.5.5.3.11 SUBROUTINE AREA

Computes effective plate plug cross-sectional area.

1 – Computes effective plate plug cross-sectional area.

2.5.5.3.12 SUBROUTINE TPPM

Determines equivalent, unyawed, cylinder dimensions, introduction of the minimum interface velocity for applications to thin plates, introduction of the extrusion/shear mass loss computation, and elimination of the debris model.

1 – ***CALL PLATP***
2 – Use presented area of equivalent cylinder to compute length and diameter of equivalent unyawed cylinder.
3 – Calculate dimensionless parameters for TPPM.
4 – Calculate flow stress for unconfined plate material (uniaxial stress).
5 – Set initial values for penetration flags.
6 – Set initial values for dependent variables.

7 – Set initial interface velocity. Avoid interface velocity less than 0. Avoid divide by 0 when plate and projectile identities are equal. Avoid interface velocities greater than projectile velocity and avoid negative square roots.
8 – Integrate penetration equations using fifth-order Runge-Kutta procedure. ***CALL FUNC.***
9 – Kinematic constraints on projectile, interface, and plug velocities. If length becomes negative or zero, equate projectile and interface velocities to plug velocity.
10 – Flow stress in plate corresponds to uniaxial stress conditions (i.e., permit plug to continue erosion beyond breakout). New flow stress value assigned in FUNC.
11 – Once deformation has begun, length cannot decrease faster than UCV.
12 – Reassign integration history array values.
13 – Set indices denoting breakout and beginning of deforming and rigid penetrator behaviour.
14 – Redefine CMR when length = 0 in case LEESD and LESD produce non-zero value.
15 – Restore extrusion shear mass loss for aluminium plates.

2.5.5.3.13 SUBROUTINE FUNC

Contains the differential penetration equations for thick plate penetration model TPPM.

1 – Constraints are required in FUNC as well as TPPM because of calls to FUNC at intermediate time steps before computing dependent variables. Flow stress in plate corresponds to uniaxial stress conditions (i.e., permit plug to continue erosion beyond breakout). Also, plug shear resistance set to zero after breakout.
2 – Modify and rearrange kinematic constraints on V, U, and W.
3 – Projectile and target defeat criteria.
4 – Allow plug to erode under uniaxial stress after breakout.
5 – Once deformation has begun, length cannot decrease faster than UCV.
6 – Allow plug to erode under uniaxial stress after breakout.
7 – Continuity at beginning of deformation and which recognises combined effects of enlarged frontal area of deformed penetrator and that all plate material in path of penetrator is not accelerated to velocity U.
8 – Allow plug to erode under uniaxial stress after breakout.
9 – Define flow factor for when deformation does not occur prior to rigid penetration (will only occur when U = V at T = 0).

3.0 CHARACTERISATION PROCESS

3.1 Characterisation Process Introduction

3.1.1 Characterisation Process Overview

The characterisation process included in DeCaM includes eight steps as shown in Figure 3.1. The user may direct DeCaM to perform the characterisation based on witness pack threshold curves or its analytic characterisation process. The threshold curve characterisation process, step 4b, is not available in DeCaM version 1.1. In addition, the user may select to use a specified shape factor which would remove steps 6 and 7 from the characterisation process. The DeCaM characterisation process optimised the shape factor to match the total mass of fragments to the change in target mass for all of the results discussed in this report.

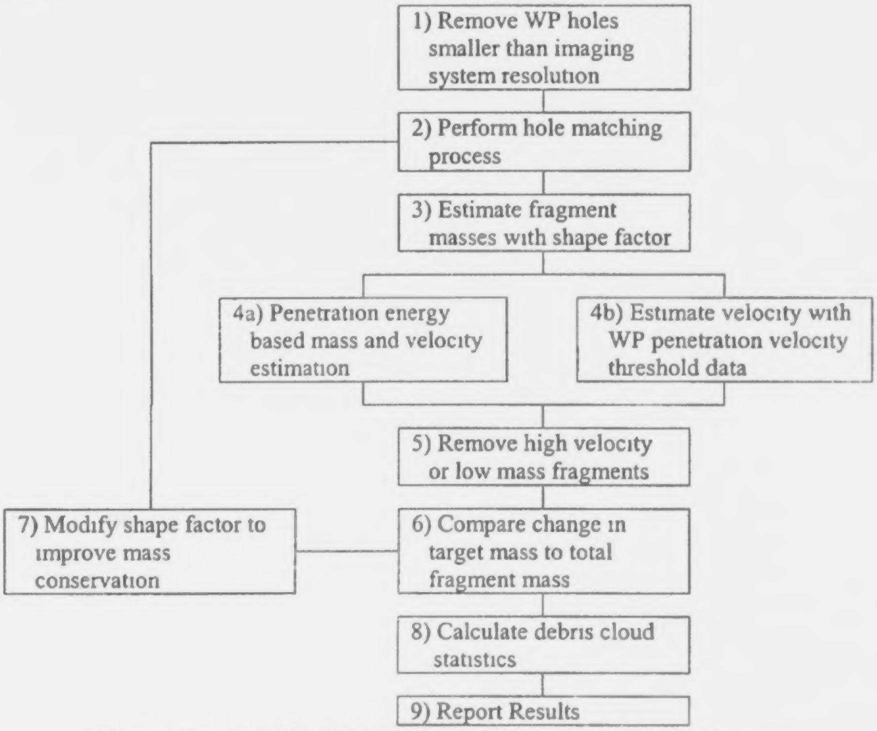
1) Remove WP holes smaller than imaging system resolution
2) Perform hole matching process
3) Estimate fragment masses with shape factor
4a) Penetration energy based mass and velocity estimation
4b) Estimate velocity with WP penetration velocity threshold data
5) Remove high velocity or low mass fragments
7) Modify shape factor to improve mass conservation
6) Compare change in target mass to total fragment mass
8) Calculate debris cloud statistics
9) Report Results

Figure 3.1: DeCaM BA Debris Characterisation Process

3.1.2 Scope of Characterisation Process Improvement

The sections which follow provide descriptions of the work completed in the improvement and validation of the DeCaM characterisation process. This work is presented in the following three sections:

- Improvements in the hole matching process,
- Development of witness pack penetration threshold curves, and
- Comparison of BA-debris characterisation results.

In each of these sections, some background is given on the operation of DeCaM 1.1 along with the improvements made in the development of DeCaM 3.0.

3.2 Hole Matching Process

3.2.1 Hole Matching Process Introduction

To properly analyse witness pack based behind-armour debris data, all of the holes produced by a single fragment must be grouped. Only those witness pack fragment holes in the plate closest to the rear (plate # 4) of the witness pack in each group should be used in the debris characterisation. The grouping of witness pack holes which are assumed to be produced by the same fragment is illustrated in Figure 3.2.

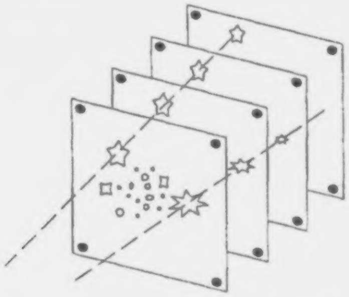

Figure 3.2: Grouping Witness Pack Holes on Successive Plates

In order to group holes and eliminate all but those which represent the final penetrations of debris fragments the witness pack plates are examined in pairs. The co-ordinates identifying the location of the witness pack hole centroids are adjusted to represent the *X* and *Y* locations of the fragment centroid when they passed the Z^* reference plane (as described in the previous section). When comparing any two successive plates in the matching process, the plate furthest from the target or debris origin is identified as the leading plate and the other plate in the pair being examined is the trailing plate. With this nomenclature in mind, the hole matching process currently used in DeCaM may be summarised into the following steps:

- Select each plate in the witness pack in turn as the leading plate, starting at the rear of the witness pack and ending at the second plate, to identify the holes on the trailing plate which correspond to its holes
- Select each hole on the leading plate in turn and compare their size (A_r) and location (S_r) to each hole on the trailing plate (see Figure 3.3). This comparison is made for each pair based on the following ratios:

$$A_r = \frac{A_{max}}{A_{min}}$$

$$S_r = \frac{S_c}{D_{min}}$$

$$D_{min} = 2 \cdot \sqrt{\frac{A_{min}}{\pi}}$$

$$S_c = R_1^2 + R_2^2 - 2R_1R_2\cos(\gamma)$$

$$\gamma = \theta_1 - \theta_2$$

Where:

A_r	hole area ratio
$A_{max,\ min}$	minimum and maximum areas of the two holes being compared
S_r	hole centroid separation ratio
S_c	distance between the centroids of the two holes being compared
D_{min}	diameter of the smaller of the two holes being compared
$R_{1,\ 2}$	radius of each hole from the debris centroid
$\theta_{1,\ 2}$	angular location of witness plate holes

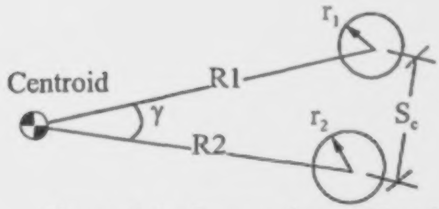

Witness plate hole locations on the characterisation reference plane.

Figure 3.3: Comparison of Leading and Trailing Hole Locations

The separation between hole centroids (S_c) is calculated based on the radial location of the hole centroids with respect to the debris cloud centroid (see Figure 3.3).

- Calculate the matching "Score" for each pair of holes:

$$\text{Score} = A_r \times S_r$$

- Calculate the maximum allowable hole separation (S_{max}) for the pair of holes being considered:

$$S_{max} = \text{Tolerance Factor} \times (r_1 + r_2)$$

- Sort the hole matching scores for all of the leading and trailing plate hole combinations in ascending order. As the hole matching score ($= A_r \times S_r$) approaches zero the quality of the match between two holes is assumed to improve since a hole area ratio (A_r) value of unity indicates that the holes were exactly the same size and a separation ratio (S_r) of zero denotes holes with coincident centroids.
- Select each leading and trailing hole score, in the sorted list, in turn and identify the leading and trailing holes as matched to each other; if they are as yet unmatched and their separation is less than the maximum allowable ($S_c \leq S_{max}$)

Once this matching and elimination process has been completed for all neighbouring pairs of witness pack plates all of those holes which are produced by a single fragment which precede the final plate penetration should be flagged for removal from the data set. The final characterisation of the BA debris will be based on those witness pack holes which were not marked for removal from the data set.

The process which is described above will not properly match and eliminate holes if irregularities exist in either the fragment penetration or data collection steps of the BA debris test procedure. The following list outlines the potential sources of error to which the matching and elimination process is vulnerable:

- erroneous inclusion or omission of a witness pack hole(s) in the data file due to electronic imaging system or human error
- spalling or fragmentation of a witness pack plate could produce unwanted leading plate holes
- further fragmentation of debris while passing the trailing plate will increase the number of holes on the leading plate, some of which will not have a match on the trailing plate
- significant changes in fragment trajectory resulting from the penetration of the leading plate will impede the matching and elimination process
- overlapping fragment holes will be interpreted as a single larger fragment which will cause an error in the estimation of the number of fragments and the distribution of fragment size and velocity

In order to identify the significance of these errors a warning, which appears when these errors become significant, was incorporated in the BA debris characterisation software to alert the user.

3.2.1 Hole Matching Process Improvements

The hole matching process was reviewed in an effort to improve its ability to accurately trace the path of fragments through the witness pack. If one assumes that fragment yaw angles do not change during the witness pack penetration process and that fragments decelerate as they penetrate each witness pack plate, then it is possible to say that holes produced by a single fragment in multiple witness pack plates should decrease in size towards the rear of the witness pack. This conclusion is based on the idea that fragment velocity is related to hole growth.

When completing the hole matching process, the number of fragments which pass through the large central hole in the first witness pack hole may be estimated as follows:

$$N_x = \frac{r_i N_{mo} - r_m N_o(r_i)}{r_m - r_i}$$

where:		
	N_x	number of fragments passing through central hole
	N_{mo}	total number of observed fragments
	$N_o(r_i)$	number of fragments observed in radius i
	r_i	radius i about the debris pattern centroid
	r_m	maximum debris radius

This is based on the observation (Recht 1969) that the number of holes contained in concentric circles increases linearly with circle radius.

3.3 WP Penetration Threshold Curves

3.3.1 WP Penetration Threshold Curve Introduction

As an improvement to the quality of the DeCaM 1.1 characterisation process, relationships were formulated between the mass of armour debris fragments and the required minimum velocity to penetrate a specified number of plates in the witness pack. These relationships were developed graphically and are referred to as "Threshold" curves or equations. The threshold curves are plotted by fitting power function regression curves to the experimental data. The sections which follow describe the data, development and resulting threshold curves.

3.3.2 Threshold Curve Experimental Data

The experimental program was conducted at the Ballistics Laboratory of the TNO-Prins Maurits Laboratory within the scope of Implementing Arrangement 11 of the CA/NL Memorandum of Understanding (Verolme, 1999). Fragment simulating projectiles (FSP's) were fired at witness packs in order to develop witness pack threshold curves. By firing FSP's of different masses at various initial velocities, "threshold curves" relating the minimum velocity required to penetrate each plate in the witness pack can be developed. Different probability of penetration velocity curves were calculated from experimental test data using the Kneubuehl methodology (Kneubuehl, 1996). Table 3.1 describes the geometry and mass of the FSP's involved in the threshold curve development experimental program. Table 3.2 describes the configuration of the two witness packs for which threshold curves were developed. The two witness pack configurations M1 and M2 represent standard DREV and TNO-PML configurations. Both witness pack configurations respect the procedures defined in the NATO Standard STANAG 4190 (NATO, 1996).

Table 3.1: FSP Geometric Parameters

Mass	**D**	**L/D**
[g]	**[mm]**	
0.162	2.65	1.21
0.486	4.05	1.14
1.10	5.38	1.18
2.85	7.7	1.01
5.30	9.10	1.14
13.4	12.9	1.01

Table 3.2: Witness Pack Configurations

Pack ID	Plate No.						
	1	2	3	4	5	6	7
	1mm al	1mm al	3mm al	1.5mm st	1.5mm st	1.5mm st	1.5mm st
M1-DREV	2024-T3	2024-T3	2024-T3	St 37-2	St 37-2	St 37-2	St 37-2
M2-PML	99.5 F11	99.5 F11	99.5 F11	St 37-2	St 37-2	St 37-2	St 37-2

where: al = aluminium, and st = steel

3.3.3 Penetration Velocity Threshold Curve Regression

The witness pack penetration threshold velocity experimental program results provided in Table 3.3 include the velocity of penetration at each plate of the witness pack. Each column represents the results generated for a witness pack and an FSP mass combination. The results are presented for each successive plate in a pack (i.e. 1 = plate 1, 2 = plates 1 & 2, 3 = plates 1, 2 & 3, etc..). This data is used to fit a regression equation of the form:

$$\text{Velocity} = \text{a Mass}^{b}$$

in which Velocity can be V_{50}, V_{90} or V_{95} and Mass is the FSP mass in grams. The velocity subscript "x" for the V_x parameter defines the velocity at which the fragments have an "x" percent probability of not perforating the plates.

The regression equations relate the mass of armour debris fragments and the required minimum velocity to penetrate the plates of a witness pack. The penetration threshold velocity equations for each witness pack plate all have a common form, differing only in the numerical value of the coefficient and power. The regression coefficients a and b were estimated for each plate in each witness pack for each of the V_{50}, V_{90} and V_{95} penetration velocities. These coefficients are shown in Table 3.4.

Table 3.3: WP-Calibration Data

V50	**0.162_M2**	**0.162_M1**	**0.486_M2**	**0.486_M1**	**1.1_M2**	**1.1_M1**	**2.85_M2**	**2.85_M1**	**5.3_M2**	**5.3_M1**	**13.4_M2**	**13.4_M1**
1	187.2	224.2	127.5	182.5	111.0	155.0						
2	313.8	346.3	219.4	275.0	173.8	216.9	142.5	170	115.0	147.5		
3			467.5	567.5	347.5	435.0	266.7	280	223.3	248.8		
4			713.3		510.8	672.5	382.3	450.6	342.5	363.8	235.4	280.0
5					716.2	932.5	519.5	617.5	399.4	472.5	286.7	327.5
6							685.8	762.5	511.7	551.3	418.8	436.3
7									619.2	675.0	473.9	515.0
V90	**0.162_M2**	**0.162_M1**	**0.486_M2**	**0.486_M1**	**1.1_M2**	**1.1_M1**	**2.85_M2**	**2.85_M1**	**5.3_M2**	**5.3_M1**	**13.4_M2**	**13.4_M1**
1	168.7	205.4	124.3	179.3	108.4	155.0						
2	303.0	334.2	205.5	256.9	171.0	209.9	139.3	170	115.0	143.0		
3			438.7	554.3	344.3	409.8	246.2	275.5	195.2	238.6		
4			710.3		503.0	646.3	371.9	414.9	330.9	335.6	226.0	270.9
5					689.0	901.8	505.0	614.3	391.4	464.6	271.6	315.9
6							656.8	745.5	499.7	530.4	398.3	404.0
7									613.4	675.0	454.7	495.0
V95	**0.162_M2**	**0.162_M1**	**0.486_M2**	**0.486_M1**	**1.1_M2**	**1.1_M1**	**2.85_M2**	**2.85_M1**	**5.3_M2**	**5.3_M1**	**13.4_M2**	**13.4_M1**
1	163.5	200.1	123.4	178.4	107.7	155.0						
2	300.0	330.7	201.6	251.7	170.2	208.0	138.4	170	115.0	141.7		
3			430.6	550.5	343.4	402.6	240.4	274.2	187.3	235.7		
4			709.5		500.9	638.9	368.9	404.8	327.7	327.6	223.3	268.4
5					681.3	893.1	500.9	613.4	389.1	462.4	267.3	312.7
6							648.5	740.7	496.3	524.5	393.6	394.9
7									611.8	675.0	449.3	489.3

Table 3.4: Coefficients and Powers for WP Threshold Curve Formula

		V_{50}		V_{90}		V_{95}	
WP	**Plate no**	**Constant a**	**Power b**	**Constant a**	**Power b**	**Constant a**	**Power b**
M1	1	158.22	-0.1924	158.7	-0.1457	158.86	-0.1317
	2	223.2	-0.2498	215.74	-0.241	213.6	-0.2383
	3	437.57	-0.3624	422.5	-0.3629	418.16	-0.363
	4	673.03	-0.3504	632.3	-0.3479	620.69	-0.347
	5	962.96	-0.4194	943.67	-0.4213	938.13	-0.4218
	6	1059.7	-0.3522	1077.9	-0.3878	1083.8	-0.3985
	7	1097.9	-0.2917	1178.9	-0.3344	1203.7	-0.3469
M2	1	110.38	-0.2771	108.7	-0.2335	108.25	-0.2201
	2	184.08	-0.2792	178.9	-0.2671	177.43	-0.2636
	3	367.94	-0.3058	348.58	-0.3379	343.05	-0.3506
	4	549.97	-0.3202	542.34	-0.3314	540.23	-0.3347
	5	748.58	-0.3695	727.45	-0.3745	721.49	-0.376
	6	914.46	-0.3106	889.45	-0.317	880.06	-0.3169
	7	1001.5	-0.2883	1050.8	-0.3228	1065.8	-0.3328

Tables 3.5 to 3.7 present the extrapolated witness pack threshold test data (of Table 3.3) based on the regression equation and coefficients shown in Table 3.4. This information is used to create the threshold curves. The values shown in italics in Tables 3.5 to 3.7 are estimated using the regressed penetration threshold relationships.

Table 3.5: Extrapolated V_{50} Witness Pack Threshold Data

FSP	**M1 Witness Pack Plate no.**						
Mass [g]	**1**	**2**	**3**	**4**	**5**	**6**	**7**
0.162	224.2	346.3	*846.3*	*1273.6*	*2066.0*	*2011.8*	*1867.0*
0.486	182.5	275.0	567.5	*866.6*	*1303.3*	*1366.3*	*1355.1*
1.1	155.0	216.9	435.0	672.5	932.5	*1024.7*	*1067.8*
2.85	*129.4*	170.0	280	450.6	617.5	762.5	*808.8*
5.3	*114.9*	147.5	248.8	363.8	472.5	551.3	675.0
13.4	*96.0*	*116.7*	*170.8*	280.0	327.5	436.3	515.0
20	*88.9*	*105.6*	*147.8*	*235.6*	*274.1*	*368.9*	*458.2*
FSP	**M2 Witness Pack Plate no.**						
Mass [g]	**1**	**2**	**3**	**4**	**5**	**6**	**7**
0.162	187.2	313.8	*641.9*	*985*	*1467*	*1609.5*	*1692.6*
0.486	127.5	219.4	467.5	713.3	*977.3*	*1144.2*	*1233.1*
1.1	111.0	173.8	347.5	510.8	716.2	*887.7*	*974.3*
2.85	*82.5*	142.5	266.7	382.3	519.5	685.8	*740.5*
5.3	*69.5*	115.0	223.3	342.5	399.4	511.7	619.2
13.4	*53.7*	*89.1*	*166.4*	235.4	286.7	418.8	473.9
20	*48.1*	*79.7*	*147.2*	*210.7*	*247.5*	*360.6*	473.9

Table 3.6: Extrapolated V_{90} Witness Pack Threshold Data

FSP	M1 Witness Pack Plate no.						
Mass [g]	**1**	**2**	**3**	**4**	**5**	**6**	**7**
0.162	205.4	334.2	*817 89*	*1191*	*2032*	*2183 4*	*2166 8*
0.486	179.3	256.9	554 3	*812.7*	*1279*	*1425 9*	*1500 6*
1.100	155.0	209.9	409.8	646 3	901 8	*1038 8*	*1141.9*
2.850	*136 2*	170.0	275.5	414.9	614.3	745.5	*830.5*
5.3	*124 4*	143.0	238 6	335.6	464.6	530.4	675.0
13.4	*108.7*	*115.4*	*164.7*	270.9	315.9	404 0	495.0
20.0	*102 5*	*104 8*	*142 4*	*222 9*	*267 1*	*337.3*	*432 9*
FSP	**M2 Witness Pack Plate no.**						
Mass [g]	**1**	**2**	**3**	**4**	**5**	**6**	**7**
0.162	168.7	303 0	*644 54*	*991 4*	*1438*	*1583 8*	*1891*
0.486	124.3	205.5	438 7	710.3	*953 1*	*1118*	*1326 4*
1.1	108 4	171.0	344.3	503.0	689.0	*862 98*	*1019*
2.85	*85.10*	139.3	246.2	371 9	505.0	656.8	*749.37*
5.3	*73.63*	115.0	195.2	330.9	391 4	499.7	613.4
13.4	*59.29*	*89 45*	*145 10*	226 0	271 6	398.3	454.7
20	*54 00*	*80 37*	*126 75*	*201*	*236 9*	*344 11*	*399 53*

Table 3.7: Extrapolated V_{95} Witness Pack Threshold Data

FSP	M1 Witness Pack Plate no.						
Mass [g]	**1**	**2**	**3**	**4**	**5**	**6**	**7**
0.162	200.1	330 7	*809 63*	*1167*	*2022*	*2238 5*	*2263.3*
0.486	178.4	251.7	550 5	*797 3*	*1272*	*1444 9*	*1546.1*
1.1	155.0	208.0	402.6	638.9	893.1	*1043 4*	*1164.6*
2.85	*138 39*	170.0	274.2	404.8	613.4	740.7	*837.01*
5.3	*127 53*	141 7	235.7	327 6	462.4	524 5	675.0
13.4	*112 87*	*115 08*	*163 01*	268 4	312 7	394.9	489.3
20	*107.07*	*104 61*	*140 95*	*219 5*	*265 1*	*328 46*	*425 79*
FSP	**M2 Witness Pack Plate no.**						
Mass [g]	**1**	**2**	**3**	**4**	**5**	**6**	**7**
0.162	163.5	300.0	*649 38*	*993 5*	*1430*	*1566 8*	*1953.2*
0.486	123.4	201.6	430 6	709.5	*946 4*	*1106 2*	*1355.1*
1.1	107.7	170.2	343 4	500 9	681.3	*853 88*	*1032 5*
2.85	*85 96*	138.4	240.4	368.9	500.9	648.5	*752.15*
5.3	*74 99*	115.0	187.3	327.7	389.1	496.3	611.8
13.4	*61 14*	*89.52*	*138 10*	223 3	267.3	393.6	449.3
20 0	*55 98*	*80 55*	*120 01*	*198 21*	*233 91*	*340 58*	*393 27*

3.3.4 Witness Pack Penetration Velocity Threshold Curves

Figure 3.4 illustrates the V_{50} threshold curves for the plates in the M2 witness pack as an example. The heavy lines in the graph represent the portion of the curve in which the experimental data allows interpolation, while the dashed portions of the threshold curves have been extrapolated based on the experimental data.

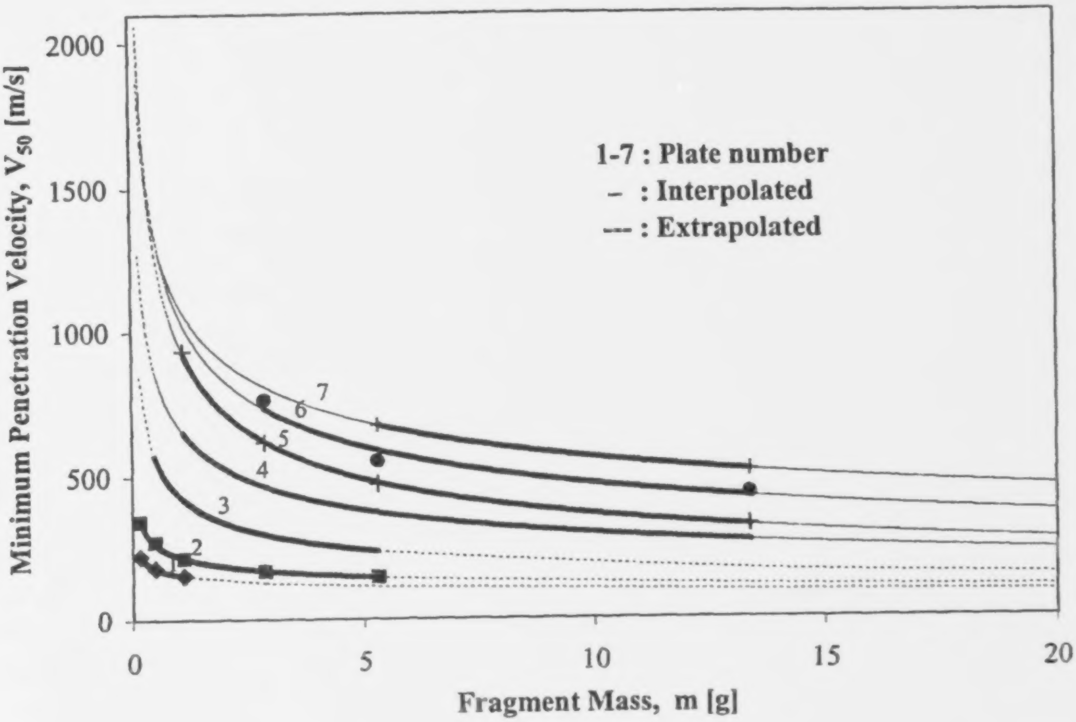

Figure 3.4: M1 Witness Pack V_{50} Penetration Threshold Velocity Curves

The remainder of the threshold curves are contained in the Excel spreadsheet accompanying this report. The ability to use this threshold data has been incorporated into the DeCaM software. The user may specify a data file containing the witness pack threshold curve coefficients which would be similar in form to that shown below for the V_{50} penetration velocities in the M1 witness pack. The witness pack penetration threshold curve data file includes a header text block to identify the data followed by a row of data for each plate in the witness pack. Each witness pack plate data row contains the "A" and "B" coefficients for the threshold velocity regression equation.

Table 3.8: Typical Witness Pack Penetration Velocity Threshold Data File

```
M2, v50, 7
110.38, -0.2771
184.08, -0.2792
367.94, -0.3058
549.97, -0.3202
748.58, -0.3695
914.46, -0.3106
1001.5, -0.2883
```

If the user does not specify the name of a witness pack threshold penetration velocity data file, the DeCaM software will use the existing analytical characterisation technique.

3.4 Characterisation and Comparison of WP BA Debris Data

3.4.1 Characterisation and Comparison of WP BA Debris Data Introduction

Recent improvements to the Debris Characterisation and Modelling (DeCaM) software have improved its modelling and characterisation abilities. This section presents a comparison of the behind armour (BA) debris witness pack characterisation results for DeCaM versions 1.1 and 2.0. The comparison is completed for ten witness pack data sets.

The primary objective of this review is to compare the BA debris characterisation results of DeCaM version 1.1 with those generated with and without threshold curves in DeCaM 2.0. In addition, the characterisation results are compared with experimentally observed data as a preliminary validation.

3.4.2 BA Debris Witness Pack Experimental Data

The behind armour debris captured in witness packs in the 3500 experiment series are used in this report as the basis of comparison of the characterisation ability of the DeCaM software. The data set includes ten BA-debris tests identified as Test 3527 to Test 3536. The projectile, target plate and witness pack data used by the DeCaM software to describe the BA debris experiments, for the characterisation process, are listed in Table 3.9. These tests were completed at the TNO-Prins Maurits Ballistics Laboratory in the Netherlands under a Memorandum of Understanding in 1996. The tests included the firing of 12.7mm Dutch AP/I ammunition against a 10mm thick rolled homogenous Armour (RHA) steel plate at three different impact velocities.

Table 3.9: Data Used in DeCaM BA Debris Characterisation Process

Parameter	Value	Parameter	Value
Witness Pack Angle [deg]	0.0	Location of impact point [cm]	X: 31.00 Y: 31.00 Z: -70.00
Witness pack plate spacing [cm]	2.54	Projectile mass [g]	26.0
Z reference [cm]	70.0	Impact velocity [m/s]	*
Target thickness [mm]	10.0	Projectile base diameter [mm]	12.7
Target density [kg/m^3]	7850	Imaging resolution [cm^2]	0.006
Young's Modulus [GPa]	207	Minimum allowed mass [g]	0.000
Target yield strength [MPa]	900	Matching area ratio	4.0
Fracture toughness [MPa m$^{1/2}$]	100.0	Matching radius multiplier	1.5
Minimum fragment size [cm^2]	0.000	Matching minimum distance [cm]	0.5
Target obliquity [deg]	0.0	Projectile X window offset [cm]	5.0
Fragment shape factor [m^2/kg$^{2/3}$]	**	Projectile Y window offset [cm]	5.0
Target hole side slope [deg]	30	Number of projectile fragments	1
Target mass before test [g]	*	Plate data file type	*
Target mass after test [g]	*	Number of plates	*

* Unique to each test (See Table 3.10) ** Calculated in the characterisation process (see Table 3.15)

Experimental conditions unique to each test and experimental measurements are listed in Table 3.10. The final target mass was set to zero and the change in target mass was used as the initial mass in the DeCaM characterisation process.

Table 3.10: Experimental Data and Measurements Unique to Each Test

Test Number	Change in Target Mass [g]	Impact Velocity, V_I [m/s]	Velocity Overmatch, V_I / V_{50}	Proj. Residual Velocity, V_R [m/s]	Debris Velocity, V_D [m/s]
3527	10.0	693.6	1.98	557.9	--
3528	10.0	699.9	2.00	514.6	--
3529	6.0	705.4	2.02	553.1	231.3
3530	11.0	697.8	1.99	505.2	222.5
3531	8.0	542.4	1.55	345.9	--
3532	10.0	521.1	1.49	303.1	--
3533	10.0	541.0	1.55	327.0	--
3534	10.0	627.4	1.79	460.5	--
3535	8.0	628.5	1.80	465.6	--
3536	10.0	622.3	1.78	446.0	--

3.4.3 Comparison of Characterisation Results

In this section the DeCaM witness pack BA debris characterisation results are reviewed. Comparisons are drawn between the earlier version (1.1) and the most recent version (2.0) of DeCaM. As noted in Section 3.1.1, DeCaM version 2.0 allows debris characterisation based on an analytic approach (DeCaM 2.0) and based on experimentally derived velocity threshold curves (DeCaM 2.0T). While the threshold velocity curve characterisation approach (DeCaM 2.0T) may be completed on a witness pack plate V_{50} or V_{95} penetration basis, in the comparisons which follow, unless otherwise stated, DeCaM 2.0T results refer to the V_{50} threshold velocity curve characterisation approach.

3.4.3.1 Comparison of DeCaM Characterisation Results

A comparison of the BA debris characterisation results from DeCaM 1.1, DeCaM 2.0 and DeCaM 2.0T with witness pack velocity threshold curves is tabulated in Appendix A for the ten experiments described in Tables 3.9 and 3.10. The characterisation result comparison for test 3536 is shown below in Table 3.11 as a sample and a basis of further discussion.

In general, fragment velocities estimated by DeCaM 1.1 are much higher than those inferred from the witness pack data by DeCaM 2.0 or DeCaM 2.0T. The lowest estimated fragment velocities appear to be provided by DeCaM 2.0T. The difference between the DeCaM 2.0 and DeCaM 2.0T fragment velocity estimates may be attributed to the fact that the DeCaM 2.0T velocities are lower bound values whereas, the DeCaM 2.0 velocity values are average values. In other words in DeCaM 2.0, a fragment penetrating the third plate in the witness pack would be characterised as having a velocity consistent with the average energy required to penetrate the third and fourth witness pack plates. In DeCaM 2.0T a fragment penetrating the third plate in the witness pack would be assigned the minimum velocity it required to penetrate the third witness pack plate. This difference could be easily removed.

Table 3.11: Test 3536 Comparison

WP Plate Hole No.*	WP Hole Area [cm²]	DeCaM 1.1 - Penetration Energy			DeCaM 2.0 - Penetration Energy			DeCaM 2.0T - Velocity Threshold Curves		
		Mass [g]	Vel. [m/s]	Next Hole[†]	Mass [g]	Vel. [m/s]	Next Hole[†]	Mass [g]	Vel. [m/s]	Next Hole[†]
Plate No. 1										
1	0.439	1.04	266.7	1	3.27	144.4	1	3.27	79.5	1
2	0.204	0.31	416.9	2	0.98	219.5	-1	0.98	111.0	2
3	2.034	11.00	118.8	3	34.38	65.7	3	34.38	41.4	3
4	1.213	4.99	155.2	4	15.64	85.4	4	15.64	51.5	4
5	0.294	0.55	333.9	-1	1.75	178.9	-1	1.75	94.5	-1
6	1.531	7.13	141.5	5	22.31	79.4	5	22.31	46.7	5
7	0.888	3.09	191.5	6	9.70	106.9	6	9.70	58.8	6
Plate No. 2										
1	0.267	0.47	874.2	-1	1.50	425.6	-1	1.50	164.3	-1
2	0.083	0.07	2086.4	-1	0.23	852.1	-1	0.23	278.5	-1
3	2.744	17.34	229.4	2	54.18	124.2	2	54.18	60.4	2
4	1.104	4.32	376.4	1	13.54	198.7	1	13.54	88.9	1
5	0.392	0.87	709.8	-1	2.74	361.7	-1	2.74	138.9	-1
6	0.918	3.26	437.2	-1	10.21	233.6	-1	10.21	96.2	-1
Plate No. 3										
1	0.899	2.48	627.2	1	8.16	318.3	1	8.16	193.6	1
2	1.114	3.56	549.3	-1	11.65	282.1	-1	11.65	173.7	-1
Plate No. 4										
1	0.825	2.95	613.8	1	9.27	317.8	1	9.27	269.6	1
Plate No. 5										
1	0.810	2.87	646.1	1	9.02	333.7	1	9.02	332.7	1
Plate No. 6										
1	0.945	3.62	614.3	1	11.36	319.3	1	11.36	429.9	1
Plate No. 7										
1	0.674	2.18	758.6	-1	6.84	387.3	-1	6.84	575.3	-1

The number in the column Hole No. represent the hole number on the specified witness pack plate.

[†] Hole number indicates the number of the hole on the following witness pack plate to which the current hole is matched. A value of -1 signifies the matching process did not match the hole with any holes on the following plate.

Another item to note in reviewing the characterisation data is that DeCaM identifies fragments with characterised velocities greater than the projectile initial impact velocity as high velocity fragments. These "high velocity" fragments are ignored in the remainder of the debris cloud statistical characterisation. Therefore, an important implication of a fragment velocity overestimation is the possibility that BA-armour fragment information will be unnecessarily discarded. A preliminary review of DeCaM's velocity estimation ability is presented in Section 3.4.3.2, but for the time being it is noted that the higher velocity estimates associated with DeCaM 1.1 and 2.0 could reduce the accuracy of the characterisation. For example, witness pack plate hole number 2 in the DeCaM 2.0 characterisation results (Table 3.11) is identified as a "high velocity" fragment and thus left out of the hole matching process. This causes the second hole on the first plate, which is matched to the second hole on the second plate in the DeCaM 2.0T result, to be considered a final fragment hole.

Since the debris characterisation in both DeCaM 2.0 and DeCaM 2.0T were run to ensure that the total fragment mass equals the change in target mass by optimising the fragment shape factor value it would be expected that the fragment masses be very similar. The only difference in the two mass characterisation processes is that DeCaM 2.0 includes a hole growth routine to try and establish the difference between the witness pack plate hole area and the fragment presented area. The similarity of the results suggests that either hole growth is not a significant factor or that the hole growth routine is not adequate. The latter hypothesis is more likely.

Data supporting the DeCaM 2.0T characterisation process was developed for either V_{50} or V_{95} penetration velocity threshold curves. Table 3.12 compares the results of DeCaM characterisations based on V_{50} and V_{95} penetration threshold data for BA debris experiment 3527. The V_{50} characterisation results relate to velocities which have a 50% chance of penetrating the witness pack plate whereas the V_{95} results represent the velocities which have a 95% probability of penetrating the plate and would thus be greater for a given fragment mass. Unfortunately, the V_{50} characterisation results for given witness pack holes, in Table 3.12, do not consistently relate to lower estimated fragment velocities than those for the V_{95} results, as expected.

Table 3.12: Comparison of V_{50} and V_{95} Characterisation Results for Test 3527

WP Plate Hole No *	WP Hole Area [cm^2]	DeCaM 2.0 - V_{50} Velocity Threshold Curves			DeCaM 2.0 - V_{95} Velocity Threshold Curves		
		Mass [g]	Vel. [m/s]	Next Hole†	Mass [g]	Vel [m/s]	Next Hole†
Plate No. 1							
1	0.930	11.56	63.2	1	11.56	56.5	1
2	1.192	16.89	58.1	2	16.89	50.4	2
3	0.003	0.00	0.0	-1	0.00	0.0	-1
4	0.001	0.00	0.0	-1	0.00	0.0	-1
5	1.934	35.33	49.4	3	35.33	41.1	3
6	0.100	0.34	136.9	-1	0.34	148.3	-1
7	0.207	1.12	105.7	-1	1.12	107.1	-1
Plate No. 2							
1	1.156	16.12	85.3	1	16.12	87.7	1
2	2.219	43.54	65.6	2	43.54	64.2	2
3	1.736	29.97	72.4	3	29.97	71.2	3
Plate No. 3							
1	0.382	2.06	288.2	-1	2.06	294.9	-1
2	1.056	11.87	144.1	2	11.87	172.7	2
3	1.113	12.94	139.8	3	12.94	168.2	3
Plate No. 4							
1	0.053	0.16	1004.3	-1	0.16	995.3	-1
2	0.227	1.47	474.4	-1	1.47	485.7	-1
3	1.292	20.16	197.7	1	20.16	269.6	1
Plate No. 5							
1	1.679	29.85	201.2	1	29.85	213.4	1
Plate No. 6							
1	1.385	22.37	328.7	1	22.37	348.3	1
Plate No. 7							
1	1.777	32.50	367.1	-1	32.50	367.1	-1

The inconsistency in results is thought to be a product of the variability in the reported experimental data from which the threshold curves were generated. Figure 3.5, illustrates the areas and magnitudes of the inconsistencies between the penetration velocity threshold predictions of the V_{50} and V_{95} data. This figure plots the ratio of the predicted fragment velocity at each penetrated witness pack plate versus fragment mass for each plate hole. In this figure, all of the points would ideally have velocity ratios less than unity. It is noted that the inconsistencies are related to low velocity predictions. That is predictions made for high mass (low penetration velocity) on plates 1 and 2 seem to be problematic in the regressed threshold curves.

Large mass / low velocity and low mass / high velocity events are at the ends of the penetration velocity threshold curves where extrapolation of the data was required and therefore could be in error. In addition, the V_{50} and V_{95} threshold curves were developed independently and their results were not carefully compared to ensure consistency. It is felt that the threshold curves formulations could be reviewed to ensure more complete consistency between the V_{50} and V_{95} characterisation results. If time allowed it would be interesting to review the raw experimental data to develop a better statistical understanding of the experimental variability and thus better describe the witness pack plate minimum penetration velocities.

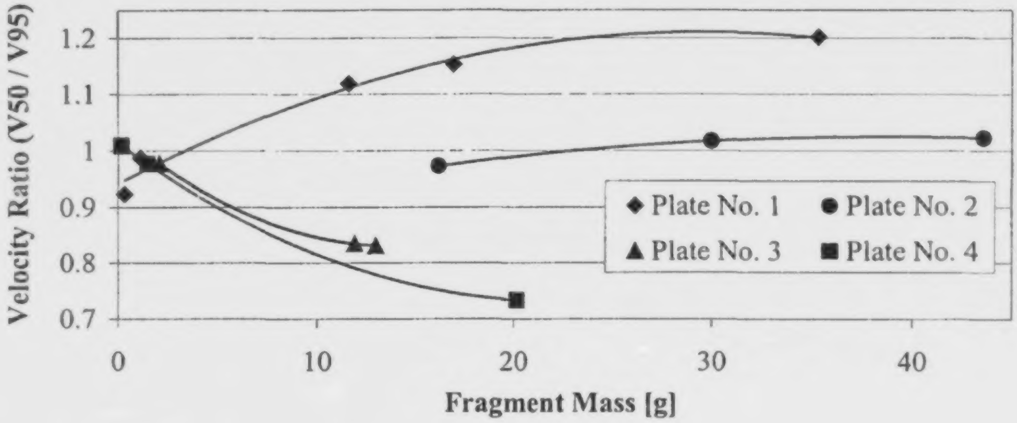

Figure 3.5: V_{50} and V_{95} Penetration Velocity Threshold Estimation Inconsistencies

3.4.3.2 Comparison of Estimated and Observed Velocities

In reviewing the characterisation results, the fragment and residual projectile velocities have been compared to experimental results. Table 3.13, compares the characterised fragment velocities to experimentally reported fragment velocities. The experimental results for tests 3529 and 3530 report fragment velocities of 231.3 and 222.5, respectively. It is unclear if these are the velocities of single fragments or average fragment cloud velocities, but they are compared to the characterisation results in terms of the average fragment velocities. Table 3.13 reports the velocity of each fragment as estimated at the last plate it penetrated. The calculated average fragment velocity only includes those fragment velocities below the penetrator impact velocity. Based on these assumptions and the limited amount of data, it is suggested that the threshold curves seem to provide the best estimate of BA debris fragment velocities.

Table 3.13: Comparison of Estimated and Observed Fragment Velocities

Test 3529	DeCaM 1.1	DeCaM 2.0	DeCaM 2.0 (Threshold)
Fragment Velocities [m/s]		2672.3, 2952.1 674.0, 380.8, 339.5	457.3, 501.2, 171.3 231.7, 243.9
# Good Fragments		3	5
Average Velocity [m/s]		464.8	321.1
Obs. Frag. Vel. [m/s]	231.3	231.3	231.3
Est. /Obs. Velocity		2.01	1.39
Test 3530	DeCaM 1.1	DeCaM 2.0	DeCaM 2.0 (Threshold)
Fragment Velocities [m/s]	8914.7, 1193.5 484.9, 624.0	450.4, 280.3, 34868 364.1, 632.7, 2773.4	128.6, 88.48, 1864.0 262.0, 187.3, 468.3
# Good Fragments	2	4	5
Average Velocity [m/s]	554.5	431.9	226.9
Obs. Frag. Vel. [m/s]	222.5	222.5	222.5
Est. /Obs. Velocity	2.49	1.94	1.02

By assuming that the largest hole in the last penetrated plate represents the residual penetrator, Table 3.14 compares the experimentally observed residual projectile velocities to those characterised by DeCaM and that calculated by MPPM3.

Table 3.14: Comparison of Estimated and Observed Residual Projectile Velocities [m/s]

Test	Observed	DeCaM 1.1	DeCaM 2.0	DeCaM 2.0T	MPPM3
3527	557.9	437.0	294.1	367.1	558.8
3528	514.6	455.5	229.6	378.6	566.1
3529	553.1		339.5	243.9	509.1
3530	505.2	624.0	364.1	262.0	499.0
3531	345.9	555.9	366 8	202.8	255.2
3532	303.1	481.2	202.9	152.3	441.1
3533	327.0	607.2	756.9	282.6	253.3
3534	460.5	1832.0	1127.6	573.5	400.2
3535	465.6	418.1	342.3	239.3	402.0
3536	446.0	758.6	387.3	575.3	392.4

In an effort to better understand this projectile residual velocity data, Figure 3.6 was generated to compare the estimated to observed velocities for each measured or observed velocity. A perfect prediction of the measured residual penetrator velocity would be shown in Figure 3.6 as a horizontal line at a value of unity. The results for MPPM3 most closely approaches the ideal. The results for DeCaM 2.0 and DeCaM 2.0T are similar in their accuracy yet DeCaM 2.0 seems to overestimate fragment velocities whereas DeCaM 2.0T seems to underestimate residual penetrator velocities. Both DeCaM 2.0 and DeCaM 2.0T estimate higher velocities for residual penetrators with medium residual velocities, this could be a coincidence related to projectile yaw when penetrating the witness pack which would effect mass and thus minimum penetration velocity estimates.

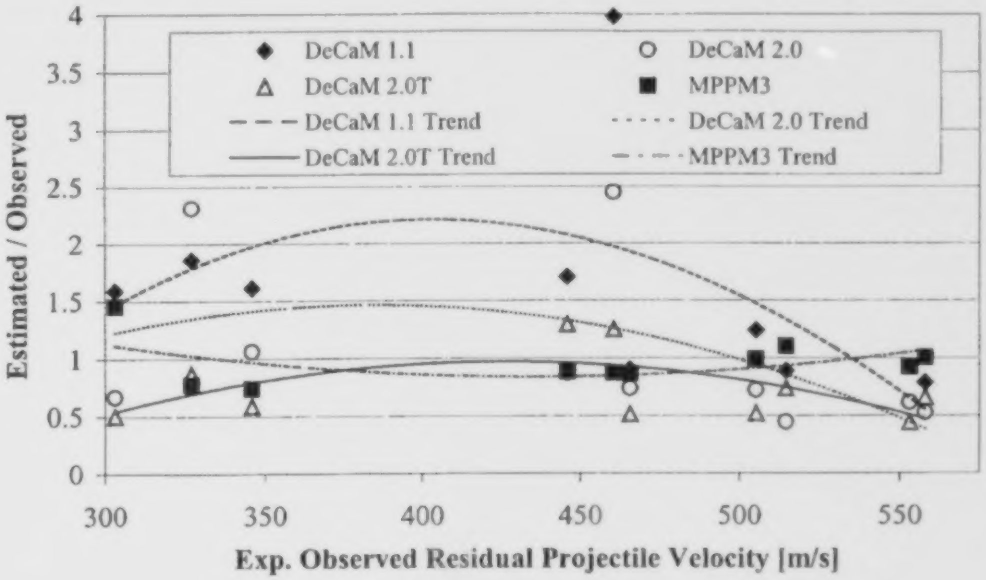

Figure 3.6: Residual Projectile Velocity Error Ranges

3.4.3.3 Comparison of Estimated and Observed Masses

The results of the fragment and projectile mass characterisation are reviewed here against common sense and the predictions of MPPM3. Table 3.15 tabulates the estimated shape factors which were used to relate total fragment mass to the change in target mass in the characterisation of the each experimental test results. The target shape factors which include information on both material density and fragment geometry have been related to cylindrical fragment length to diameter (L/D) ratios for ease of interpretation. The given relation between shape factors and L/D ratios are valid for fragment diameters ranging from 1 to 20 mm. The results in Table 3.15 indicate that for the most part the DeCaM 2.0 and DeCaM 2.0T characterisations independently arrive at the same shape factor. Shape factor differences occur when "high velocity" fragments have been eliminated from the DeCaM 2.0 data set and not DeCaM 2.0T.

Table 3.15: Comparison of Fragment Geometry

	DeCaM 2 0		DeCaM 2.0T	
Test	Shape Factor [$m^2/kg^{2/3}$]	L/D Ratio	Shape Factor [$m^2/kg^{2/3}$]	L/D Ratio
3527	0.0026250	0.84	0.0018750	1.39
3528	0.0015000	1.94	0.0015000	1.94
3529	0.0060000	0.24	0.0060000	0.24
3530	0.0052500	0.30	0.0052500	0.30
3531	0.0036250	0.52	0.0032500	0.61
3532	0.0010000	3.57	0.0010000	3.57
3533	0.0050000	0.32	0.0021250	1.15
3534	0.0050000	0.32	0.0035000	0.55
3535	0.0045000	0.37	0.0045000	0.37
3536	0.0018125	1.46	0.0018125	1.46

The L/D ratios assigned to the fragments are "reasonable" in that they do not require the ratio of the fragment dimensions to be more than four to one. Ideally the characterisation process would assign individual fragment shape factors instead of a single shape factor to the entire debris cloud. These individual shape factors could be assigned based on a relationship with fragment mass or velocity.

The residual mass of the projectile based on the DeCaM characterisation process is compared to that predicted by MPPM3 in Table 3.16. The results are the same for DeCaM 2.0 and DeCaM 2.0T which is due to their common estimated shape factor value (see Table 3.15). While the MPPM3 estimated residual penetrator mass does not vary significantly between test results, the characterised residual penetrator mass varies over a wide range, but is generally below that estimated by MPPM3.

Table 3.16: Comparison of MPPM3 Residual Projectile Mass

	Projectile Residual Mass [g]			
Test No.	MPPM3	DeCaM 1.1	DeCaM 2.0	DeCaM 2.0T
3527	26.00	9.37	19.01	32.50
3528	26.00	8.41	29.19	29.19
3529	26.00		20.79	20.79
3530	25.75	7.52	17.13	17.14
3531	25.69	4.25	8.36	7.01
3532	26.00	3.55	17.88	17.88
3533	25.69	2.81	2.00	8.00
3534	25.72	0.37	0.66	0.88
3535	25.72	9.61	13.45	13.45
3536	25.72	2.18	6.84	6.84

3.5 Characterisation Process Status

The characterisation process review and validation based on a comparison with experimental data suggests that the DeCaM 2.0 characterisation process is soundly grounded on scientific / engineering theory and agrees well with observed trends. Additional effort should however be spent in improving the witness pack penetration threshold curves and in the revision of the witness pack hole growth relationships.

4.0 MODELLING PROCESS

4.1 Modelling Process Introduction

4.1.1 Modelling Process Overview

The modelling process included in DeCaM includes seven steps as shown in Figure 4.1. In the first step of the process the user may direct DeCaM to produce a deterministic or a probabilistic modelling result. The deterministic result only develops a single debris cloud description based on a random estimate of the number of debris cloud fragments. A probabilistic modelling result is essentially a statistical summary of many deterministic modelling results. The number of deterministic model results used to develop the probabilistic result is either specified by the user or determined in the process of developing a result to a specified level of accuracy.

The residual penetrator velocity may be specified by the user as a fraction of the impact velocity or may be calculated based on MPPM3 results as shown in steps 2a and b of Figure 4.1. This option is included in order to allow the user to:

- avoid supplying the significant amount of data required by MPPM3,
- use experimentally measured residual penetrator velocities, and
- develop upper and lower bound BA-debris simulation results by maximising the available fragmentation energy (high residual penetrator velocities will maximise energy available for the fragmentation process).

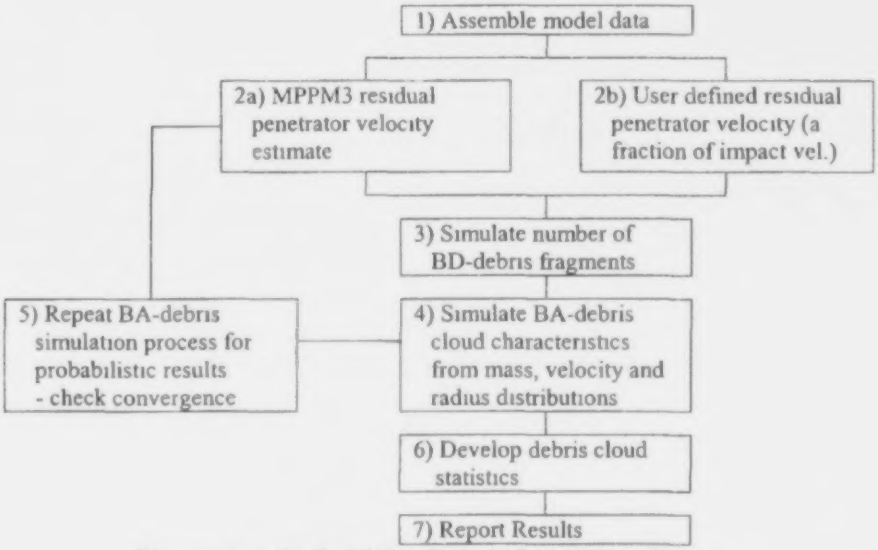
1) Assemble model data
2a) MPPM3 residual penetrator velocity estimate
2b) User defined residual penetrator velocity (a fraction of impact vel.)
3) Simulate number of BD-debris fragments
5) Repeat BA-debris simulation process for probabilistic results - check convergence
4) Simulate BA-debris cloud characteristics from mass, velocity and radius distributions
6) Develop debris cloud statistics
7) Report Results

Figure 4.1: DeCaM BA Debris Modelling Process

4.1.2 Scope of Modelling Process Improvements

In general, the improvements of the modelling process have focussed on the target penetration mechanism and its subsequent effects on the fragmentation process. The specific areas which were investigated include:

- consideration of MPPM3 data
- target penetration hole geometry
- energy expended in target deformation in the penetration process
- updating the target fragmentation model

After the implementation of the ballistic penetration model modifications, it was necessary to recalibrate and validate the fragmentation model based on WP test data. The sections which follow describe the development processes and the work done in the calibration and validation processes.

4.2 Target Penetration Model Improvements

4.2.1 Target Penetration and Fragmentation Process Introduction

In this portion of the project penetrated target plates were examined to improve the armour fragmentation model by:

1) relating the target hole conical frustum geometry to the ballistic impact conditions and shot conditions (projectile, target and impact characteristics), and
2) assessing target deformation energy consumption.

A relationship between the ballistic impact conditions including target configuration and the expected number of target fragments generated in a penetration event was developed previously. This penetration process energy balance is based on an assumed affected target area (volume). A conical frustum is defined as the source of all behind-armour debris fragments and the energy balance formulation indicates how much fragmentation energy is available.

4.2.2 Target Penetration Experimental Data

The penetration zones in six steel plates used in fifteen BA-debris tests were examined in this investigation. The ballistic testing was completed at the Defence Research Establishment Valcartier (DREV). The test conditions associated with each penetration event (BA-debris test) are described in Table 4.1. Unfortunately only one oblique impact result is available for examination therefore the results of this investigation will be confined to normal impact penetration events.

Table 4.1: Target Penetration Experimental Data

Test	Threat**		Target			V_{50}	Velocity				Target weight	
ID	Calibre	Type	Type	Thick.	Obliq		Impact		Res. core	BA debris	before	after
	[inch]			[mm]	[deg]	[m/s]	[V_i / V_{50}]	[m/s]	[m/s]	[m/s]	[g]	[g]
1198	0.5	M2 ball	RHA	6.5	0	363	2.41	875	814	680	n/a	n/a
1201							2.38	864	811	717	n/a	n/a
1265							1.49	539	404	none	2330	2325
1266							n/a	600*	n/a	n/a	n/a	n/a
1267							1.91	692	586	n/a	2323	2322
1206				10	0	485	1.77	858	n/a	450	3804	3784
1207							1.79	869	n/a	436	3784	3765
1208							n/a	n/a	n/a	n/a	n/a	n/a
1271							1.51	731	n/a	n/a	3660	3656
1272							n/a	800*	530	n/a	3656	3655
1274							1.75	847	723	520	3655	3636
1213				14.5	0	601	1.47	881	665	544	5018	4981
1214							1.44	867	662	321	4981	4944
1215							n/a	n/a	n/a	n/a	n/a	n/a
1340					15	524	1.32	689	304	n/a	5069	5055

*Assumed impact velocity

**Projectile mass assumed to be 25.5 g (0.50 cal ball M33 - core mass = 25.3g)

4.2.3 Review of Target Penetration Holes

The penetration events include both petalling and plugging mechanisms. This observation is based on the remaining geometry of the target plates. Visually one can discern a penetration mechanism progression from petalling to plugging. Figure 4.2 pictorially illustrates this progression by showing several target penetrations. Hole type A is representative of a typical petalling penetration and hole type C is typical for plug type penetration. The penetration producing hole type B is considered to be in a transition form a petalling process to a plugging process since a shear ring is formed. It is suggested that this shear ring produces the annular disk fragments observed in experimental penetration processes.

Measurements of the penetrated plate deformed geometries are shown in Table 4.3 and these geometric measures are defined in Figure 4.3. A comparison of the measured data with the shot conditions (see Table 4.1) suggests that:

- the size of the penetration hole is directly related to the impact velocity,
- the size of the deformation zone is inversely related to the impact velocity, and
- the penetration cone angle is directly related to the penetration velocity.

Table 4.2 also relates each penetration event to a mechanism type (A, B or C) as characterised in Figure 4.2.

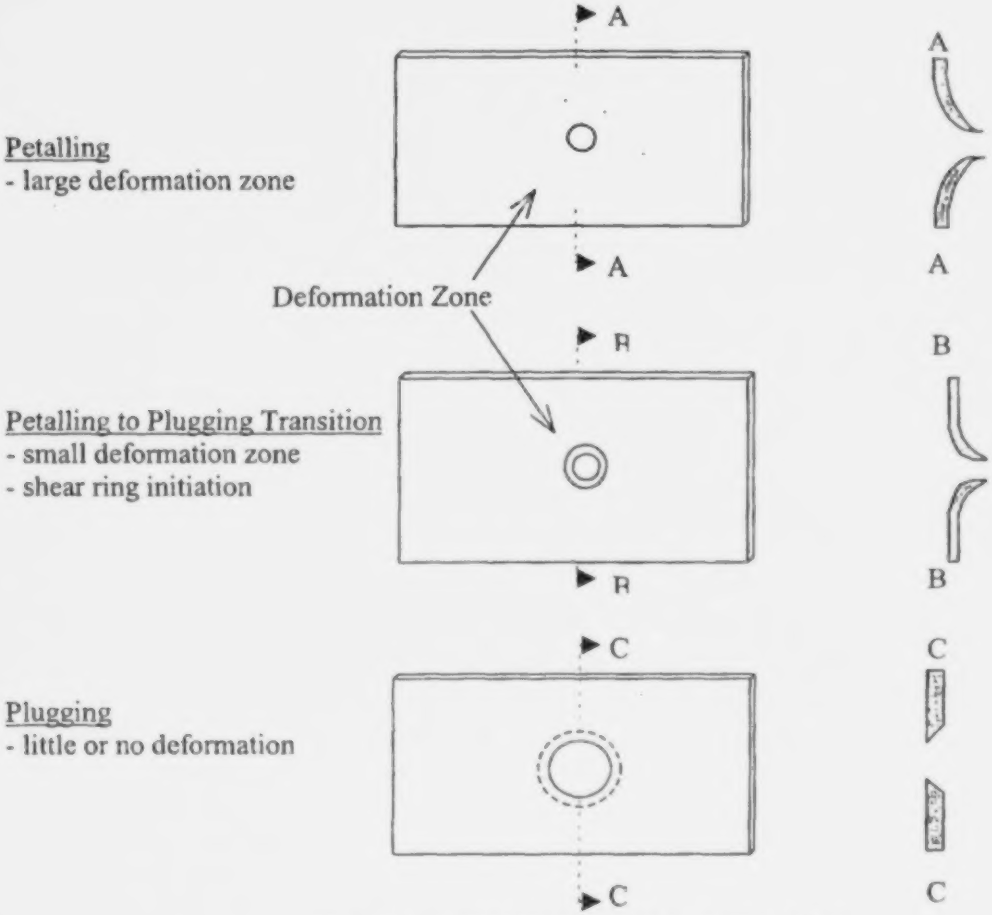

Figure 4.2: Petalling and Plug Penetration

Table 4.2: Penetration Zone Geometry

Test	Plate	Overmatch	Hole Dia.		Def. Zone Dia.		Def Zone	Cone	Penetration
ID	Thick.	V_i/V_{50}	Front	Back	Front	Back	Depth[*]	Angle	Mech.[†]
	[mm]		[mm]	[mm]	[mm]	[mm]	[mm]	[deg.][‡]	
1198	6.5	2.41	14.0	15.5	19	26	0	6.3	C
1201	6.5	2.38	13.3	15.2	19	23	0	8.2	C
1265	6.5	1.49	10.5	10.5	58	60	6.5	0.0	A
1266	6.5	1.65[¥]	14.7	14.7	60	60	9.0	0.0	A
1267	6.5	1.91	15.6	15.6	63	63	13.3	0.0	A
1206	10	1.77	15.5	19.6	22	36	0	11.6	C
1207	10	1.79	15.9	20.5	22	36	0	13.2	C
1208	10	1.65[¥]	15.4	20.9	23	32	0	15.4	C
1271	10	1.51	10.8	10.8	46	46	3.2	0.0	B
1272	10	1.65[¥]	10.7	10.7	45	46	3.2	0.0	B
1274	10	1.75	15.2	21.2	22	36	0	16.7	C
1213	14.5	1.47	16.0	24.9	31	37	0	17.0	C
1214	14.5	1.44	15.8	25.8	31	40	0	19.1	C
1215	14.5	1.65[¥]	16.0	25.7	31	42	0	18.5	C
1340	14.5	1.32	10.1	10.1	29	36	0	0.0	C

[*] Maximum depth

[†] Penetration mechanism as per Figure 1

[‡] Calculated value

[¥] Based on assumed impact velocity

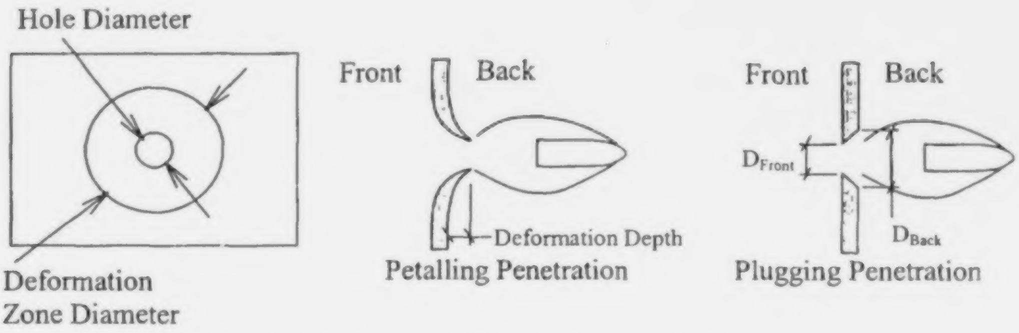

Figure 4.3: Penetrated Plate Geometric Measures

4.2.3 Development of Target Penetration Cone Relations

From the experimental data, relationships between penetration hole diameter and impact velocity overmatch were developed. These relationships are shown in Figure 4.4, in which the entry and exit diameter symbols plot measured values and the cone angle symbols represent calculated values. The target penetration cone angle is calculated from the entry and exit diameters, for a normal impact scenario, as follows:

$$\text{Cone Angle } (\phi) = \text{Tan}^{-1}\left(\frac{D_{Exit} - D_{Entry}}{2t}\right)$$

where t is the target plate thickness.

It was found that a second order polynomial provided an appropriate regression fit between impact velocity over match and the penetration hole geometry. While regression equations have been developed for all three geometric parameters (entry diameter, exit diameter and conical hole angle), values for any two of the parameters completely define the penetration cone geometry.

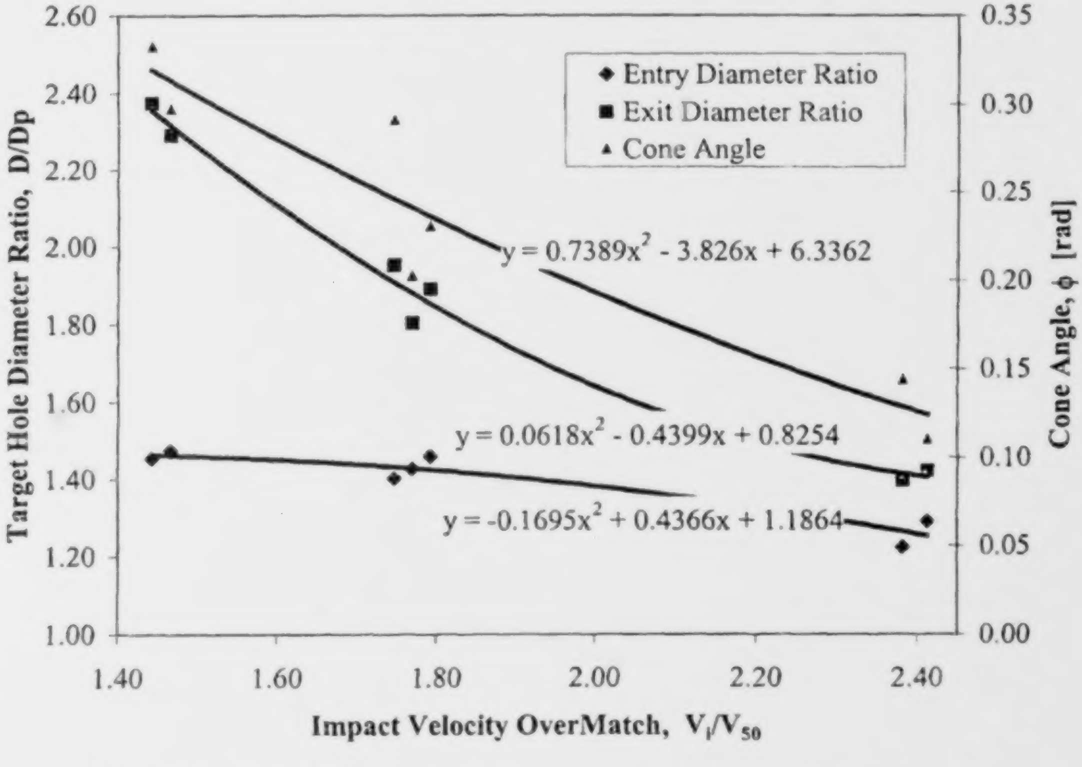

Figure 4.4: Target Penetration Cone Geometry to Impact Velocity Relations

4.2.4 Estimation of Target Deformation Energy

The current target penetration energy balance does not explicitly include target deformation as an energy sink since preliminary analyses indicated that it did not consume a significant amount of energy. The following investigation reviews this assumption based on experimental data. The investigation recognises the difference between the two distinct penetration mechanisms (i.e. petalling and plugging) by developing target penetration zone deformation definition relations separately for the two penetration processes.

The target deformation energy was estimated for the plates which displayed measurable deformation (see Table 4.2). Eleven radial distances from the centre of the target penetration hole were defined at which the displacement of the target surface was measured. This deformation data was used to estimate the plastic deformation work in terms of the target plate thickness (t), plate perfectly plastic moment (M_{pi}), change in rotation within an interval ($\Delta\theta_i$), the deformation zone interval radius (r_i) and yield strength (σ_y) of the steel as follows:

$$\text{Deformation Work} = \sum_{i=1}^{\#\,\text{intervals}} \Delta\theta_i M_{pi} = \sum_{i=1}^{\#\,\text{intervals}} \frac{1}{2}\Delta\theta_i \pi r_i \sigma_y t^2$$

The plastic deformation energy (E_p) is calculated and expressed as a fraction of the impact energy (E_i) in Table 4.3. Only 5 of the 15 target holes examined are petalling penetrations, "A or B" type as shown in Figure 4.2 (i.e. display significant deformation zone depth). The available data includes two target plate thickness and five impact velocity matching ratios.

Table 4.3: Percentage of Plastic Energy to Impact Energy

Test ID	V_i [m/s]	Diameter$^+$ [mm]	Depth$^+$ [mm]	E_p [J]	E_i [J]	E_p/E_i
1265	539	58	6.5	82.3	3704.1	0.022
1266	600*	60	9.03	198.1	4590.0	0.043
1267	692	63	13.3	447.0	6105.5	0.073
1271	731	46	3.2	268.9	6813.1	0.039
1272	800*	45	3.2		8160.0	

* Assumed impact velocity

$^+$ Diameter and depth of deformation zone as shown in Figure 4 3

The data in Tables 4.3 and 4.1 may be plotted to identify target deformation trends with impact velocity and target parameters. These relationships are plotted in Figures 4.4, 4.5 and 4.6 for petalling types A and B and plugging Type C penetration mechanisms, respectively.

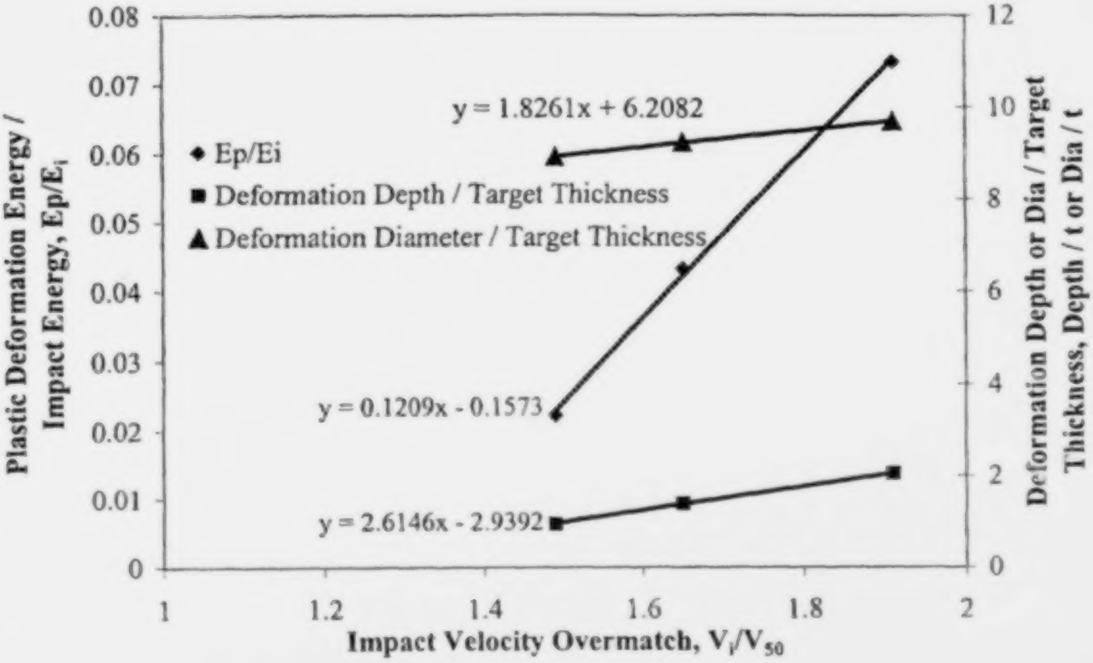

Figure 4.4: Target Deformation Trends for Type A Petalling Penetration

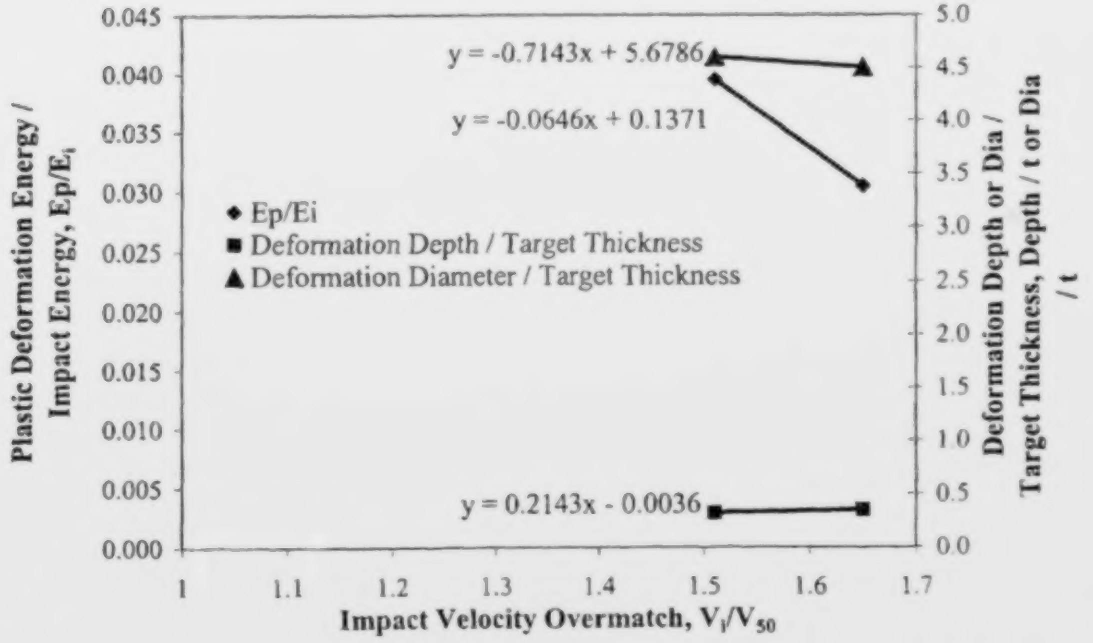

Figure 4.5: Target Deformation Trends for Type B Petalling Penetration

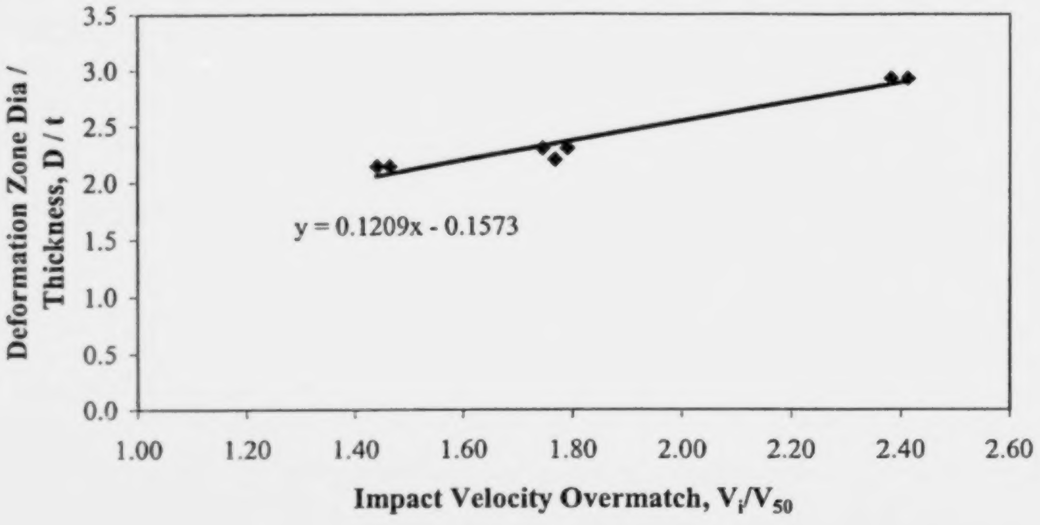

Figure 4.6: Target Deformation Trends for Type C Plugging Penetration

A general trend which is drawn from the data review is that at projectile impact velocities below the plugging penetration mechanism threshold, the target plastic deformation energy increases with impact velocity until sufficient energy is delivered to the target to form a shear ring. With the development of a shear ring the deformation energy declines. This trend is shown pictorially in Figure 6 and is consistent with strain rate material embrittlement (i.e. a decrease in material ductility with increasing loading rate). It should however be noted that the target deformation trends observed in this investigation are based on a small data set and should be verified with additional information.

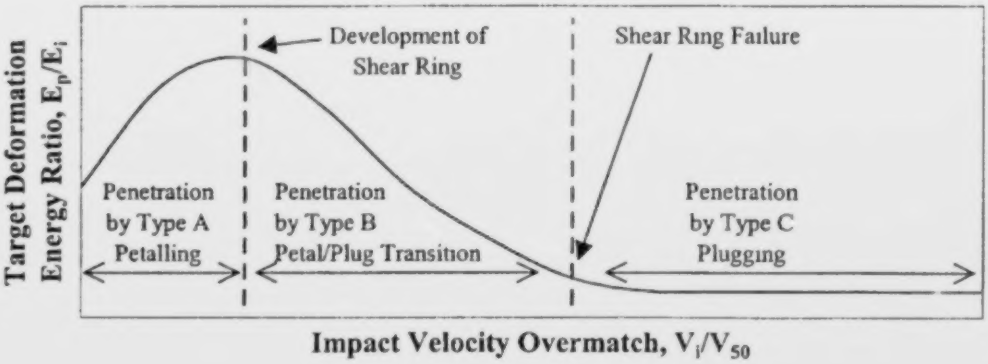
Target Deformation Energy Ratio, E_p/E_i
Development of Shear Ring
Shear Ring Failure
Penetration by Type A Petalling
Penetration by Type B Petal/Plug Transition
Penetration by Type C Plugging
Impact Velocity Overmatch, V_i/V_50

Figure 4.7: Idealised Deformation Energy to Impact Velocity Relationship

4.2.5 Fragmentation Model Target Penetration Improvements

The results of the target penetration reviews provide information which may be used in further developing the target fragmentation model. While all of the results developed in the previous sections are of interest, only the target hole geometry to impact velocity relationship will be implemented at this time. While the target hole geometry relationship is based only on normal impact experimental data, it will be implemented in the fragmentation model which considers both normal and oblique impacts. The remainder of this section describes the fragmentation model including the modifications developed in this investigation.

As before, a target hole produced by an oblique ballistic penetration is characterised as a frustum of a skewed elliptical cone as shown in Figure 4.8. The major (b_1 and b_2) and minor (a_1 and a_2) axis radii of the entry and exit surfaces and cone surface area (A_{cone}) are functions of the projectile diameter (D_p), impact velocity overmatch, the target obliquity angle (θ), and cone angle (ϕ).

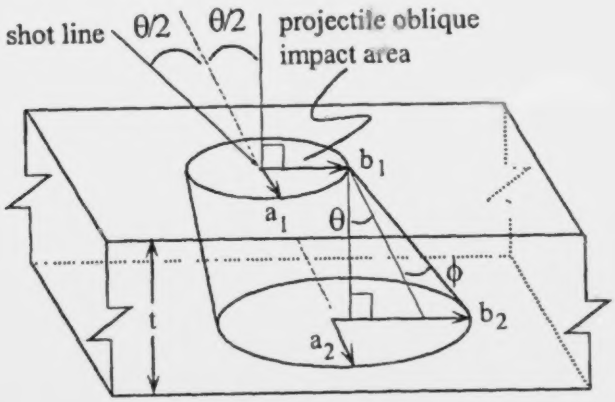

Figure 4.8: Target Plug Fragmentation Zone

Where

$$a_1 = \frac{D_p}{2}\frac{D_1}{D_p} = \frac{D_1}{2}$$

$$b_1 = \frac{a_1}{Cos2\theta} = \frac{D_1}{2Cos2\theta}$$

$$a_2 = a_1 + tTan\phi = \frac{D_2}{2}$$

$$b_2 = \frac{D_1}{2Cos2\theta} + \frac{t}{2}\left(Tan(\phi-\theta) + Tan(\phi+\theta)\right)$$

$$A_{cone} = \pi t\sqrt{2\left[\left(\frac{a_1+a_2}{2}\right)^2 + \left(\frac{b_1+b_2}{2}\right)^2\right]}$$

$$= \pi t\sqrt{2\left[\left(\frac{D_1+D_2}{4}\right)^2 + \left(\frac{2D_1/(Cos2\theta)+t\left(Tan(\phi-\theta)+Tan(\phi+\theta)\right)}{4}\right)^2\right]}$$

The target plate penetration hole investigation provides the following relationships for the cone side slope (ϕ), entry (D_1) and exit (D_2) hole diameters in terms of the impact velocity overmatch ratio ($R = V_i / V_{50}$) and projectile diameter (D_p):

$$D_1 = (-0.145\,R^2 + 0.374\,R + 1.015) * D_p$$

$$D_2 = (0.0618\,R^2 - 0.4399\,R + 0.8254) * D_p$$

$$\phi = \mathrm{Tan}^{-1}\left(\frac{D_2 - D_1}{2t}\right)$$

By assuming the target hole geometry described above, the crack growth area (A_c) produced by the fracture energy can be estimated based on the fragment surface areas as follows:

$$A_c = \frac{NA_s}{2} - A_1 - A_2 + \pi\, t\sqrt{2\left[(\bar{a})^2 + (\bar{b})^2\right]}$$

A_c	crack surface area
N	number of debris fragments
A_s	average fragment surface area
$A_{1,2}$	entry / exit ellipse area = $\pi\, a_i b_i$
$\bar{a}, \bar{b}$	average ellipse axis = $(a_1 + a_2)/2$

$$A_c = \frac{NA_s}{2} - A_1 - A_2 + \pi t\sqrt{2\left[(\bar{a})^2 + (\bar{b})^2\right]} = \frac{NA_s}{2} - \pi a_1 b_1 - \pi a_2 b_2 + \pi t\sqrt{2\left[(\bar{a})^2 + (\bar{b})^2\right]}$$

$$= \frac{NA_s}{2} - \pi\frac{D_1{}^2}{4\mathrm{Cos}2\theta} - \pi D_2\left(\frac{D_1}{2\mathrm{Cos}2\theta} + \frac{t}{2}\left(\mathrm{Tan}(\phi - \theta) + \mathrm{Tan}(\phi + \theta)\right)\right) + \pi t$$

$$\sqrt{2\left[\left(\frac{D_1 + D_2}{4}\right)^2 + \left(\frac{2D_1/(\mathrm{Cos}2\theta) + t\left(\mathrm{Tan}(\phi - \theta) + \mathrm{Tan}(\phi + \theta)\right)}{4}\right)^2\right]}$$

The behind-armour debris fragments are characterised as cylindrical elements, with diameters (D_f) and a specified length to diameter ratio (Φ). Using this information their surface area (A_s) can be determined in terms of their mass (m_f) and presented area to mass ratio (k) as follows:

$$A_s = \Phi\pi D_f{}^2 + \frac{\pi D_f{}^2}{2} \qquad \text{where} \qquad D_f = \sqrt{\frac{4k}{\pi} m_f{}^{2/3}} \qquad \text{and} \qquad k = \frac{\pi^{1/3}}{(\Phi\rho)^{2/3}}$$

then

$$A_s = \frac{2\pi^{1/3} m_f{}^{2/3}(2\Phi + 1)}{(\Phi\rho)^{2/3}}$$

An equation which relates the expected number of fragments (N) to the fracture energy in the target plate is found by substituting the equations above into the fracture area (A_c) equation and solving for N:

$$N = \frac{(\Phi\rho)^{2/3}\left[(E_f / G) - A_{cone} + \pi(a_1 b_1 + a_2 b_2)\right]}{\pi^{1/3} m_f{}^{2/3}(2\Phi + 1)}$$

A further substitution allows the expression of the number of fragments in terms of the fragmentation energy components as follows:

$$N = \frac{(\Phi\rho)^{2/3}\left[\left(\left(E_i - E_d - E_p - E_l\right)/G\right) - A_{cone} + \pi\left(a_1 b_1 + a_2 b_2\right)\right]}{\pi^{1/3} m_f^{2/3}(2\Phi + 1)}$$

And expanding this expression based on the energy component definitions results in:

$$N = (\Phi\rho)^{2/3}\left[\frac{Em_p V_i^2 - 2A_{cone}K^2 - 2EE_p - m_p V_{pres}^2 + 2\pi K^2\left(a_1 b_1 + a_2 b_2\right)}{\left(4\pi^{1/3}K^2\Phi + 2\pi^{1/3}K^2 + m_f^{1/3}(\Phi\rho)^{2/3}EV_f^2\right)m_f^{2/3}}\right]$$

This equation can be used to predict a characteristic (mean) value of the number of debris fragments developed in a ballistic projectile penetration based on a first order Taylor series expansion of the independent variables about their mean values. The expression for the mean number of fragments produced in a ballistic penetration is evaluated for the mean values of each of the independent random variables (material toughness (K), fragment geometry (Φ), fragment mass (m_f) and fragment velocity (v_f)).

4.3 Fragmentation Model Calibration and Validation

4.3.1 Fragmentation Model Calibration and Validation Introduction

The target fragmentation process, which produces the observed BA debris, is idealised in DeCaM by conserving the initial impact energy, as described in the previous section. The impact energy is assumed to be balanced in part by the energy required to generate BA debris fragments through a process described by linear elastic fracture mechanics. It is recognised that this formulation is an idealisation of the ballistic penetration target fragmentation process and requires calibration:

- to better represent experimental observations of the typical number of fragments, and
- to incorporate the fragmentation process uncertainty and predict the distribution of results.

This calibration work is handled in two steps relating to the definition of a fragmentation trend or mean value correction constant followed by a calibration process to define the uncertainty associated with the fragmentation process based on a Weibull distribution calibration constant.

The objective of this section is to present the results of the re-calibration and validation of the improved behind-armour (BA) debris fragmentation model. This model is used in DeCaM 2.0 to estimate the number of BA debris fragments generated in a ballistic penetration event. The calibration of this model involves the selection of appropriate factors used to relate the analytic fragmentation model to experimental data in both a deterministic and probabilistic sense. The experimental data used in the calibration are taken from characterised witness pack data from a Defence Research Establishment Valcartier (DREV) experimental programme.

Predictions of the number of BA debris fragments generated in the ballistic penetration event are made in the DeCaM software in both the characterisation and modelling processes. The difference between the two results lies in their uncertainty. The fragmentation model results presented by the characterisation process are deterministic values based on the mean values of the uncertain or random variables (i.e. fragment mass and velocity). The results of the fragmentation model provided by DeCaM's BA debris modelling process are presented as either discrete random outcomes or statistical descriptions of the potential outcomes of the ballistic penetration event. The discrete and distributed BA debris descriptions are developed by the deterministic or probabilistic modelling capabilities of DeCaM, respectively. Details concerning the formulation of the fragmentation model were provided in the previous section and result in the following.

$$N = (\Phi\rho)^{2/3}\left[\frac{Em_pV_i^2 - 2A_{cone}K^2 - 2EE_p - m_pV_{pres}^2 + 2\pi K^2(a_1b_1 + a_2b_2)}{\left(4\pi^{1/3}K^2\Phi + 2\pi^{1/3}K^2 + m_f^{1/3}(\Phi\rho)^{2/3}EV_f^2\right)m_f^{2/3}}\right]$$

This equation may be used to predict a characteristic (mean) value of the number of debris fragments developed in a ballistic projectile penetration based on a first order Taylor series expansion of the independent variables about their mean values. The expression for the mean number of fragments produced in a ballistic penetration is evaluated for the mean values of each of the independent random variables (material toughness (K), fragment geometry (Φ), fragment mass (m_f) and fragment velocity (v_f)).

4.3.2 Fragmentation Model Uncertainty

The Weibull distribution when applied in the field of fragmentation ballistics has become known as the Mott distribution, since Mott (1947) introduced its use. Various studies have demonstrated the Weibull distribution can provide a good description of the variability in the number, mass or density of debris fragments. The Weibull probability density and cumulative distribution functions are expressed as follows:

Probability Density Function (PDF) $$f(x) = \frac{\beta}{\alpha}\left(\frac{x}{\alpha}\right)^{\beta-1}\exp\left[-\left(\frac{x}{\alpha}\right)^{\beta}\right]$$

Cumulative Distribution Function (CDF) $$F(x) = 1 - \exp\left[-\left(\frac{x}{\alpha}\right)^{\beta}\right]$$

Experimentally observed numbers of behind-armour debris fragments, generated in a ballistic penetration process, are used to validate the formulation of the mean number of debris fragments and calibrate the predicted variability of the fragmentation process. In a review of the difference between the predicted (mean) and characterised number of fragments it is possible to identify a consistent percentage error. This systematic difference between the observed and predicted number of fragments has been termed the modelling error (Δ). The deviation about the mean value may be described in terms of a confidence interval which contains a given percentage (λ) of the observed distributed data. The calibration process would identify the most appropriate modelling error value (Δ) and level of confidence (λ).

With this information it is possible to relate the mean number of fragments to the 50th percentile and derive the statistical parameters of the Weibull distribution describing the number of fragments generated in ballistic penetration event:

$$\beta = \frac{\ln[-\ln(0.5)] - \ln[-\ln(1-\lambda)]}{\ln[1/(1+\Delta)]} \quad \text{and} \quad \alpha = \frac{N}{[-\ln(0.5)]^{1/\beta}}$$

4.3.2 Calibration and Validation BA Debris Witness Pack Data

In the calibration and validation of the BA debris target fragmentation model independent data sources are used for the calibration (RD series experimental data) and subsequent validation (3500 series experimental data) process. The sections which follow describe this experimental data.

4.3.2.1 Experimental Calibration Data

The RD series experiments are characterised in this report as the basis of calibration of the fragmentation model. The data set includes 27 BA-debris tests identified as Test RD-1 to RD-67. The projectile, target plate and witness pack data used by the DeCaM software to describe the BA debris experiments for the fragmentation model, are listed in Table 4.4. These tests included both 25 and 35mm calibre projectiles at various impact velocities against various targets.

Table 4.4: Calibration Data Used in DeCaM BA Debris Characterisation Process

Parameter	Value	Parameter	Value
Witness Pack Angle [deg]	*	Location of impact point [cm]	X: 60.00 Y: 60.00 Z: -70.00
Witness pack plate spacing [cm]	2.54	Projectile mass [g]	*
Z reference [cm]	70.0	Impact velocity [m/s]	*
Target thickness [mm]	*	Projectile base diameter [mm]	*
Target density [kg/m^3]	7850	Imaging resolution [cm^2]	0.006
Young's Modulus [GPa]	207	Minimum allowed mass [g]	0.000
Target yield strength [MPa]	900	Matching area ratio	4.0
Fracture toughness [MPa m$^{1/2}$]	100.0	Matching radius multiplier	1.5
Minimum fragment size [cm^2]	0.000	Matching minimum distance [cm]	0.5
Target obliquity [deg]	*	Projectile X window offset [cm]	5.0
Fragment shape factor [m^2/kg$^{2/3}$]	**	Projectile Y window offset [cm]	5.0
Target hole side slope [deg]	30	Number of projectile fragments	1
Target mass before test [g]	*	Plate data file type	*
Target mass after test [g]	*	Number of plates	*

* Unique to each test (See Table 2)   ** Calculated in the characterisation process

Experimental conditions unique to each test and experimental measurements are listed in Table 4.5. The final target mass was set to zero and the change in target mass was used as the initial mass in the DeCaM characterisation process.

Table 4.5: Experimental Calibration Data and Measurements Unique to Each Test

Test ID	Change in Target Mass[g]*	Impact Velocity, V_i [m/s]	Velocity Overmatch V_i / V_{50}	Target Thickness [cm]	Obliquity Angle [deg]	Projectile Mass [g]	Projectile Base Dia [mm]	No. of Plates in Target
RD-1	166.3	1072.0	1.23	4.44	57	101.4	13.47	2
RD-10	180.4	1001	1.15	4.44	57	101.4	13.47	2
RD-14	253.6	1180.0	1.01	5.40	57	101.4	13.47	2
RD-17	245.8	942.1	1.04	5.40	35	101.4	13.47	2
RD-2	189.9	961.0	1.10	4.44	57	101.4	13.47	2
RD-21	258.9	904.0	0.99	5.40	35	101.4	13.47	2
RD-22	240.8	966.7	1.06	5.40	35	101.4	13.47	2
RD-23	238.3	970.6	1.07	5.40	35	101.4	13.47	2
RD-24	238.3	977.0	1.07	5.40	35	101.4	13.47	2
RD-25	366.9	1325.6	1.33	10.78	35	101.4	13.47	5
RD-26	368.8	1320.2	1.32	10.78	35	101.4	13.47	5
RD-27	424.4	1063.0	1.18	10.78	35	101.4	13.47	5
RD-3	200.0	915.5	1.05	4.44	57	101.4	13.47	2
RD-38	644.5	1324.6	1.32	9.14	57	294	19.38	5
RD-40	391.2	1105.0	1.11	4.44	57	294	19.38	2
RD-41	390.8	1106.0	1.11	4.44	57	294	19.38	2
RD-42	529.8	901.0	1.00	5.40	35	294	19.38	2
RD-43	422.4	1099.3	1.22	5.40	35	294	19.38	2
RD-47	680.6	1357.0	1.17	8.26	35	294	19.38	3
RD-48	786.4	1197.0	1.03	8.26	35	294	19.38	3
RD-49	811.3	1161.0	1.00	8.26	35	294	19.38	3
RD-53	475.1	1106.3	1.11	5.40	57	294	19.38	2
RD-54	473.6	1109.4	1.11	5.40	57	294	19.38	2
RD-59	970.1	1084.4	1.08	10.78	35	294	19.38	5
RD-60	479.8	1096.8	1.10	5.40	35	294	19.38	2
RD-63	478.6	1099.1	1.10	5.40	35	294	19.38	2
RD-67	1002.8	1052.4	1.05	10.78	35	294	19.38	5

* estimated change in target mass

The change in target mass due to the ballistic penetration was not provided in the RD experimental data set. In order to make use of this data set in the calibration process, the change in target mass was estimated based on the results of the target penetration hole relationship developed and presented previously, in which the target entry and exit hole diameters normalised based on projectile diameter (D/D_p) was related to the impact velocity overmatch (V_i/V_{50}). With these estimates of the target entry and exit hole diameters, the change in target mass is estimated based on the volume of the penetration hole and the density of steel (see Table 1).

The RD series data was selected for the model calibration process due to its wide range of shot conditions (e.g. impact velocity and obliquity, target and projectile types). This range of impact conditions and target combinations was expected to include the greatest range of penetration mechanisms and thus be the most complete test for the fragmentation model.

4.3.2.2 Experimental Validation Data

The behind-armour debris captured in witness packs in the 3500 experiment series are used in this report as the basis of validation of the target fragmentation model. The data set includes 10 BA-debris tests identified as Test 3527 to Test 3536. These tests consisted of 12.7mm (0.5 in.) AP ammunition at various impact velocities against a 10mm thick RHA steel target at zero degrees obliquity. The projectile, target plate and witness pack data used by the DeCaM software to describe the BA debris experiments, for the characterisation process, are listed in Table 4.6.

Table 4.6: Validation Data Used in DeCaM BA Debris Characterisation Process

Parameter	Value	Parameter	Value
Witness Pack Angle [deg]	0.0	Location of impact point [cm]	X: 31.00 Y: 31.00 Z: -70.00
Witness pack plate spacing [cm]	2.54	Projectile mass [g]	26.0
Z reference [cm]	70.0	Impact velocity [m/s]	*
Target thickness [mm]	10.0	Projectile base diameter [mm]	12.7
Target density [kg/m^3]	7850	Imaging resolution [cm^2]	0.006
Young's Modulus [GPa]	207	Minimum allowed mass [g]	0.000
Target yield strength [MPa]	900	Matching area ratio	4.0
Fracture toughness [MPa m$^{1/2}$]	100.0	Matching radius multiplier	1.5
Minimum fragment size [cm^2]	0.000	Matching minimum distance [cm]	0.5
Target obliquity [deg]	0.0	Projectile X window offset [cm]	5.0
Fragment shape factor [m^2/kg$^{2/3}$]	**	Projectile Y window offset [cm]	5.0
Target hole side slope [deg]	30	Number of projectile fragments	1
Target mass before test [g]	*	Plate data file type	*
Target mass after test [g]	*	Number of plates	*

* Unique to each test (See Table 4.5)

** Calculated in the characterisation process (see Table 3.15)

Experimental conditions unique to each test and experimental measurements are listed in Table 4.7. The final target mass was set to zero and the change in target mass was used as the initial mass in the DeCaM characterisation process.

Table 4.7: Experimental Validation Data and Measurements Unique to Each Test

Test ID	Change in Target Mass [g]	Impact Velocity, V_I [m/s]	Velocity Overmatch, V_I / V_{50}	Proj. Residual Velocity, V_R [m/s]	Debris Velocity, V_D [m/s]
3527	10.0	693.6	1.98	557.9	--
3528	10.0	699.9	2.00	514.6	--
3529	6.0	705.4	2.02	553.1	231.3
3530	11.0	697.8	1.99	505.2	222.5
3531	8.0	542.4	1.55	345.9	--
3532	10.0	521.1	1.49	303.1	--
3533	10.0	541.0	1.55	327.0	--
3534	10.0	627.4	1.79	460.5	--
3535	8.0	628.5	1.80	465.6	--
3536	10.0	622.3	1.78	446.0	--

4.3.3 Fragmentation Model Calibration

In this section, experimental behind-armour debris data describing the number of fragments generated in the penetration event is compared with the fragmentation model. The objective of this comparison is to calibrate the formulation of the mean number of debris fragments and to calibrate the predicted variability of the fragmentation process. In a review of the difference between the predicted (mean) and characterised number of fragments it is possible to identify a consistent percentage error. This systematic difference between the observed and predicted number of fragments is termed the modelling error (Δ). The deviation about the mean value may be described in terms of a confidence interval which contains a given percentage (λ) of the observed distributed data. The two stage calibration process in the sections which follow identifies the most appropriate modelling error value (Δ) and confidence level (λ).

4.3.3.1 Results of DeCaM 2.0 Fragmentation Model Results

The BA debris fragmentation model calibration was completed by comparing the RD series experimental data with the number of fragments predicted in DeCaM 2.0's characterisation process. The DeCaM fragmentation model is the same as that described above and is used in conjunction with the witness pack velocity threshold curves and the automated shape factor selection option. The results of this calibration process are shown in Table 4.8 and Figure 4.9.

Table 4.8 compares the number of holes in the first witness pack plate (approximate number of fragments since multiple fragments may pass through a single WP hole) with the number of fragments characterised by DeCaM 2.0 and the number of fragments predicted by the fragmentation model. A comparison of this data in terms of the modelling error (Δ) or other means indicates that DeCaM does a reasonable job of estimating the number of debris fragments one should expect from a particular ballistic penetration event.

The difference between the predicted mean and characterised number of fragments was reviewed to identify the 80% confidence interval for the data. It was noted that a confidence interval of ±60% of the mean expected number of fragments captured 80% of the differences between the predicted and experimental data. The 80% confidence interval range is provided in the last column of Table 4.8 and is bounded in Figure 4.9 by dotted lines. The experimental results in Figure 4.9 are plotted in ascending order of the number of fragments predicted by the fragmentation model. This manipulation allows one to graphically compare the predicted trend with the experimental data.

Table 4.8: Fragmentation Model Calibration Results

Test Number	Test ID	No. of Holes In First Plate	No. of Fragments Characterised	Expected or Mean No. of Fragments	Modelling Error [Mean / Characterised]	80% Confidence Interval [Mean (1+0.6)]
1	Rd-21	13	11	4	0.37	2 - 6
2	Rd-27	4	4	6	1.50	2 - 10
3	Rd-48	11	11	7	0.64	3 - 11
4	Rd-14	8	8	11	1.38	4 - 17
5	Rd-24	21	20	16	0.76	6 - 26
6	Rd-38	6	4	18	4.50	7 - 30
7	Rd-17	17	15	21	1.40	8 - 33
8	Rd-22	12	10	21	2.10	8 - 33
9	Rd-49	23	21	23	1.10	9 - 37
10	Rd-40	77	68	24	0.35	10 - 38
11	Rd-1	36	33	27	0.82	11 - 43
12	Rd-63	18	15	27	1.80	11 - 43
13	Rd-23	22	22	31	1.41	12 - 49
14	Rd-26	52	50	32	0.64	13 - 50
15	Rd-25	52	51	35	0.69	14 - 55
16	Rd-42	49	44	37	0.84	15 - 59
17	Rd-10	65	59	38	0.64	15 - 62
18	Rd-3	15	14	41	2.93	16 - 65
19	Rd-54	63	60	42	0.70	17 - 66
20	Rd-60	103	92	45	0.49	18 - 73
21	Rd-43	127	122	48	0.39	19 - 76
22	Rd-59	81	76	51	0.67	20 - 81
23	Rd-41	91	85	56	0.66	22 - 90
24	Rd-2	28	25	64	2.56	26 - 102
25	Rd-67	83	81	75	0.93	30 - 119
26	Rd-53	81	75	85	1.13	34 - 135
27	Rd-47	150	146	115	0.79	46 - 185

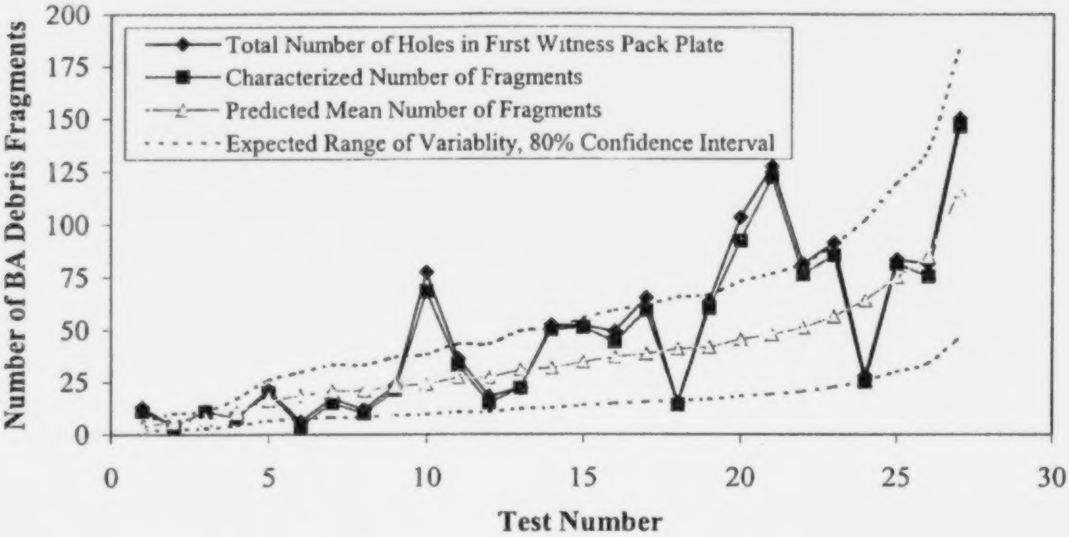

Figure 4.9: Fragmentation Model Calibration Results
(Test numbering as shown in Table 4.8)

4.3.4 Fragmentation Model Validation

The RD experimental data series was used in the previous section to calibrate the fragmentation model. In this section, an independent BA debris experimental data set (3500 series) is used to validate the selected calibration constants. As before, the BA debris test results were characterised using DeCaM 2.0 to predict the number of debris fragments for each ballistic penetration event. The number of holes in the first plate of the witness pack, the number of fragments characterised by DeCaM 2.0 and the results of the fragmentation model are compared in Table 4.9 and Figure 4.10 in this validation.

Table 4.9: Fragmentation Model Validation Results

Test Number	Test ID	No. of Holes In First Plate	No. of Fragments Characterised	Expected or Mean No. of Fragments	Modelling Error [Mean / Characterised]	80% Confidence Interval [Mean (1+0.6)]
1	3528	4	4	3	0.75	1 - 5
2	3529	5	5	3	0.60	1 - 5
3	3527	7	5	4	0.80	2 - 6
4	3530	5	5	6	1.20	2 - 10
5	3533	6	6	6	1.00	2 - 10
6	3532	9	7	7	1.00	3 - 11
7	3536	7	7	8	1.14	3 - 13
8	3531	11	10	10	1.00	4 - 16
9	3534	13	10	10	1.00	4 - 16
10	3535	9	7	10	1.43	4 - 16

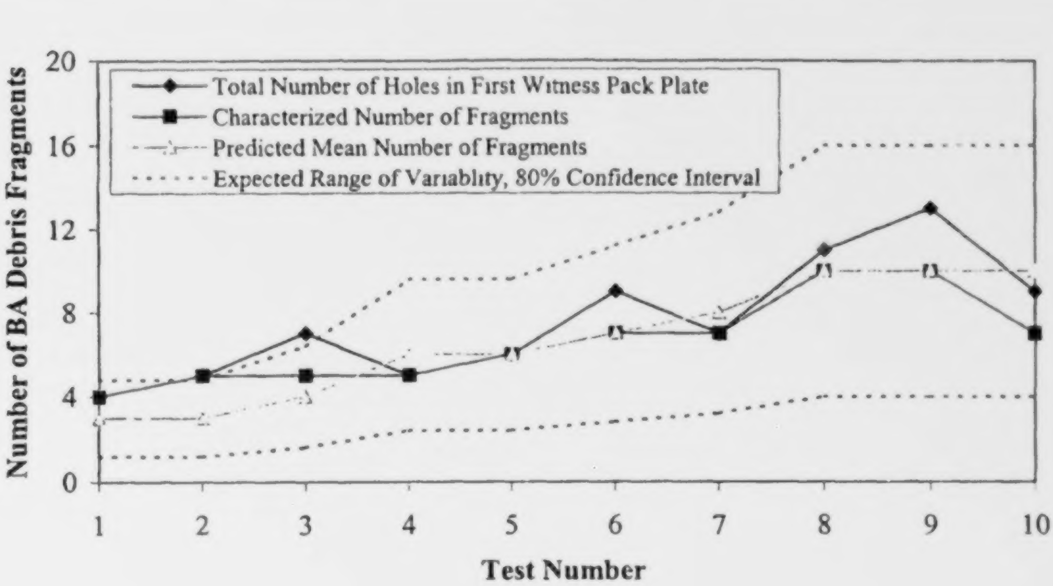

Figure 4.10: Fragmentation Model Validation Results
(Test numbering as shown in Table 4.9)

The results of the validation indicate that the model is a reasonable predictor of the mean number of fragments. However, the variability associated with the RD experimental test series which includes multi-layered targets is much higher than that displayed by the single layer 3500 series BA debris tests. If the calibration were completed based on the 3500 series data the 80% confidence interval would be significantly smaller. It is also important to note that these tests only included single layer targets and generated smaller numbers of BA debris fragments reducing the variability in the fragmentation model results.

4.4 Modelling Process Status

The modelling process review, calibration and validation based on a comparison with experimental data suggests that the DeCaM 2.0 modelling process is soundly grounded on scientific / engineering theory and agrees well with observed trends. Additional effort should however be spent in improving the predictive capabilities of the algorithms. A detailed combined energy, momentum and mass balance could be used to link the number of fragments generated in a penetration event to their mass, velocity and trajectory distributions. It is suggested that future development work focus on further developing the predictive (modelling) capabilities of the DeCaM software.

5.0 DECAM SOFTWARE

5.1 DeCaM Software Introduction

5.1.1 DeCaM 2.0 Software Overview

The behind-armour debris characterisation modelling process and its improvements described in the previous sections have been implemented in the DeCaM 2.0 software package. This section describes the DeCaM hardware and software requirements and how to install the software. The on-line help menus provided with the DeCaM software are complete and should provide the user with sufficient information to operate the software and interpret the input data.

5.1.1.1 Hardware and Software Requirements

The DeCaM 2.0 software was written for use in a Windows 32 bit operating environment (Win 95 or Win NT) on an IBM PC compatible computer. The software was tested in a Windows 95 and Windows NT operating environment and no problems were identified.

The computer on which the software is to be run should be at least a 486 with a minimum of 16 megabytes of RAM and 10 megabytes of free hard disk space.

5.1.1.2 Software Installation

The DeCaM Software is provided on a CD-ROM which includes four subdirectories:

- Install - containing the setup.exe program to install the DeCaM software on a PC
- Source Code - containing the ANSI C DeCaM software engine source code
- Report - containing MS Word document reports in support of DeCaM's development
- Data - additional data files for use with the DeCaM software

Follow the following steps to install the DeCaM software:

1) Place the CD-ROM in the CD-ROM drive
2) Press the Windows "Start" button
3) Select the "Run" menu item
4) Select "Browse"
5) Select the CD-ROM and then the "Install" folder
6) Double click on the "setup.exe" program

The user will be asked to approve the name of the DeCaM software program group name "Debris Characterisation and Modelling". The user should accept this name or provide a new one. The user will also be asked to approve the drive and directory in which the DeCaM software is installed.

The following is a list of files installed and subdirectories created by the DeCaM installation software in the directory specified by the user during the set-up process:

decam.exe
mppm32.exe
_isreg32.dll
decam.cnt
decam.hlp
_deisreg.isr
DelsL1.isu
mppm32.pif

..\Data
all *.sht
*.rpt
*.res
*.sim
*.mod
*.dcm
*.vel

..\Database
MATDB.dcm
PJDB.dcm
TRPDB.dcm
WPDB.dcm

The "exresult" and "exshot" files are sample input and output data files used and generated by the DeCaM 2.0 software. The "rd_67_" files are sample witness pack data files generated by the witness pack review process. Their format is shown in Appendix B.

5.1.1.3 Software Limitations

The DeCaM software characterisation capabilities are limited due to the memory capacity of the computer and platform it is running on. The debris characterisation process is limited to a maximum of ten witness pack plates with a maximum of 750 holes on each plate.

5.1.2 Scope of DeCaM 2.0 Software Improvements

In addition to the analytical improvements to the characterisation and modelling processes, the functionality and presentation of the DeCaM software was improved. The major modifications to the DeCaM software have improved:

- the functionality of the software by incorporating databases to facilitate data entry,
- the presentation of the software and its results by updating the data entry menus and, in general, improving the graphics and animation for the analysis results, and
- clearly defining the accuracy of the probabilistic modelling solution.

5.2 Witness Pack, Projectile, Target and Material Databases

It was noted that the description of a BA debris test or modelling configuration is a time consuming task due to the large number of parameters which the user must select. In addition, it was noted that a variety of standard WP configurations, armour systems, or projectile descriptions might be used repetitively. Therefore, it was decided to simplify the data entry approach and incorporate material, projectile, witness pack and target databases. Figure 5.1 illustrates the DeCaM 2.0 characterisation data entry dialog box, which includes five tabs associated with each data group. This "tabbed" data group arrangement along with graphical data definition information facilitates the data entry and review processes. The DeCaM 2.0 modelling data is presented in a similar fashion.

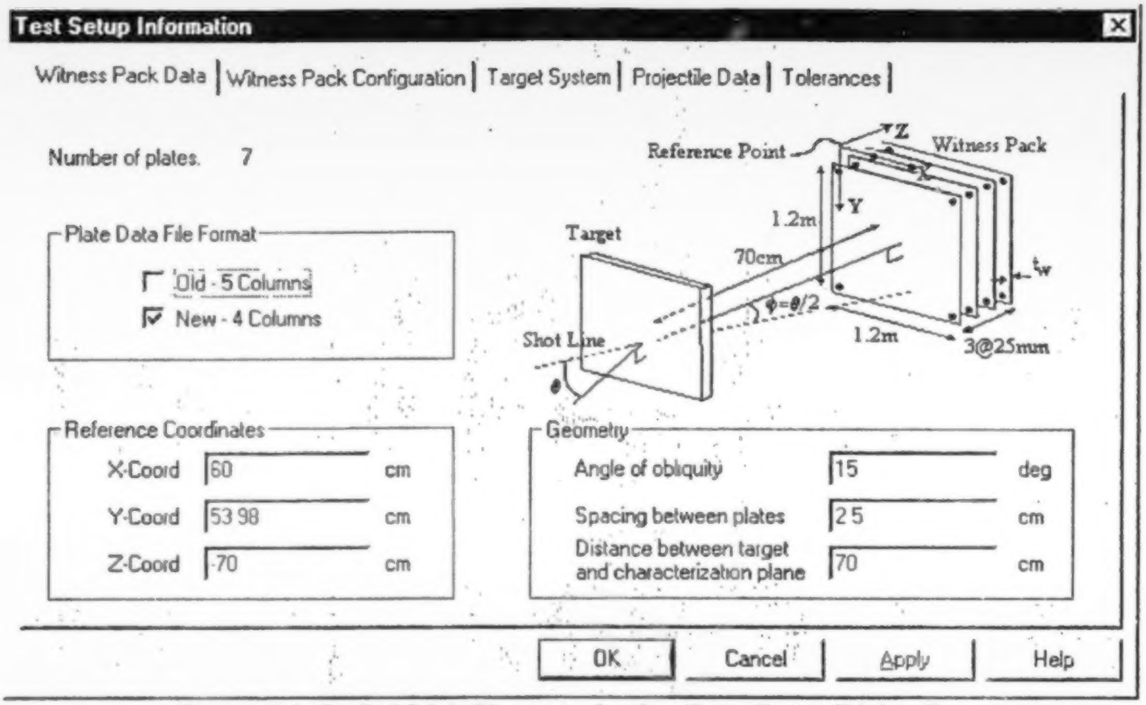

Number of plates. 7

Plate Data File Format

☐ Old - 5 Columns

☑ New - 4 Columns

Reference Coordinates

X-Coord	60	cm
Y-Coord	53.98	cm
Z-Coord	-70	cm

Geometry

Angle of obliquity	15	deg
Spacing between plates	2.5	cm
Distance between target and characterization plane	70	cm

Figure 5.1: DeCaM 2.0 Characterisation Data Entry Dialog Box

In order to simplify the assembly of characterisation or modelling scenario descriptions and reduce data entry errors, databases for standard witness pack configurations, target armour systems, projectiles and materials have been incorporated in DeCaM 2.0. For example, Figure 5.2 shows the DeCaM 2.0 projectile data entry dialog and the range of data the user must enter to completely describe a projectile in the characterisation process. Instead of entering each piece of data individually, the user may opt to select a standard projectile from the projectile database by clicking on the "Load from Database" button on the dialog box. The data contained in the database may be supplemented by the user, for future characterisation and modelling sessions, by clicking on the "Save to Database" button.

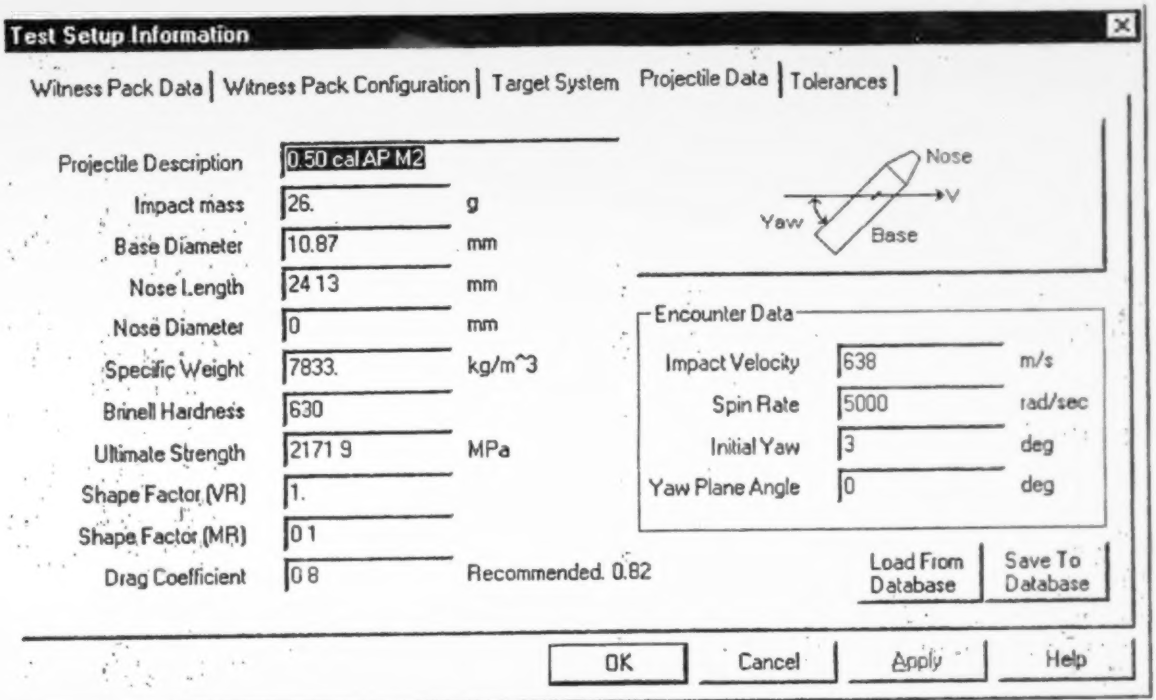

Projectile Description: 0.50 cal AP M2
Impact mass: 26. g
Base Diameter: 10.87 mm
Nose Length: 24 13 mm
Nose Diameter: 0 mm
Specific Weight: 7833. kg/m^3
Brinell Hardness: 630
Ultimate Strength: 2171 9 MPa
Shape Factor (VR): 1.
Shape Factor (MR): 0 1
Drag Coefficient: 0 8 Recommended. 0.82

Encounter Data
Impact Velocity: 638 m/s
Spin Rate: 5000 rad/sec
Initial Yaw: 3 deg
Yaw Plane Angle: 0 deg

Figure 5.2: Projectile Data Entry Dialog Box

When the user opts to load projectile data from the DeCaM 2.0 database, they are presented with the projectile database dialog as shown in Figure 5.3. A projectile type is selected by clicking on the projectile title and then selecting the OK button. The scroll bars are used to display additional projectile types and projectile data fields. Since all of the data shown in Figure 5.2, with the exception of the "Encounter Data", is presented on one line in the projectile database dialogue the user must use the horizontal scroll bar to view all of the information for a given projectile.

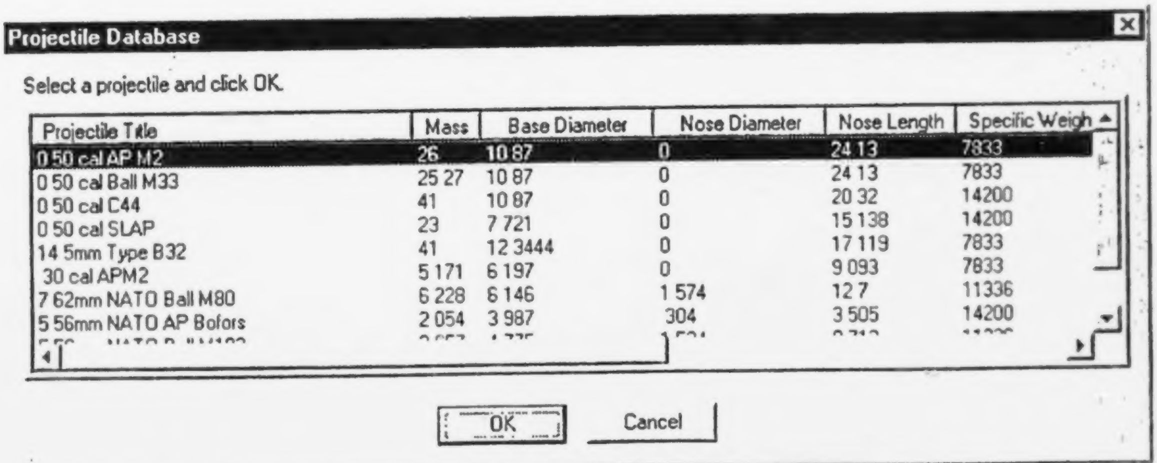

Select a projectile and click OK.

Projectile Title	Mass	Base Diameter	Nose Diameter	Nose Length	Specific Weigh
0 50 cal AP M2	26	10 87	0	24 13	7833
0 50 cal Ball M33	25 27	10 87	0	24 13	7833
0 50 cal C44	41	10 87	0	20 32	14200
0 50 cal SLAP	23	7 721	0	15 138	14200
14 5mm Type B32	41	12 3444	0	17 119	7833
30 cal APM2	5 171	6 197	0	9 093	7833
7 62mm NATO Ball M80	6 228	6 146	1 574	12 7	11336
5 56mm NATO AP Bofors	2 054	3 987	304	3 505	14200

Figure 5.3: Projectile Database Dialog Box

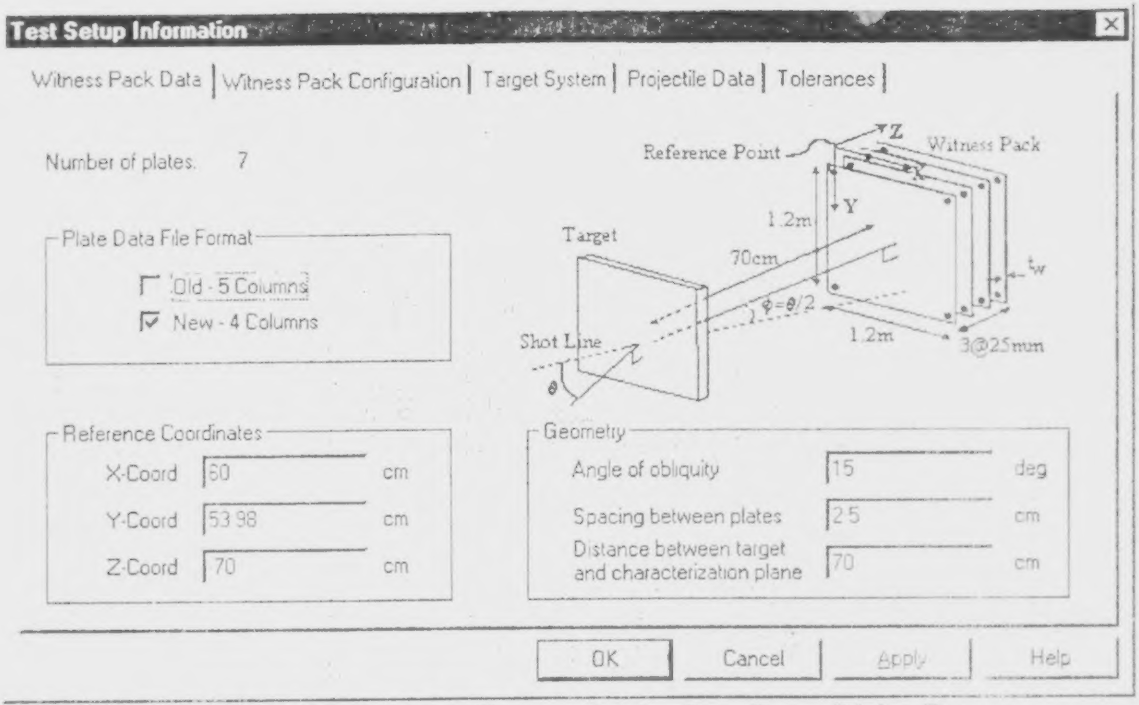

Number of plates: 7

Plate Data File Format
- ☐ Old - 5 Columns
- ☑ New - 4 Columns

Reference Coordinates

X-Coord	60	cm
Y-Coord	53.98	cm
Z-Coord	70	cm

Geometry

Angle of obliquity	15	deg
Spacing between plates	2.5	cm
Distance between target and characterization plane	70	cm

Figure 5.1: DeCaM 2.0 Characterisation Data Entry Dialog Box

In order to simplify the assembly of characterisation or modelling scenario descriptions and reduce data entry errors, databases for standard witness pack configurations, target armour systems, projectiles and materials have been incorporated in DeCaM 2.0. For example, Figure 5.2 shows the DeCaM 2.0 projectile data entry dialog and the range of data the user must enter to completely describe a projectile in the characterisation process. Instead of entering each piece of data individually, the user may opt to select a standard projectile from the projectile database by clicking on the "Load from Database" button on the dialog box. The data contained in the database may be supplemented by the user, for future characterisation and modelling sessions, by clicking on the "Save to Database" button.

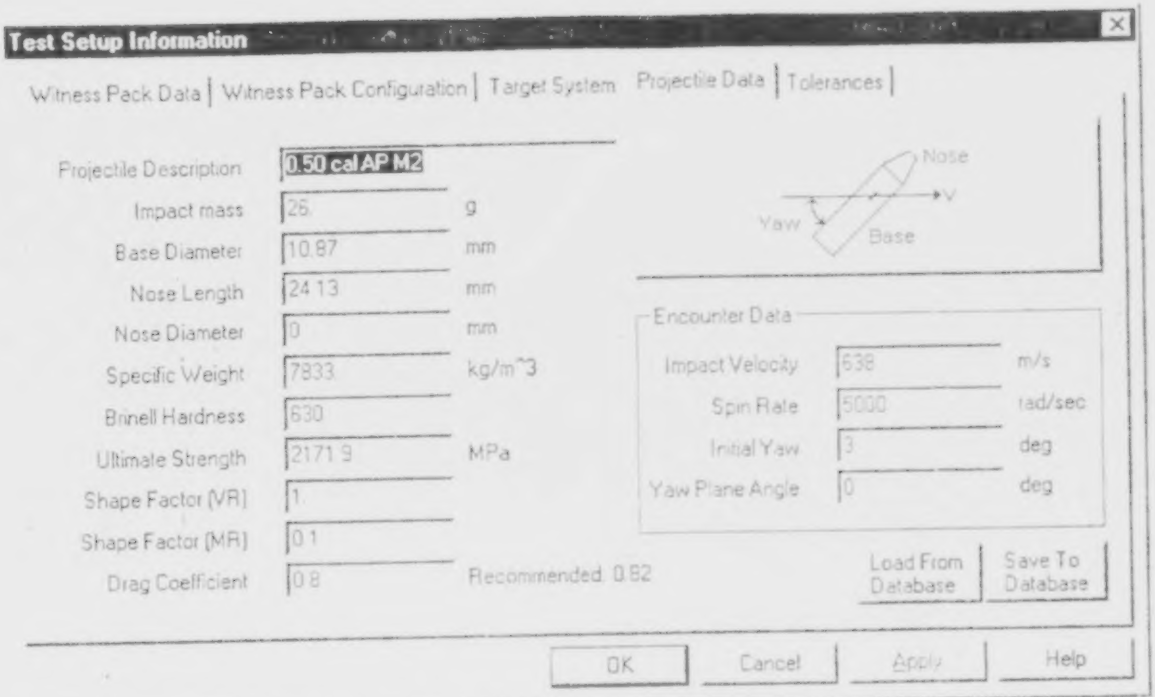

Projectile Description: 0.50 cal AP M2
Impact mass: 26 g
Base Diameter: 10.87 mm
Nose Length: 24.13 mm
Nose Diameter: 0 mm
Specific Weight: 7833 kg/m^3
Brinell Hardness: 630
Ultimate Strength: 2171.9 MPa
Shape Factor (VR): 1
Shape Factor (MR): 0.1
Drag Coefficient: 0.8 Recommended: 0.82

Encounter Data
Impact Velocity: 638 m/s
Spin Rate: 5000 rad/sec
Initial Yaw: 3 deg
Yaw Plane Angle: 0 deg

Figure 5.2: Projectile Data Entry Dialog Box

When the user opts to load projectile data from the DeCaM 2.0 database, they are presented with the projectile database dialog as shown in Figure 5.3. A projectile type is selected by clicking on the projectile title and then selecting the OK button. The scroll bars are used to display additional projectile types and projectile data fields. Since all of the data shown in Figure 5.2, with the exception of the "Encounter Data", is presented on one line in the projectile database dialogue the user must use the horizontal scroll bar to view all of the information for a given projectile.

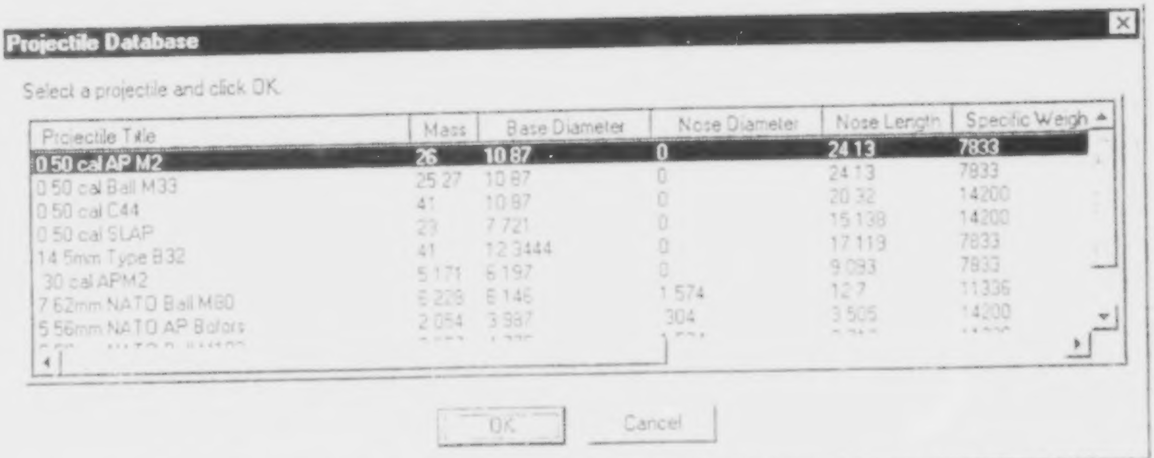

Select a projectile and click OK.

Projectile Title	Mass	Base Diameter	Nose Diameter	Nose Length	Specific Weigh
0.50 cal AP M2	26	10.87	0	24.13	7833
0.50 cal Ball M33	25.27	10.87	0	24.13	7833
0.50 cal C44	41	10.87	0	20.32	14200
0.50 cal SLAP	23	7.721	0	15.138	14200
14.5mm Type B32	41	12.3444	0	17.119	7833
.30 cal APM2	5.171	6.197	0	9.093	7833
7.62mm NATO Ball M80	6.228	6.146	1.574	12.7	11336
5.56mm NATO AP Bofors	2.054	3.937	.304	3.505	14200

Figure 5.3: Projectile Database Dialog Box

Databases similar to the projectile database have been assembled for the typical witness pack configurations (see Figure 5.4) and target systems (see Figure 5.5). As in the projectile database, these databases are populated with standard witness pack and target descriptions which the user may not edit, however, the user may add additional custom witness pack and target configurations to the database.

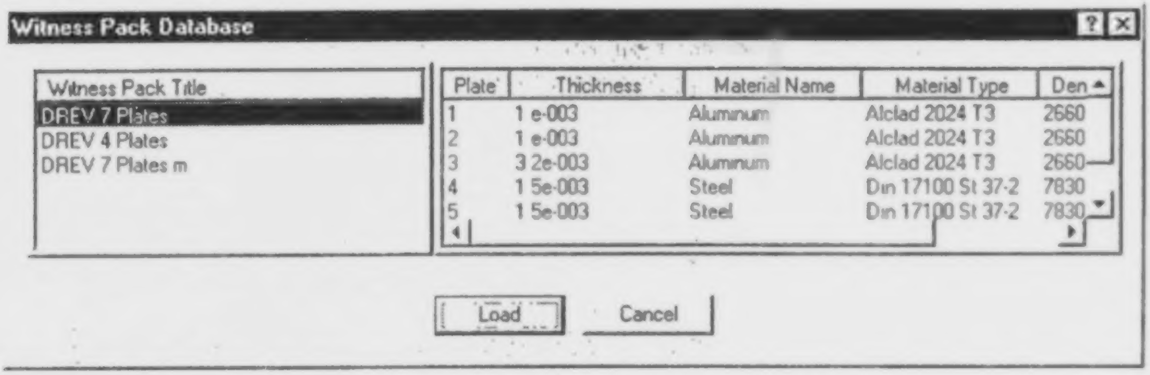

Witness Pack Title
DREV 7 Plates
DREV 4 Plates
DREV 7 Plates m

Plate	Thickness	Material Name	Material Type	Den
1	1 e-003	Aluminum	Alclad 2024 T3	2660
2	1 e-003	Aluminum	Alclad 2024 T3	2660
3	3 2e-003	Aluminum	Alclad 2024 T3	2660
4	1 5e-003	Steel	Din 17100 St 37-2	7830
5	1 5e-003	Steel	Din 17100 St 37-2	7830

Figure 5.4:Witness Pack Database Dialog Box

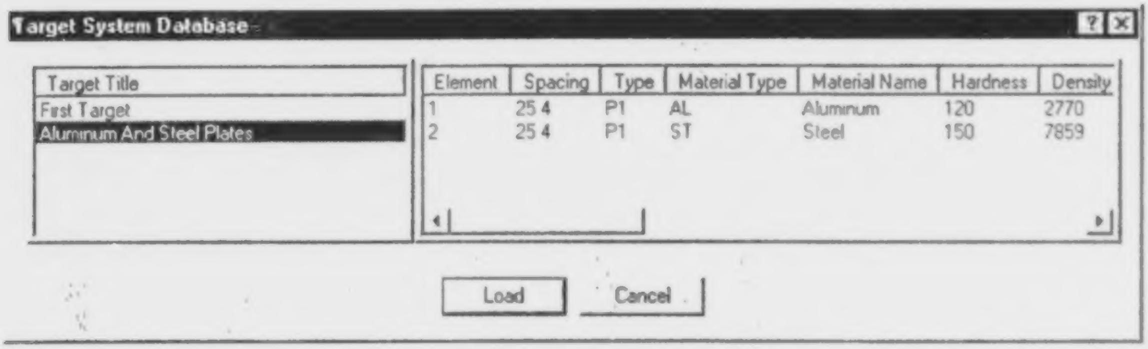

Target Title
First Target
Aluminum And Steel Plates

Element	Spacing	Type	Material Type	Material Name	Hardness	Density
1	25 4	P1	AL	Aluminum	120	2770
2	25 4	P1	ST	Steel	150	7859

Figure 5.5: Target System Database

A significant number of material parameters (e.g. density, yield strength and toughness) are required by DeCaM to describe the components used in a target system or a witness pack assembly. To facilitate the correct specification of material properties a material property database was included in DeCaM 2.0. The database includes a range of standard material descriptions which the user may not edit, but also allows the user to supplement this listing of materials by adding to the DeCaM 2.0 material database.

The material database is accessed thought the Data menu as shown in Figure 5.6, by selecting the material database option. Once the material database item located on the Data menu is selected, the material database dialogue box, Figure 5.7, is displayed. The user may review, edit, delete or add material type records at this point. When the user opts to add or edit a material type description by selecting the material description and clicking on the add material or edit material buttons, respectively, the Add/Edit Material dialogue box (see Figure 5.8) is used to present the material property fields of interest.

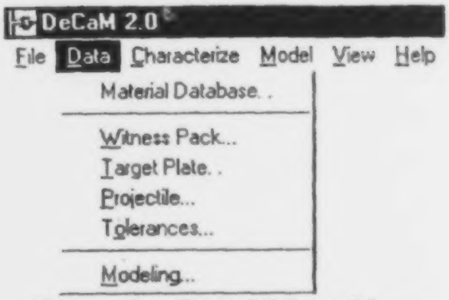

Figure 5.6: DeCaM Data Menu

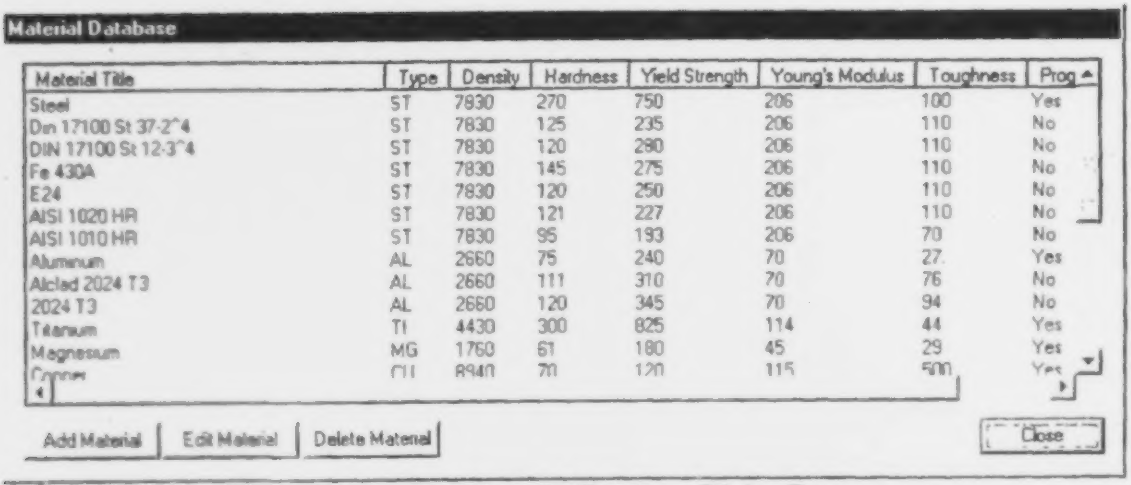

Material Title	Type	Density	Hardness	Yield Strength	Young's Modulus	Toughness	Prog
Steel	ST	7830	270	750	206	100	Yes
Din 17100 St 37-2^4	ST	7830	125	235	206	110	No
DIN 17100 St 12-3^4	ST	7830	120	280	206	110	No
Fe 430A	ST	7830	145	275	206	110	No
E24	ST	7830	120	250	206	110	No
AISI 1020 HR	ST	7830	121	227	206	110	No
AISI 1010 HR	ST	7830	95	193	206	70	No
Aluminum	AL	2660	75	240	70	27.	Yes
Alclad 2024 T3	AL	2660	111	310	70	76	No
2024 T3	AL	2660	120	345	70	94	No
Titanium	TI	4430	300	825	114	44	Yes
Magnesium	MG	1760	61	180	45	29	Yes
Copper	CU	8940	70	120	115	500	Yes

Figure 5.7: Material Database Dialog Box

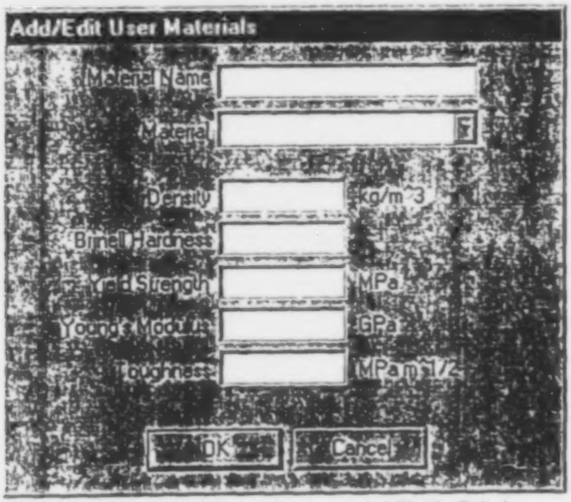

Figure 5.8: Material Database Add/Edit Dialogue box

Changes to the material property database affect the options which are displayed in the pull-down menus used to select material types in the target and witness pack description dialogues (e.g. WP Configuration or Target System tabs in Figure 5.1) and databases (Figures 5.4 and 5.5).

Databases similar to the projectile database have been assembled for the typical witness pack configurations (see Figure 5.4) and target systems (see Figure 5.5). As in the projectile database, these databases are populated with standard witness pack and target descriptions which the user may not edit, however, the user may add additional custom witness pack and target configurations to the database.

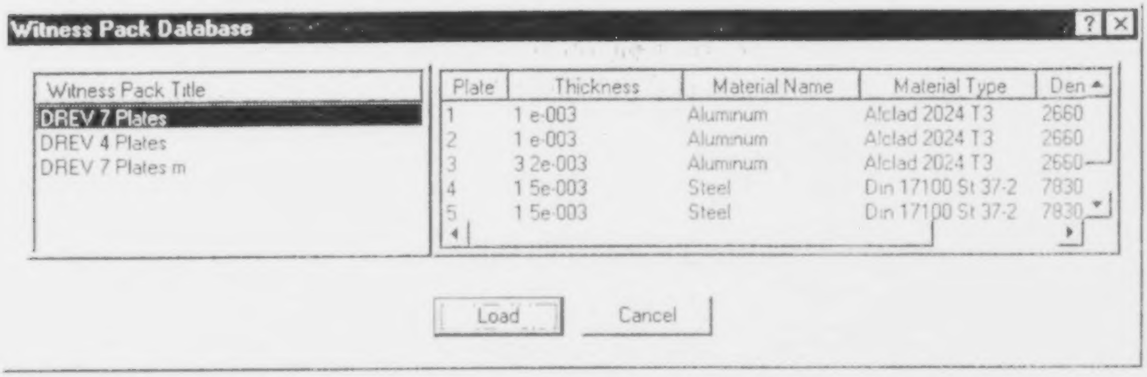

Witness Pack Title
DREV 7 Plates
DREV 4 Plates
DREV 7 Plates m

Plate	Thickness	Material Name	Material Type	Den
1	1 e-003	Aluminum	Alclad 2024 T3	2660
2	1 e-003	Aluminum	Alclad 2024 T3	2660
3	3 2e-003	Aluminum	Alclad 2024 T3	2660
4	1 5e-003	Steel	Din 17100 St 37-2	7830
5	1 5e-003	Steel	Din 17100 St 37-2	7830

Figure 5.4:Witness Pack Database Dialog Box

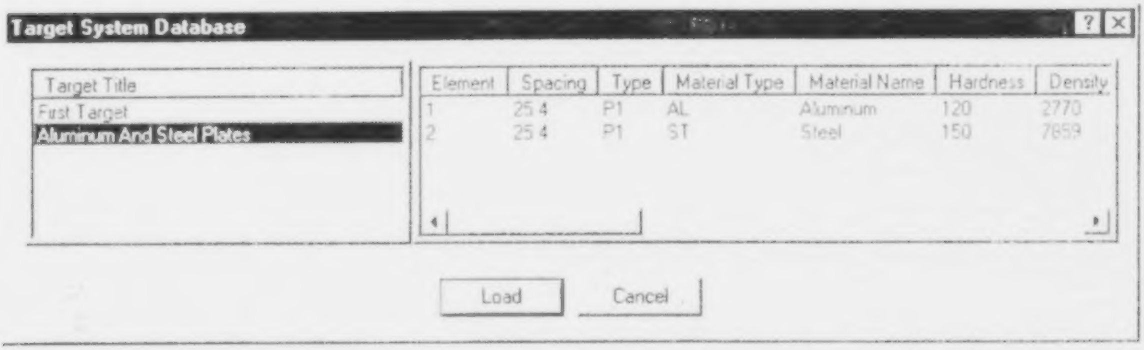

Target Title
First Target
Aluminum And Steel Plates

Element	Spacing	Type	Material Type	Material Name	Hardness	Density
1	25 4	P1	AL	Aluminum	120	2770
2	25 4	P1	ST	Steel	150	7859

Figure 5.5: Target System Database

A significant number of material parameters (e.g. density, yield strength and toughness) are required by DeCaM to describe the components used in a target system or a witness pack assembly. To facilitate the correct specification of material properties a material property database was included in DeCaM 2.0. The database includes a range of standard material descriptions which the user may not edit, but also allows the user to supplement this listing of materials by adding to the DeCaM 2.0 material database.

The material database is accessed thought the Data menu as shown in Figure 5.6, by selecting the material database option. Once the material database item located on the Data menu is selected, the material database dialogue box, Figure 5.7, is displayed. The user may review, edit, delete or add material type records at this point. When the user opts to add or edit a material type description by selecting the material description and clicking on the add material or edit material buttons, respectively, the Add/Edit Material dialogue box (see Figure 5.8) is used to present the material property fields of interest.

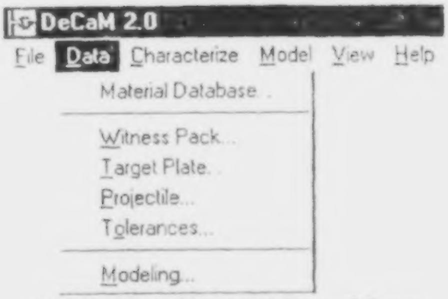

Figure 5.6: DeCaM Data Menu

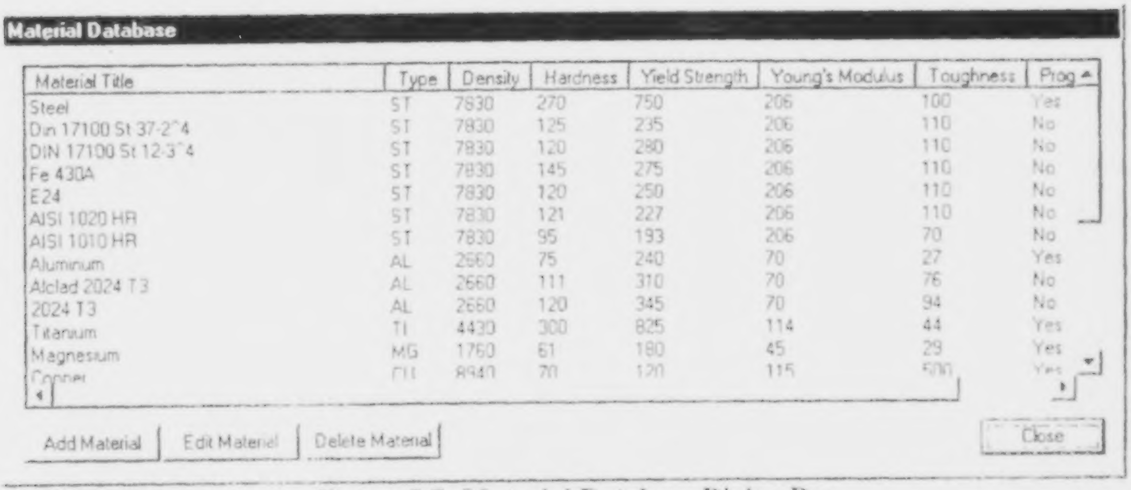

Material Title	Type	Density	Hardness	Yield Strength	Young's Modulus	Toughness	Prog
Steel	ST	7830	270	750	206	100	Yes
Din 17100 St 37-2^4	ST	7830	125	235	206	110	No
DIN 17100 St 12-3^4	ST	7830	120	280	206	110	No
Fe 430A	ST	7830	145	275	206	110	No
E24	ST	7830	120	250	206	110	No
AISI 1020 HR	ST	7830	121	227	206	110	No
AISI 1010 HR	ST	7830	95	193	206	70	No
Aluminum	AL	2660	75	240	70	27	Yes
Alclad 2024 T3	AL	2660	111	310	70	76	No
2024 T3	AL	2660	120	345	70	94	No
Titanium	TI	4430	300	825	114	44	Yes
Magnesium	MG	1760	61	180	45	29	Yes
Copper	CU	8940	70	120	115	500	Yes

Figure 5.7: Material Database Dialog Box

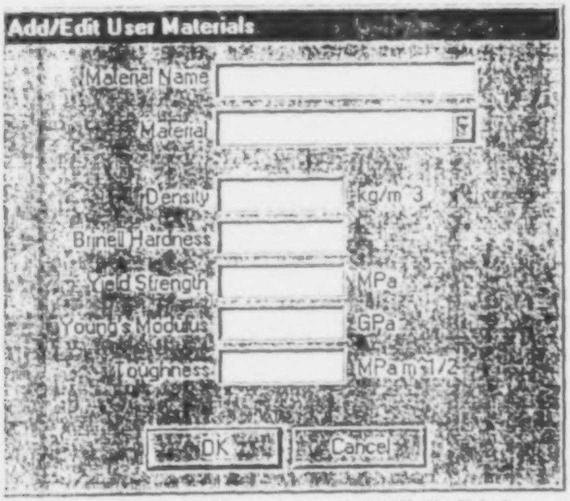

Figure 5.8: Material Database Add/Edit Dialogue box

Changes to the material property database affect the options which are displayed in the pull-down menus used to select material types in the target and witness pack description dialogues (e.g. WP Configuration or Target System tabs in Figure 5.1) and databases (Figures 5.4 and 5.5).

5.3 Probabilistic Solution Automated Result Accuracy Feature

In order to develop a probabilistic BA debris modelling result with DeCaM 2.0, it was necessary for the user to indicate the number of simulations to be completed to generate the desired result. The convergence of a simulated probabilistic result is dependant on the random variable distributions, the simulation technique and the number of simulated results incorporated in the result statistics. Therefore, since the user was only able to specify the number of simulation runs required, DeCaM 2.0 only offered limited control of the convergence or accuracy of the reported probability values.

The modification which was proposed for DeCaM 2.0, to avoid the uncertainty in solution accuracy, was to allow the user to specify the simulation convergence accuracy. Figure 5.6 presents the DeCaM 2.0 probabilistic modelling parameter dialog box. In this revised dialog box the user may select to direct the probabilistic BA-debris modelling process based on the number of simulated results incorporated in the result statistics or alternatively an accuracy convergence criteria may be specified, by clicking on the adjacent check box.

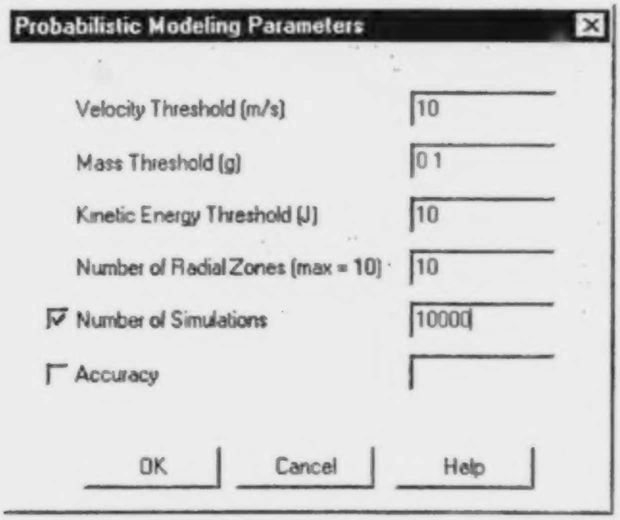

Velocity Threshold (m/s) 10
Mass Threshold (g) 0.1
Kinetic Energy Threshold (J) 10
Number of Radial Zones (max = 10) 10
☑ Number of Simulations 10000
☐ Accuracy

Figure 5.6: Probabilistic Modelling Parameter Dialog Box

In the development of a probabilistic modelling result, all of the simulated fragment velocities, masses and kinetic energies are sorted into magnitude and deposition plane location ranges. By monitoring the change in the number of observations in each bin relative to the total number of simulated fragments, the accuracy of the solution is determined. The user is asked to specify the "accuracy" convergence level which is compared against the stability of the solution accuracy. By specifying an "accuracy" convergence level of 0.001 the user is indicating that the maximum allowable error in the modelling probabilistic results (probabilities) will be 0.1%.

The probabilistic simulation convergence criteria operates based on the following logic:

1) Set fragment mass, velocity and energy distribution intervals to zero ($p_i = 0$)

2) Set simulation interval (S) to $\frac{5}{\text{Accuracy}}$

3) Perform deterministic simulation process S times and collect the debris characteristics to develop fragment distribution interval probabilities (p_i)

4) Check for fragment probability distribution interval convergence

   4a) If the change in each fragment distribution interval probability, over the last S simulations, is less than Accuracy ($\Delta p_i \leq \text{Accuracy}$)
   - then probabilistic simulation is complete

   4b) If the change in any fragment distribution interval probability, over the last S simulations, is greater than Accuracy ($\Delta p_i > \text{Accuracy}$)
   - then set simulation interval (S) to $\frac{1}{\text{Accuracy}}$
   - Repeat steps 3 and 4 up to 8 times

It is noted that the fragment distribution statistics are comprised of information developed from amongst all of the simulated fragments with the exception of those having masses lower than the minimum mass or having velocities greater than the maximum permissible (impact velocity).

5.4 Improve DeCaM Graphics and Animation

In order to improve the presentation of the DeCaM characterisation and modelling results, work was carried out towards the improvement of the program's graphics and animation. This work involved the conversion of the DeCaM software to a 32 bit system in which OpenGL and a variety of graphics tools could be used. The two most significant improvements in this area involved the 3D animation and statistical distribution data viewer.

The BA-debris animation illustrating the characterisation and modelling results are shown in Figure 5.7. The animation illustrates the projectile trajectory of the projectile before and after target penetration based on the results of MPPM3. The size and trajectory of the BA-debris fragments resulting from the ballistic penetration event are also shown in the animations. Fragments are depicted as rectangular prisms whose aspect ratios and volumes are proportionate to the characterised or predicted fragment sizes.

The characterisation and modelling viewers are set-up to allow the user to zoom in or out and translate or rotate the field of view. The animation may be advanced frame by frame or run from beginning to end using the VCR type control buttons. Individual witness pack plates may be hidden in the characterisation viewer by selecting the plate number (e.g. plate 1 = P1).

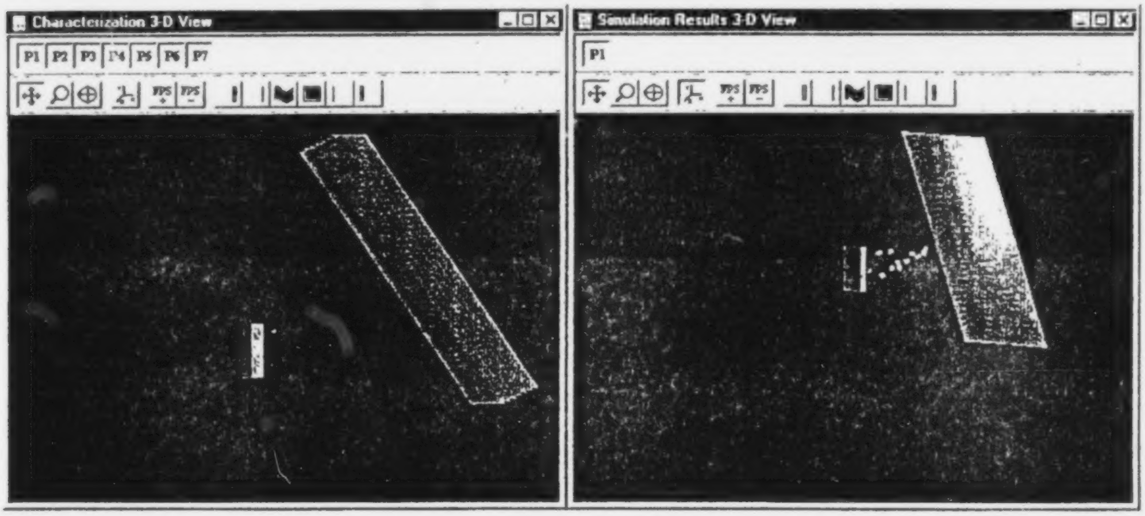

Figure 5.7: DeCaM 2.0 Characterisation and Modelling 3D BA-Debris Animation

In addition the enhancements in the characterisation and modelling results 3D animation DeCaM 2.0 includes improvements in the BA-debris statistical distribution viewer (see Figure 5.8). The user may view fragment velocity, mass, radius from the debris cloud centroid and number of fragments simply by selecting the named tabs in the statistical distribution viewer window.

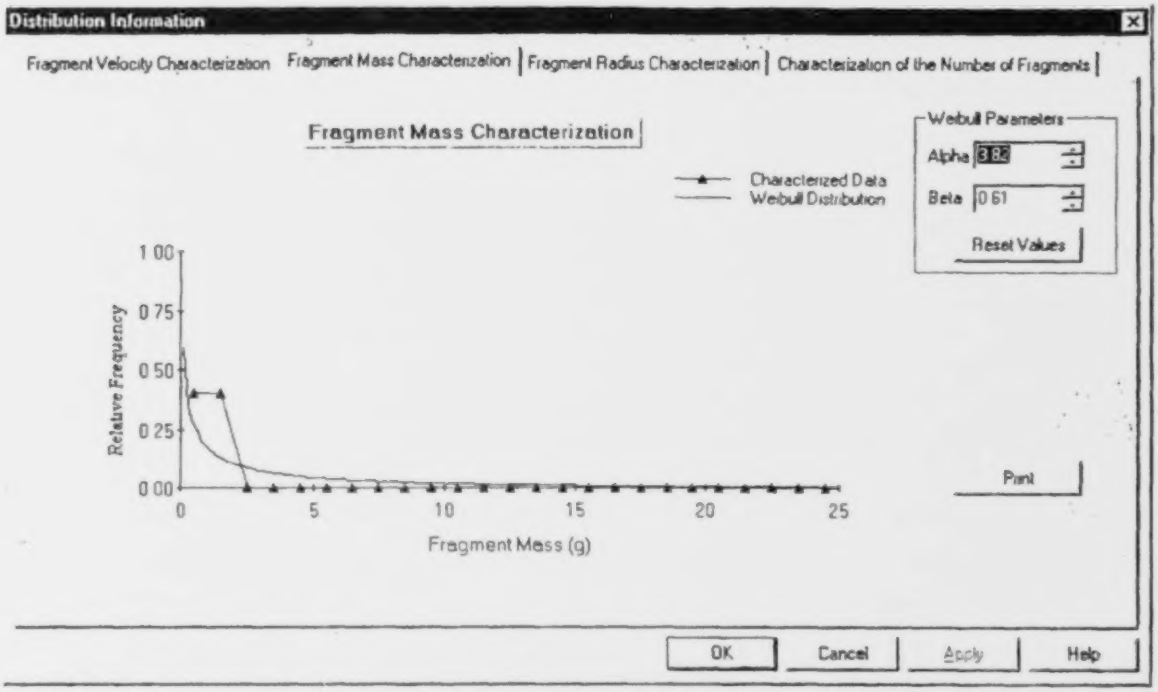

Alpha 3.82

Beta 0.61

Figure 5.8: BA-Debris Statistical Distribution Viewer

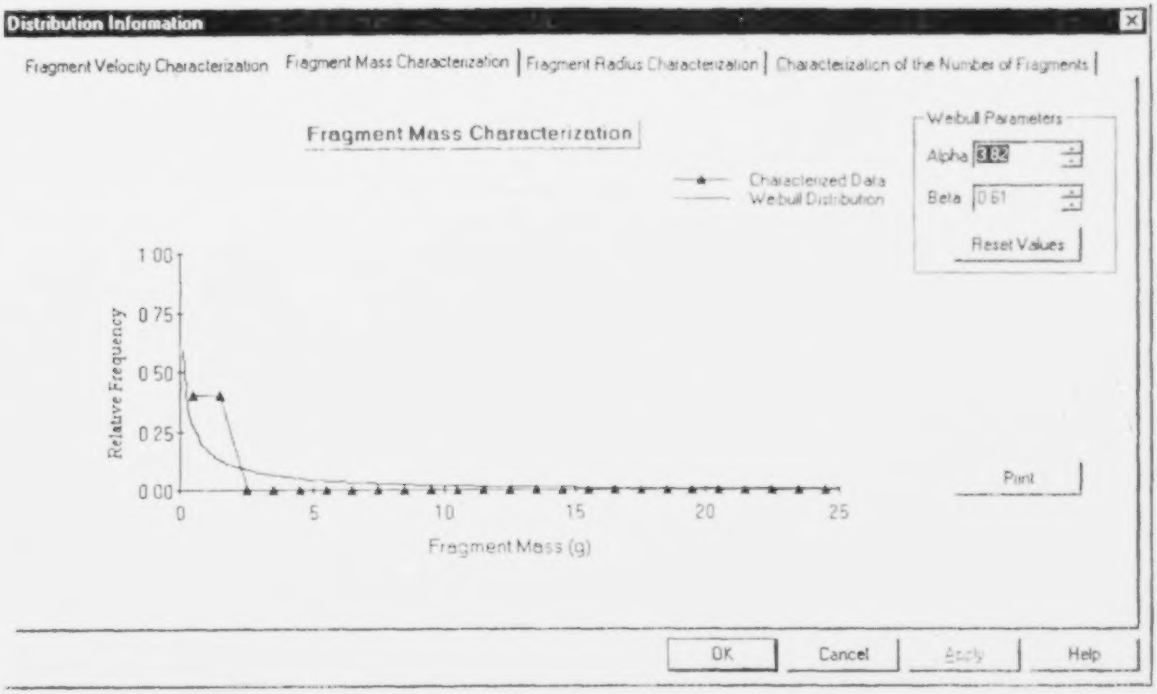

Alpha 3.82

Beta 0.61

Figure 5.8: BA-Debris Statistical Distribution Viewer

6.0 CONCLUDING REMARKS AND RECOMMENDATIONS

6.1 Concluding Remarks

The behind-armour debris characterisation and modelling processes employed in the DeCaM software were extended using sound scientific / engineering principles and were validated against available behind-armour debris test data. The work completed in this project included literature reviews to identify the state-of-the-art in behind-armour debris modelling, target penetration frontal splash and target spall modelling.

The implemented improvements were aimed at extending the applicability and capability of the behind-armour debris characterisation and modelling (DeCaM) software. These improvements included:

- the addition of MPPM3 algorithms for projectile penetration predictive capabilities,
- modifications to the witness pack characterisation hole matching process,
- the development of an automated probabilistic modelling result solution accuracy feature,
- target penetration and fragmentation model revisions and recalibration,
- the incorporation of witness pack penetration threshold curves, and
- improvements to multiple layer target treatment.

In addition, the DeCaM software was improved through the addition of witness pack, projectile, target and material property databases. The animation and presentation of the characterisation and modelling data and results were also improved in this project.

6.2 Recommendations

The following recommendations outline areas within the current characterisation and modelling process which deserve further attention and extensions to the current model to embrace a wider range of applications. The recommendations presented in each of the three subsequent sections are subjectively arranged to in order of their potential for technical improvement of the DeCaM software.

6.2.1 Recommended Calibration and Revisions to the Current Model

While the current DeCaM software provides results which agree with observed trends, its range of application and confidence in its results could be enhanced. Suggested improvements and validation / calibration studies for the characterisation and modelling processes are outlined below as recommendations for future work. It is suggested that the primary focus of future work should be in the further development of DeCaM's modelling capabilities.

Characterisation Process

- Based on a review of recovered fragments the witness pack hole growth algorithm could be improved.
- Consider consistency of fragment mass and velocity, estimated for related witness pack holes, in the characterisation process.
- Review and rationalise regressed threshold curves to ensure consistency of results
- The mass balance approach used to automatically select fragment shape factors should be revised to consider not only mass conservation but energy/momentum conservation.
- In general, multi-layered targets are not treated well and deserve additional attention.

Modelling Process

- A more detailed mass/energy/momentum balance could be used to improve the predictive capabilities of the DeCaM modelling process by estimating the debris velocity, mass and trajectory distribution parameters.
- Additional test data describing the debris generated by oblique penetration events should be reviewed to better model oblique penetration events.
- The modelling process could be reviewed to better estimate the debris cloud centroid trajectory (direction of the cone of lethality)
- In general, multi-layered targets are not treated well and deserve additional attention.
- Further study of target penetrations to measure the hole and its orientation with respect to the shot line could be completed to further validate the fragmentation model. At the same time, the orientation of cracking and the material failure mechanisms could be investigated to better understand the projectile penetration and fragmentation processes.
- Study the projectile erosion and break-up processes to better express their contributions to the residual penetrator projectile fragmentation energies.

6.2.2 Potential Extensions of the DeCaM Process

Potential extensions of the DeCaM software's capabilities were given some consideration to develop the following list of potential development topics :

- Characterisation and modelling of chemical energy (CE) projectile BA debris
- The addition of a secondary target plane (size, location and direction) could be defined to further develop the vulnerability / lethality model
- The model may be reviewed to ensure that it is capable of handling other projectile types (i.e. EFP's and shape charges)
- Develop a macroscopic dynamic spall damage accumulation model to handle non-penetrating impact events
- This characterisation and modelling approach could be applied in naval, air frame and spacecraft protection evaluation. Application to these other fields will require compilation of additional test data and revalidation of the models.
- The model may be used to calibrate witness packs and help in the further development of STANAG 4190
- The effects of the non-metallic layers in multi-layer targets on the fragmentation process should be investigated further.
- Fragmentation may be influenced by the impurities in the armour material (i.e. sulphur content has greater embrittlement capacity on larger grain materials). This idea could be pursued from a metallurgical perspective.

6.2.3 Possible Enhancements for the DeCaM Program

The functionality and presentation of the DeCaM software would improve with the consideration of the following items:

- add ability to have number of WP plates not match # of *.rpt files
- Allow multiple characterisation and modelling sessions be run and viewed simultaneously for comparison
- Improve 3D viewer to show fragment trajectories
- Improve deposition plane viewer to include functionality of sashview (i.e. display fragment hole data (hole number, area, co-ordinates, mass, velocity and kinetic energy) when a hole on the witness pack data viewer is selected)
- An extension to the modelling process could be developed to determine the possible origins of the projectile penetration in the target using a known location of the cone of lethality.
- Improve the interface such that current characterisation and modelling files are prominent.
- User selection of the colours used in the witness pack data viewer and deposition plane view for both deterministic and probabilistic models should be available. The user should also be able to specify the units of preference in these views.
- A built-in screen capture could be developed to "cut and paste" sections or whole views into other programs (e.g. Word, Excel, etc.).
- Modify the data structures used in the DeCaM software to remove the limitation of the number of fragments (750) imposed by the current program. This modification will allow the computer's available memory to limit the size of problem which may be handled but may require the ANSI C programming language restriction to be dropped.

7.0 REFERENCES

Al-Hassani, S.T.S., Chen, D., Sarumi, M., "A Simple Non-Local Spallation Failure Model", Int. J. Impact Engng. Vol. 19, Nos., 5-6, pp. 493-501, 1997.

Backman, M. E., Finnegan, S. A., "A Phenomenological Investigation of the Impact of Compact Projectiles against Plates at Speeds up to 3 km/s" 8th International Symposium on Ballistics, Orlando, Florida, 1984.

Backman, M., Goldsmith, W. "The Mechanics of Penetration of Projectiles into Targets" International Journal of Engineering Science, Vol. 16, pp. 1 – 99, 1978.

Baker, J. R, Persechino, M. A., "An Analytical Model of Hole Size in Finite Plates for Both Normal and Oblique Hypervelocity Impact for all Target Thicknesses up to the Ballistic Limit" International Journal of Impact Engineering, Vol. 14, pp. 73-84, 1993.

Buchar, J., Krejcf, J., "Spall Behaviour of the Low Alloyed High Strength Steel", Journal De Physique IV, Colloque C8, supplement au journal de physique III, Vol.4, 1994.

Buchar, J. Rolc, S., Hrebicek, J., "Strain Rate Dependence of the Spall Strength of Steels", J. Phys. IV, France 7, Colloque C3, Supplement au Journal de Physique III d'aout, 1997.

Bodner, S.R. and Parton, Y., J. Appl. Mech. 42, 385, 1975.

Carroll,M.M., Holt,A.C., "Static and dynamic pore-collapse relations for ductile porous materials", J. Appl. Phys., vol.43, pp.1626-1636, 1972.

Chen, D., Al-Hassani, S.T.S., Sarumi, M., Jin., X. "Crack Straining-Based Spall Model", Int. J. Impact Engng, Vol. 19, No. 2, pp. 107-116, 1997.

Cortes, R. "The growth of microvoids under intense dynamic loading", Int. J. Solids Structure Vol. 29, No. 11, pp.1339-1350, 1992.

Cortes, R. "Dynamic Growth of Microvoids Under Combined Hydrostatic and Deviatoric Stresses", Int. J. Solids Structure Vol. 29, No. 13, pp. 1637-1645, 1991.

Cortes, R., Elices, M. "Numerical Modelling of Ductile Spall Fracture", Int. J. Impact Engng Vol. 16, No. 2, pp. 237-251, 1995.

Curson,A.L., "Continuum Theory of Ductile Rupture by Void Nucleation and Growth - Part I - Yield criteria and flow rules for porous ductile media", J. Engng Mater. Tech., Vol. 99, pp. 2-15, 1977.

Dikshit, S. N., Kutumbarao, V. V., Sundararajan, G., "The Influence of Plate Hardness on the Ballistic Penetration of Thick Steel Plates", International Journal of Impact Engineering, Vol. 16, No. 2, pp. 293-320, 1995.

Dikshit, S.N., Sundararajan,G., "The Penetration of Thick Steel Plates by Olive-Shaped Projectiles-Experiment and Analysis." Int. J. Impact Engng 12, 373-408, 1992.

Grady, D.E., Journal de Physique 49, 175, 1988.

Gurson, A.L., "Continuum theory of ductile rupture by void nucleation and growth: Part I - yield criteria and flow rules for porous ductile mdeia". J. Engng Mater. Tech. 99, 2-15, 1977.

Hohler, V., Nahme, H., Tham, R., Stilp, A., Weber, K., Yeh, Y. -K., Wang, J. -P., Lee, T. -S., "Experimental and Numerical Simulation of High Velocity Impact on Steel Targets" International Journal of Impact Engineering, Vol. 14, pp. 325-334, 1993.

Hörz, F., Cintala, M. J., Bernhard, R. P., See, T.H., "Dimensionally Scaled Penetration Experiments to Extract Projectile Sizes from Space Exposed Surfaces" International Journal of Impact Engineering, Vol. 14, pp. 347-358, 1993.

Ipson, T. W., Recht, R.F., "Ballistic Perforation by Fragments of Arbitrary Shape." NWC TP 5927, Denver Research Institute, Denver, CO., 1977.

Johnson, J.N. "Dynamic Fracture and Spallation in Ductile Solids", J. Appl. Phys. American Institute of Physics, April 1981.

Kipp, M. E., Grady, D. E., Swegle, J. W., "Numerical and Experimental Studies of High-Velocity Impact Fragmentation", International Journal of Impact Engineering, Vol. 14, No. 1-4, pp. 427-438, 1993.

Kneubuehl, B.P., "Improved Test Procedures for Body Armour", Proceedings of PASS'96, DCTA 3-6, Colchester, UK, September, 1996.

McGlaun, J.M., Thompson, S.L., Elrick, M.G., "CTH: A Three-Dimensional shock Wave Physics Code." Int. J. Impact Engng., 10, 351-360, 1990.

Mott, N.F., "Fragmentation of Shell Cases", Proc. Rot. Soc., A 189, pp.300-308, 1947.

Murakami, S., Umeda, T., Takizawa, H., Itoh, M., "Application of Damage Mechanics to the Analysis of Spall Damage" International Journal Series A – Mechanics and Material Engineering, Jul., Vol. 39, No. 3, pp. 375-381, 1996.

Perzyna, P., Arch. Mech. (Marszawa) 38, 725, 1986.

Piekutowski, A. J., "Characteristics of Debris Clouds Produced by Hypervelocity Impact of Aluminum Spheres with Thin Aluminum Plates" International Journal of Impact Engineering, Vol. 14, pp. 573-586, 1993.

Piekutowski, A.J.. "Properties of Largest Fragment Produced by Hypervelocity Impact of Aluminum Spheres with Thin Aluminum Sheets." Proc. AIAA Space Programs and Technologies Conference. Huntsville, AL, Paper No. 92-1588, 1992.

Rajendran, A. M., Dietenberger, M. A. and Grove, D.J., "A Void Growth-Based Failure Model to Describe Spallation", J. Appl. Phys. 65(4), pp. 1521-1527, Feb. 1989.

Recht, R. F. and Ipson, T. W., "Ballistic Perforation Dynamics", Journal of Applied Mechanics, Vol. 30, Series E, No. 3 (Sept.), pp. 384-389, 1963.

Recht, R.F., Ipson,T.W., Wittrock, E.P., "Transformation of Terminal Ballistic Threat Definitions into Vital Component Malfunction Predictions." NWC TP 4871, Denver Research Institute, Denver, CO, 1969.

Reschauer, W., Igenbergs, E., "Experiments on the Hypervelocity Penetration of Thin Aluminum Sheets" International Journal of Impact Engineering, Vol. 14, pp. 587-596, 1993.

Rolens, D.K, Recht,R.F., Grubin,E.S., "Effects of 'G' Loading on Aircraft Vulnerability -- A user's Guide to Structural Residual Determinations." BRL Contractor Report No. 293, Denver Research Institute, Denver, CO, 1976.

Seaman, L., Curran, D. R., Shockey, D. A., "Computational models for Ductile and Brittle Fracture", Journal of Applied Physics, Vol. 47, No. 11, Nov. 1976.

Seaman, L., Curran, D.R., Murri, W.J., J. Appl. Mech. 52, 593, 1985.

Sih, G. C., "Initial Damage States of Hypervelocity Impact for Tungsten Projectile on Aluminum Target", Theoretical and Applied Fracture Mechanics, Vol. 13, July, pp. 167-180, 1990.

Steinberg, D.J., Cochran, S.G., Guinan,M.W., "A Constitutive Model for Metals Applicable at High-Strain Rate." J. Appl. Phys. 51, 1498-1504, 1980.

Taylor, R. W. and Venable, D., "An Aluminum Splash Generated by Impact of a Detonation Wave", Journal of Applied Physics, Vol. 39, No. 10 (Sept.), pp. 4633-4635, 1968.

Verolme,Dr. J.L., Szymczak,M., Bras,J.P.F., "Metallic Witness Packs foe Behind-Armour Debris Characterisation", submitted to the International Journal of Impact Engineering, 1999.

Wang, Z.-P., Lam, K.Y., "Evaluation of Microcracks in Brittle Solids Under Intense Dynamic Loading", J. Appl. Phys. 77(7), pp. 3479-3483, 1995.

Wang, Z.-P. "Spall Study in Mild Steel", Transaction of the ASME, Vol. 119, October, 1997.

Yatteau, J. D., Dickinson, D. L., "An Engineering Model to Predict Perforation Damage to Plates Impacted by High Velocity Debris Clouds" International Journal of Impact Engineering, Vol. 14, pp. 831 – 842, 1993.

Yatteau, J. D, Zernow, R. H., "MPPM3 - Multiple Plate Penetration Model, Version 3 User's Guide and Program Listing" Applied Research Associates, Inc., Lakewood, Colorado, March 22, 1990.

Yatteau, J.D., "High Velocity Multiple Plate Penetration Model," NSWC TR 82-123, Denver Research Institute, Denver, CO, 1982.

Yatteau, J.D., Dunn,J.A., Dickinson,D.L., "Terminal Ballistic Impact Fracture of Steel Cubes." NAVSWC TR 91-397, Applied Research Associates, Inc., Lakewood, CO., 1991a.

Yatteau,J.D., Zernow,R.H., Recht, R.F., "Compact Fragment Multiple Plate Penetration Model(FATEPEN2)." Vol. I – Model Description, Vol. II – Computer Code User's Manual, NAVSWC TR 21-399, Applied Research Associates, Inc., Lakewood, CO, 1991b.

Yuan, W. and Goldsmith, W., "Response of Simulated Propellant and Explosives to Projectile Impact – III Experimental and Numerical Results of Warhead Penetration and Fragmentation", International Journal of Impact Engineering, Vol. 12, No. 4, pp. 533-558, 1992.

Zheng, J., Wang, Z.-P. "Spall Damage in Aluminum Alloy" Int. J. Solid Structures Vol. 32, No. 8/9, pp. 1135-1148, 1995.

"Test Procedures for Measuring Behind-Armour Effects of Anti-Armour Ammunition", NATO Military Agency for Standardisation (MAS), STANAG 4190, Edition 2, AC/22S_D/1375, 28 February, 1996.

APPENDICES

Appendix A - Comparison of DeCaM Characterisation Results

Appendix B - Sample *.RPT File Formats

Appendix A - Comparison of DeCaM Characterisation Results

Table A.1: Test 3527 Comparison

WP Plate Hole No.*	WP Hole Area [cm²]	DeCaM 1.1 - Penetration Energy			DeCaM 2.0 - Penetration Energy			DeCaM 2.0T - Velocity Threshold Curves		
		Mass [g]	Vel [m/s]	Next Hole†	Mass [g]	Vel. [m/s]	Next Hole†	Mass [g]	Vel. [m/s]	Next Hole†
Plate No. 1										
1	0.930	3.32	185.5	1	6.75	124.7	1	11.56	56.5	1
2	1.192	4.86	157.6	2	9.87	107.5	2	16.89	50.4	2
3	0.003	0.00	0.0	-1	0.00	0.0	-1	0.00	0.0	-1
4	0.001	0.00	0.0	-1	0.00	0.0	-1	0.00	0.0	-1
5	1.934	10.19	120.3	3	20.66	83.7	3	35.33	41.1	3
6	0.100	0.09	636.2	-1	0.20	415.6	-1	0.34	148.3	-1
7	0.207	0.31	451.5	-1	0.65	312.9	-1	1.12	107.1	-1
Plate No. 2										
1	1.156	4.64	380.9	1	9.42	249.2	-1	16.12	87.7	1
2	2.219	12.56	258.3	2	25.46	173.4	2	43.54	64.2	2
3	1.736	8.64	290.2	3	17.53	197.0	3	29.97	71.2	3
Plate No. 3										
1	0.382	0.49	1230.5	1	1.14	715.7	-1	2.06	294.9	-1
2	1.056	3.25	570.2	2	6.82	368.6	-1	11.87	172.7	2
3	1.113	3.55	543.0	3	7.44	357.3	3	12.94	168.2	3
Plate No. 4										
1	0.053	0.04	4513.3	-1	0.09	2052.5	-1	0.16	995.3	-1
2	0.227	0.41	1343.0	-1	0.86	813.7	-1	1.47	485.7	-1
3	1.292	5.80	473.5	1	11.78	317.2	1	20.16	269.6	1
Plate No. 5										
1	1.679	8.60	426.8	1	17.46	287.4	1	29.85	213.4	1
Plate No.6										
1	1.385	6.44	492.4	1	13.08	329.3	1	22.37	348.3	1
Plate No. 7										
1	1.777	9.37	437.0	-1	19.01	294.1	-1	32.50	367.1	-1

The number in the column Hole No. represent the hole number on the specified witness pack plate

†Hole number indicates the number of the hole on the following witness pack plate to which the current hole is matched. A value of -1 signifies the matching process did not match the hole with any holes on the following plate.

Table A.2: Test 3528 Comparison

WP Plate Hole No.*	WP Hole Area $[cm^2]$	DeCaM 1.1 - Penetration Energy			DeCaM 2.0 - Penetration Energy			DeCaM 2.0T - Velocity Threshold Curves		
		Mass [g]	Vel. [m/s]	Next Hole†	Mass [g]	Vel. [m/s]	Next Hole†	Mass [g]	Vel. [m/s]	Next Hole†
Plate No. 1										
1	0.634	1.84	226.0	-1	6.41	118.7	-1	6.41	65.9	-1
2	0.081	0.07	737.3	-1	0.24	348.5	-1	0.24	163.4	-1
3	1.268	5.35	150.5	1	18.57	78.8	1	18.57	49.1	1
4	0.012	0.01	2146.1	-1	0.01	1429.5	-1	0.01	478.6	-1
Plate No. 2										
1	1.354	5.91	333.5	1	20.52	168.4	1	20.52	79.2	1
Plate No. 3										
1	1.159	3.81	530.4	1	13.84	259.0	1	13.84	164.7	1
Plate No. 4										
1	1.082	4.44	523.4	1	15.45	260.3	1	15.45	228.9	1
Plate No. 5										
1	1.167	4.98	522.6	1	17.30	260.3	1	17.30	261.1	1
Plate No. 6										
1	1.365	6.30	497.4	1	21.88	249.0	1	21.89	350.7	1
Plate No. 7										
1	1.654	8.41	455.5	-1	29.19	229.6	-1	29.19	378.6	-1

The number in the column Hole No. represent the hole number on the specified witness pack plate

†Hole number indicates the number of the hole on the following witness pack plate to which the current hole is matched. A value of -1 signifies the matching process did not match the hole with any holes on the following plate.

Table A.3: Test 3529 Comparison

WP Plate Hole No.*	WP Hole Area [cm²]	DeCaM 1.1 - Penetration Energy			DeCaM 2.0 - Penetration Energy			DeCaM 2.0T - Velocity Threshold Curves		
		Mass [g]	Vel. [m/s]	Next Hole†	Mass [g]	Vel. [m/s]	Next Hole†	Mass [g]	Vel. [m/s]	Next Hole†
Plate No. 1										
1	0.018				0.01	2672.3	-1	0.01	457.3	-1
2	2.944				11.96	126.4	1	11.96	55.5	1
3	2.574				9.75	133.7	2	9.75	58.7	2
4	0.610				1.07	291.9	3	1.07	108.4	3
5	0.030				0.01	2952.1	-1	0.01	501.2	-1
Plate No. 2										
1	7.036				44.75	181.2	1	44.75	63.7	1
2	4.599				23.52	224.9	2	23.52	76.2	2
3	0.690				1.29	674.0	-1	1.29	171.3	-1
Plate No. 3										
1	4.262				19.24	331.4	1	19.24	149.0	1
2	2.672				9.14	429.7	2	9.14	187.0	2
Plate No. 4										
1	3.328				14.89	380.8	-1	14.89	231.7	-1
2	4.102				20.37	334.9	1	20.37	209.5	1
Plate No. 5										
1	4.158				20.79	339.5	-1	20.79	243.9	-1

The number in the column Hole No. represent the hole number on the specified witness pack plate.

†Hole number indicates the number of the hole on the following witness pack plate to which the current hole is matched. A value of -1 signifies the matching process did not match the hole with any holes on the following plate.

Table A.4: Test 3530 Comparison

WP Plate Hole No.*	WP Hole Area [cm²]	DeCaM 1.1 - Penetration Energy			DeCaM 2.0 - Penetration Energy			DeCaM 2.0T - Velocity Threshold Curves		
		Mass [g]	Vel [m/s]	Next Hole†	Mass [g]	Vel. [m/s]	Next Hole†	Mass [g]	Vel. [m/s]	Next Hole†
Plate No. 1										
1	1.904	2.70	254.4	1	6.16	157.9	1	6.16	66.7	1
2	1.421	1.72	309.4	2	3.94	188.7	2	3.94	75.5	2
3	0.003	0.00	0.0	-1	0.00	0.0	-1	0.00	0.0	-1
4	0.017	<0.01	8914.7	-1	0.01	2773.4	-1	0.01	468.3	-1
5	2.331	3.68	223.3	3	8.38	140.9	3	8.38	61.2	3
6	0.177	0.06	1193.5	-1	0.15	632.7	-1	0.15	187.3	-1
7	0.001	0.00	0.0	-1	0.00	0.0	-1	0	0	-1
8	0.002	0.00	0.0	-1	0.00	0.0	-1	0	0	-1
Plate No. 2										
1	1.352	1.60	839.3	1	3.65	450.4	-1	3.65	128.3	-1
2	3.234	6.06	484.9	-1	13.79	280.3	-1	13.79	88.5	-1
3	3.801	7.74	419.5	2	17.62	249.6	2	17.62	82.6	2
Plate No. 3										
1	0.016	<0.01	-	-1	0.01	34868	-1	0.01	1864.0	-1
2	1.709	1.83	1077.0	1	4.41	566.0	1	4.41	233.8	1
Plate No. 4										
1	2.024	3.09	893.9	1	7.05	495.8	1	7.05	294.3	1
Plate No. 5										
1	3.655	7.52	624.0	-1	17.13	364.1	-1	17.14	262.0	-1

The number in the column Hole No. represent the hole number on the specified witness pack plate.

†Hole number indicates the number of the hole on the following witness pack plate to which the current hole is matched. A value of -1 signifies the matching process did not match the hole with any holes on the following plate.

Table A.5: Test 3531 Comparison

WP Plate Hole No.*	WP Hole Area [cm^2]	DeCaM 1.1 - Penetration Energy			DeCaM 2.0 - Penetration Energy			DeCaM 2.0T - Velocity Threshold Curves		
		Mass [g]	Vel. [m/s]	Next Hole†	Mass [g]	Vel. [m/s]	Next Hole†	Mass [g]	Vel. [m/s]	Next Hole†
Plate No. 1										
1	0.130	0.09	819.0	-1	0.18	532.8	-1	0.15	187.9	-1
2	0.209	0.20	545.2	-1	0.39	360.4	-1	0.32	151.5	-1
3	0.188	0.16	582.6	-1	0.33	382.9	-1	0.27	158.9	-1
4	0.335	0.42	410.1	1	0.83	276.0	1	0.68	122.9	1
5	0.003	0.00	0.0	-1	0.00	0.0	-1	0.00	0.0	-1
6	1.251	3.24	196.1	2	6.40	135.9	2	5.24	69.8	2
7	1.919	6.23	156.3	3	12.31	108.9	3	10.07	58.2	3
8	0.012	<0.01	3412.3	-1	0.01	1767.3	-1	<0.01	0.0	-1
9	1.283	3.37	194.7	4	6.66	134.7	4	5.44	69.0	4
10	0.503	0.79	327.5	5	1.57	222.3	-1	1.28	103.0	5
11	1.564	4.56	179.1	6	9.01	124.0	6	7.37	63.5	6
Plate No. 2										
1	0.712	1.36	659.1	-1	2.69	424.0	-1	2.2	147.7	-1
2	4.465	22.49	228.7	1	44.36	156.8	1	36.3	67.5	1
3	0.831	1.73	598.8	-1	3.42	388.4	-1	2.8	138.2	-1
4	1.016	2.35	532.5	-1	4.66	348.2	-1	3.8	126.8	-1
5	0.219	0.21	1507.3	-1	0.42	862.1	-1	0.3	247.9	-1
6	2.089	7.09	358.1	-1	14.01	240.4	-1	11.5	93.2	-1
Plate No. 3										
1	1.673	4.25	559.0	-1	8.63	366.8	-1	7.01	202.8	-1

The number in the column Hole No. represent the hole number on the specified witness pack plate.

†Hole number indicates the number of the hole on the following witness pack plate to which the current hole is matched. A value of -1 signifies the matching process did not match the hole with any holes on the following plate.

Table A.6: Test 3532 Comparison

WP Plate Hole No.[*]	WP Hole Area [cm^2]	DeCaM 1.1 - Penetration Energy			DeCaM 2.0 - Penetration Energy			DeCaM 2.0T - Velocity Threshold Curves		
		Mass [g]	Vel [m/s]	Next Hole[†]	Mass [g]	Vel. [m/s]	Next Hole[†]	Mass [g]	Vel. [m/s]	Next Hole[†]
Plate No. 1										
1	0.003	0.00	0.0	-1	0.00	0.0	-1	0.00	0.0	-1
2	0.642	2.90	171.7	-1	13.87	76.8	-1	13.87	53.3	-1
3	0.186	0.41	343.7	-1	2.01	149.1	-1	2.01	90.9	-1
4	1.407	9.67	113.5	2	46.09	51.2	2	46.09	38.2	2
5	0.008	<0.01	1912.4	1	<0.01	1218.1	-1	<0.01	494.6	-1
6	0.132	0.24	410.5	-1	1.17	176.0	-1	1.17	105.8	-1
7	0.07	0.08	603.6	-1	0.41	250.1	-1	0.41	141.0	-1
8	0.001	0.00	0.0	-1	0.00	0.0	-1	0.00	0.0	-1
9	0.061	0.06	671.3	-1	0.33	275.7	-1	0.33	150.4	-1
Plate No. 2										
1	0.002	0.00	0.0	-1	0.00	0.00	-1	0.00	0.0	-1
2	1.840	14.56	221.4	1	69.33	97.9	1	69.33	56.4	1
Plate No. 3										
1	0.848	3.55	481.2	-1	17.88	202.9	-1	17.88	152.3	-1

[*] The number in the column Hole No.[*] represent the hole number on the specified witness pack plate.

[†] Hole number indicates the number of the hole on the following witness pack plate to which the current hole is matched. A value of -1 signifies the matching process did not match the hole with any holes on the following plate.

Table A.7: Test 3533 Comparison

WP Plate Hole No.*	WP Hole Area [cm^2]	DeCaM 1.1 - Penetration Energy			DeCaM 2.0 - Penetration Energy			DeCaM 2.0T - Velocity Threshold Curves		
		Mass [g]	Vel. [m/s]	Next Hole[†]	Mass [g]	Vel. [m/s]	Next Hole[†]	Mass [g]	Vel. [m/s]	Next Hole[†]
Plate No. 1										
1	1.283	5.44	159.4	1	3.89	190.8	1	15.46	51.7	1
2	0.492	1.24	258.4	-1	0.88	314.1	-1	3.54	77.8	-1
3	0.024	0.01	2090.7	-1	<0.01	3560.8	-1	0.02	321.3	-1
4	0.910	3.21	179.0	2	2.29	215.0	-1	9.14	59.8	2
5	1.280	5.42	149.8	3	3.87	179.3	-1	15.41	51.7	3
6	1.413	6.31	143.0	4	4.51	170.7	4	17.92	49.6	4
Plate No. 2										
1	0.976	3.58	427.2	-1	2.55	526.5	-1	10.18	96.3	-1
2	0.326	0.65	766.0	-1	0.46	983.4	-1	1.87	154.7	-1
3	0.822	2.75	441.6	1	1.96	547.0	-1	7.82	103.7	1
4	2.419	14.32	244.5	2	10.24	295.6	-1	40.61	65.5	2
Plate No. 3										
1	0.938	2.67	605.7	1	1.86	761.9	-1	7.94	195.3	1
2	1.245	4.30	509.4	-1	3.02	632.0	-1	12.66	169.3	-1
Plate No. 4										
1	0.798	2.81	607.2	-1	2.00	756.9	-1	8.00	282.6	-1

The number in the column Hole No. represent the hole number on the specified witness pack plate.

[†] Hole number indicates the number of the hole on the following witness pack plate to which the current hole is matched. A value of -1 signifies the matching process did not match the hole with any holes on the following plate.

Table A.8: Test 3534 Comparison

WP Plate Hole No.*	WP Hole Area [cm²]	DeCaM 1.1 - Penetration Energy			DeCaM 2.0 - Penetration Energy			DeCaM 2.0T - Velocity Threshold Curves		
		Mass [g]	Vel. [m/s]	Next Hole†	Mass [g]	Vel. [m/s]	Next Hole†	Mass [g]	Vel. [m/s]	Next Hole†
Plate No. 1										
1	0.005	0.00	0.0	-1	0.00	0.0	-1	0.00	0.0	-1
2	0.442	0.50	411.2	2	0.88	295.0	-1	1.16	106.0	2
3	1.305	2.69	223.2	1	4.68	164.0	1	6.16	66.7	1
4	0.001	0.00	0.0	-1	0.00	0.0	-1	0.00	0.0	-1
5	0.461	0.53	407.0	3	0.94	291.4	-1	1.24	104.1	3
6	0.001	0.00	0.0	-1	0.00	0.0	-1	0.00	0.0	-1
7	0.166	0.10	753.5	4	0.18	517.1	-1	0.24	163.4	4
8	0.037	0.01	3126.3	-1	0.01	1549.7	-1	0.02	342.8	-1
9	1.270	2.58	224.2	5	4.49	164.9	5	5.91	67.5	5
10	0.819	1.31	288.1	6	2.29	209.9	6	3.01	81.3	6
11	0.734	1.11	303.9	7	1.93	221.6	-1	2.54	85.2	-1
12	2.079	5.47	179.5	8	9.53	134.1	8	12.53	54.8	8
13	1.243	2.49	240.5	-1	4.34	178.4	-1	5.72	68.1	-1
Plate No. 2										
1	1.960	5.00	428.4	-1	8.71	303.8	-1	11.46	93.2	-1
2	0.343	0.33	1355.7	-1	0.59	849.3	-1	0.78	197.5	-1
3	0.201	0.14	2151.8	-1	0.25	1235.1	-1	0.33	250.6	-1
4	0.128	0.07	3316.3	-1	0.12	1710.3	-1	0.16	308.0	-1
5	2.261	6.22	389.5	1	10.82	278.1	1	14.24	87.7	1
6	1.163	2.25	584.6	2	3.92	405.3	-1	5.16	116.4	-1
7	0.198	0.14	2133.0	-1	0.24	1227.8	-1	0.32	252.3	-1
8	1.836	4.53	460.8	-1	7.88	329.2	-1	10.37	95.8	-1
Plate No. 3										
1	2.218	5.21	567.8	1	9.24	398.2	-1	12.24	171.1	-1
2	0.008	<0.01	--	-1	<0.01	47686	-1	<0.01	2149.0	-1
Plate No. 4										
1	0.347	0.37	1832.0	-1	0.66	1127.6	-1	0.88	573.51	-1

The number in the column Hole No. represent the hole number on the specified witness pack plate

†Hole number indicates the number of the hole on the following witness pack plate to which the current hole is matched. A value of -1 signifies the matching process did not match the hole with any holes on the following plate.

Table A.9: Test 3535 Comparison

WP Plate Hole No.*	WP Hole Area $[cm^2]$	DeCaM 1.1 - Penetration Energy			DeCaM 2.0 - Penetration Energy			DeCaM 2.0T - Velocity Threshold Curves		
		Mass [g]	Vel. [m/s]	Next Hole†	Mass [g]	Vel. [m/s]	Next Hole†	Mass [g]	Vel. [m/s]	Next Hole†
Plate No. 1										
1	0.965	2.51	241.5	1	3.52	198.2	-1	3.52	77.9	-1
2	0.001	0.00	0..0	-1	0.00	0.0	-1	0.00	0.0	-1
3	2.134	8.46	137.1	2	11.83	114.5	2	11.83	55.7	2
4	0.510	0.93	295.9	3	1.31	244.7	-1	1.31	102.4	3
5	0.069	0.03	1048.0	-1	0.05	813.2	-1	0.05	253.9	-1
6	0.518	0.96	293.3	-1	1.34	243.1	-1	1.34	101.7	-1
7	1.322	4.07	176.9	4	5.70	148.2	4	5.70	68.2	4
8	0.004	0.00	0.0	-1	0.00	0.0	-1	0.00	0.0	-1
9	0.438	0.74	323.9	5	1.03	268.2	-1	1.03	109.4	5
Plate No. 2										
1	0.004	0.00	0.0	-1	0.00	0.0	-1	0.00	0.0	-1
2	2.876	13.32	268.6	1	18.63	221.3	1	18.63	81.4	1
3	0.253	0.31	1176.1	-1	0.43	901.8	-1	0.43	232.4	-1
4	3.265	16.15	250.5	2	22.58	208.0	2	22.58	77.1	2
5	0.318	0.44	1004.5	-1	0.63	783.2	-1	0.63	209.9	-1
Plate No. 3										
1	1.736	5.26	511.7	1	7.45	414.4	1	7.45	199.1	1
2	2.979	12.60	370.4	2	17.78	305.2	-1	17.78	152.6	-1
Plate No. 4										
1	2.261	9.61	418.1	-1	13.45	342.3	-1	13.45	239.3	-1
2	0.008	<0.01	93923	-1	<0.01	30929	-1	<0.01	3600.4	-1

The number in the column Hole No. represent the hole number on the specified witness pack plate.

†Hole number indicates the number of the hole on the following witness pack plate to which the current hole is matched. A value of -1 signifies the matching process did not match the hole with any holes on the following plate.

Table A.10 Test 3536 Comparison

WP Plate Hole No *	WP Hole Area [cm^2]	DeCaM 1.1 - Penetration Energy			DeCaM 2.0 - Penetration Energy			DeCaM 2.0T - Velocity Threshold Curves		
		Mass [g]	Vel. [m/s]	Next Hole[†]	Mass [g]	Vel. [m/s]	Next Hole[†]	Mass [g]	Vel [m/s]	Next Hole[†]
Plate No. 1										
1	0.439	1.04	266.7	1	3.27	144.4	1	3.27	79.5	1
2	0.204	0.31	416.9	2	0.98	219.5	-1	0.98	111.0	2
3	2.034	11.00	118.8	3	34.38	65.7	3	34.38	41.4	3
4	1.213	4.99	155.2	4	15.64	85.4	4	15.64	51.5	4
5	0.294	0.55	333.9	-1	1.75	178.9	-1	1.75	94.5	-1
6	1.531	7.13	141.5	5	22.31	79.4	5	22.31	46.7	5
7	0.888	3.09	191.5	6	9.70	106.9	6	9.70	58.8	6
Plate No. 2										
1	0.267	0.47	874.2	-1	1.50	425.6	-1	1.50	164.3	-1
2	0.083	0.07	2086.4	-1	0.23	852.1	-1	0.23	278.5	-1
3	2.744	17.34	229.4	2	54.18	124.2	2	54.18	60.4	2
4	1.104	4.32	376.4	1	13.54	198.7	1	13.54	88.9	1
5	0.392	0.87	709.8	-1	2.74	361.7	-1	2.74	138.9	-1
6	0.918	3.26	437.2	-1	10.21	233.6	-1	10.21	96.2	-1
Plate No. 3										
1	0.899	2.48	627.2	1	8.16	318.3	1	8.16	193.6	1
2	1.114	3.56	549.3	-1	11.65	282.1	-1	11.65	173.7	-1
Plate No. 4										
1	0.825	2.95	613.8	1	9.27	317.8	1	9.27	269.6	1
Plate No. 5										
1	0.810	2.87	646.1	1	9.02	333.7	1	9.02	332.7	1
Plate No. 6										
1	0.945	3.62	614.3	1	11.36	319.3	1	11.36	429.9	1
Plate No. 7										
1	0.674	2.18	758.6	-1	6.84	387.3	-1	6.84	575.3	-1

*The number in the column Hole No * represent the hole number on the specified witness pack plate.

[†] Hole number indicates the number of the hole on the following witness pack plate to which the current hole is matched. A value of -1 signifies the matching process did not match the hole with any holes on the following plate.

Appendix B - Sample *.RPT File Formats

B.1 New Format (4 Column Format)

B.2 Old Format (5 Column Format)

B.1 New Format (4 Column Format)

```
Date      :   11-OCT-89                          Page  1
Time      :   15:52:52
Plate ID  :   RD-67-1
Units     :   CM
# Holes   :   53

Hole           Hole          Hole X         Hole Y
Number         Area          Centroid       Centroid

1              .0074090     -13.4677500     31.0938000
2              .2025128      -5.4274030     50.2029500
3              .0049393      16.5150200     24.2468600
4             1.7460560      18.1893000     78.0243800
5              .0074090      16.8377100     24.2740800
   .              .              .              .
   .              .              .              .
   .              .              .              .
46             .2889512      44.5881300     57.0311300
47             .5680237      45.0816900     83.5706600
48            1.0150340      45.2194700     72 1498600
49             .8100513      45.3828200     79.7841100
50            7.9251660      47.5745200     81.2615900

Date      :   11-OCT-89                          Page  2
Time      :   15:52:52
Plate ID  :   RD-67-1
Units     :   CM
# Holes   :   53

Hole           Hole          Hole X         Hole Y
Number         Area          Centroid       Centroid

51           20.0611200      47.5526500     92 0565700
52             .0691507      45.8868900     64.8233500
53             .3852683      46.4013600     84.3708400
```

B.2 Old Format (5 Column Format)

```
Date     :    11-OCT-89                                    Page  1
Time     :    15:52:52
Plate ID :    RD-67-1
Units    :    CM
# Holes  :    53

Hole          Hole          Hole          Hole X         Hole Y
Number        Width         Area          Centroid       Centroid

1             -.0009912      .0074090     -13.4677500     31.0938000
2             -.0074344      .2025128      -5.4274030     50.2029500
3             -.0004956      .0049393      16.5150200     24.2468600
4             -.0113994     1.7460560      18.1893000     78.0243800
5             -.0009912      .0074090      16.8377100     24.2740800
  .               .             .               .              .
  .               .             .               .              .
  .               .             .               .              .
46            -.0054519      .2889512      44.5881300     57.0311300
47            -.0074344      .5680237      45.0816900     83.5706600
48            -.0109037     1.0150340      45.2194700     72.1498600
49            -.0099125      .8100513      45.3828200     79.7841100
50            -.0401456     7.9251660      47.5745200     81.2615900

Date     :    11-OCT-89                                    Page  2
Time     :    15:52:52
Plate ID :    RD-67-1
Units    :    CM
# Holes  :    53

Hole          Hole          Hole          Hole X         Hole Y
Number        Width         Area          Centroid       Centroid

51            -.0594750    20.0611200      47.5526500     92.0565700
52            -.0029737      .0691507      45.8868900     64.8233500
53            -.0069387      .3852683      46.4013600     84.3708400
```